THE EFFECTS OF HYDROGEN BONDING ON THE REACTIVITY OF SYNTHETIC ADA REPAIR PROTEIN ANALOGUES

by

Josiah G. Elsberg

A thesis

submitted in partial fulfillment

of the requirements for the degree of

Master of Science in Chemistry

Boise State University

May 2016

BOISE STATE UNIVERSITY GRADUATE COLLEGE

DEFENSE COMMITTEE AND FINAL READING APPROVALS

of the thesis submitted by

Josiah G. Elsberg

Thesis Title: The Effects of Hydrogen Bonding on the Reactivity of Synthetic Ada Repair Protein Analogues

Date of Final Oral Examination: 04 March 2016

The following individuals read and discussed the thesis submitted by student Josiah G. Elsberg, and they evaluated his presentation and response to questions during the final oral examination. They found that the student passed the final oral examination.

Eric C. Brown, Ph.D.	Chair, Supervisory Committee
Don L. Warner, Ph.D.	Member, Supervisory Committee
Jeunghoon Lee, Ph.D.	Member, Supervisory Committee

The final reading approval of the thesis was granted by Eric C. Brown, Ph.D., Chair of the Supervisory Committee. The thesis was approved for the Graduate College by John R. Pelton, Ph.D., Dean of the Graduate College.

DEDICATION

I would like to dedicate this thesis to my Mom and Dad, who have blessed me throughout my whole life. I love you both very much.

ACKNOWLEDGEMENTS

I would like to thank Dr. Eric Brown for everything he has done for me in my research and time as a graduate student. I have learned much more than I ever imagined I would from his guidance. I would like to thank Dr. Don Warner and Dr. Jeunghoon Lee for their involvement in my graduate career at Boise State University and being a part of my committee. I would also like to thank Dr. Joe Dumais for his assistance with the NMR spectra and kinetic data included in this thesis. Lastly, I would like to thank my fellow lab mates: Jeff Barlow, Martin Garcia, Lillian Volz, and Carson Kidwell for their moral support and involvement in the project.

ABSTRACT

The study of bioinorganic chemistry is an important field, as it can provide insight as to why nature has chosen certain active sites and structures within different kinds of metalloproteins. Ada repair protein, a zinc-containing metalloprotein, is one such topic of interest. Although it is known that Ada RP is able to repair methyl-phosphotriester backbone damage by self-methylation of one of its cysteine groups, the mechanism is not fully understood. Two pathways have been proposed: a dissociative pathway where the Zn-S bond becomes a zinc/sulfur ion pair and an associative pathway where a four ringed σ-metathesis occurs. Previous research has shown that a sulfur rich environment will increase the probability of thiolate dissociation, and that the probability of dissociation is dependent on the environment of the primary coordination sphere. However, we believe that the secondary coordination sphere (hydrogen bonding) is also able to increase dissociation probability. Two nitrogen-rich complexes, $[(TPA)ZnSPh]^+$ and $[(BA\text{-}TPA)ZnSPh]^+$, were synthesized (with $[(BA\text{-}TPA)ZnSPh]^+$ having a hydrogen bond donor). Both the ^1H and ^{13}C NMR spectra show broad peaks (a sign of dissociation) within $[(BA\text{-}TPA)ZnSPh]^+$ (the hydrogen bonding complex). These broad peaks became sharp when the sample is cooled, giving more plausibility that thiolate dissociation is occurring. Alkylation of the zinc-thiolate complexes showed the $[(BA\text{-}TPA)ZnSPh]^+$ complex having a larger rate constant ($6.49 \times 10^{-3}\ M^{-1}s^{-1}$) compared to $[(TPA)ZnSPh]^+$ ($1.51 \times 10^{-3}\ M^{-1}s^{-1}$). The larger rate constant for $[(BA\text{-}TPA)ZnSPh]^+$ is due to the sulfur of $[(BA\text{-}TPA)ZnSPh]^+$ being more nucleophilic (another sign of dissociation). These

results add credibility to the secondary coordination sphere increasing probability of dissociation, and as a result opens a new opportunity for future research in this field.

TABLE OF CONTENTS

LIST OF FIGURES

LIST OF TABLES

LIST OF ABBREVIATIONS

Ada RP	Ada Repair Protein
MGMT	O^6-alkylguanine-DNA alkyltransferase
DMSO	Dimethyl Sulfoxide (Deuterated)
NMR	Nuclear Magnetic Resonance
IR	Infrared Spectroscopy
Tp	Tris(pyrazolyl)borate
Ph	Phenyl
t-bu	Tert-butyl
MeI, CH_3I	Methyl Iodide
KOH	Potassium Hydroxide
TPA	Tris(2-pyridylmethyl)amine
BA-TPA	*N*-benzyl-6-((bis(pyridin-2- ylmethyl)amino)methyl)pyridin-2-amine
CD_3CN	Deuterated Acetonitrile
COSY	Correlation Spectroscopy
HSQC	Heteronuclear Single Quantum Correlation
HMBC	Heteronuclear Multiple Bond Correlation
NEM	N-Ethylmaleimide
HSPh	Thiophenol

CHAPTER ONE: INTRODUCTION

Metalloproteins and Bioinorganic Chemistry

Bioinorganic chemistry is the study of how Nature utilizes metals in natural biochemical reactions. The main focus of this field of study is a specific group of proteins called metalloproteins. Metalloproteins contain at least one metal cofactor, which is a metal ion that is required for the activity of a metalloprotein.[1] These metal cofactors serve several functions within the protein, ranging from catalysis (where the metal ion catalyzes a specific reaction such as carbonic anhydrase)[2], transport proteins (hemoglobin)[3] and even protein structure stability (zinc fingers).[4] Metalloproteins are an important function in all biological life. There are many questions that researchers ask when studying metalloproteins. Why has Nature chosen this particular metal to be used in a metalloprotein? How does the metal site perform its function? Why does it bind with specific amino acids? Would the metalloprotein function the same way if the metal was changed? These are examples of the types of questions that research in bioinorganic chemistry strive to answer.

Research pertaining to metalloproteins is an important area of study for a variety of reasons. For example, potential antibiotics may be discovered by studying the structure of certain metalloproteins. Investigating the metalloproteins of dangerous bacteria could lead to the development of mechanism based inhibitors.[5] There is also potential cancer treatment within studying metalloproteins, as some stimulate tumor growth, which can be inhibited to slow the process.[6] In terms of non-medical applications, research pertaining

to metalloenzymes could lead to improved environmental scrubbers (which are complexes used to reduce or prevent air pollution).[7]

The metalloprotein that the following research is interested in is Ada repair protein. This specific metalloprotein is a two-terminus zinc-containing protein that is involved in the repair of methylated DNA. The mechanism that it follows is of interest to the bioinorganic community, as it is not fully understood.

DNA Damage and Repair

Methylation caused by alkylating agents can affect multiple parts of the DNA strand. One of the main targets is the base pairs themselves. These alkylating agents can react with either guanine or thymine, forming O^6-methylguanine (guanine with a methylated oxygen) or O^4-methylthymine (thymine with a methylated oxygen). Both of these altered bases are problematic because they can form irregular base pairs.[8,9] O^6-methylguanine will form pairs with thymine instead of cytosine, while O^4-methylthymine forms pairs with guanine instead of adenine. If left untreated, these two methylated bases can cause transcriptions errors and eventual cell death in single celled organisms, and in humans can be a cause of cancer.[10]

Besides the base pairs, the phosphate backbone is also a target for alkylating agents.[11] In its natural form, the backbone of DNA contains phosphate groups that are resistant to cleavage. However, once the nucleophilic oxygen within the phosphate has been methylated, it forms a methyl-phosphotriester, which is more vulnerable to cleavage from water. This will eventually cause single strand breaks in the DNA strand, which can cause serious damage if left unattended. However, this methylation damage is not a primary danger to DNA compared methylation of guanine O^6-methylguanine.[12]

One of the sources of these alkylating agents originate from a specific group of S_N1 agents called nitrosamines. DNA strands in E. coli, for example, can be attacked by reactive nitrosamines such as *N*-nitroso-*N*-methylurea and *N*-methyl-*N'*-nitro-*N*-nitrosoguanidine.[13] These two molecules are some of the nitrosamides responsible for both the methylated base pairs and the methylated phosphate backbone. These molecules can be found in Nature as a product of the nitrosation (converting groups into nitrosogroups) of amides like methylurea and methylguanidine.[14] In terms of human consumption, these compounds can be found in alcoholic beverages and certain cured meats (such as smoked fish and pork)[15], as well as tobacco smoke.[16]

To defend against this threat, prokaryotes have developed a response called the Ada regulon response. This adaptive response is composed of four proteins that aid in the defense and repair of methylated DNA.[17] The three minor proteins of the adaptive response are AlkA, AlkB, and AidB. The AlkA protein is a glycosylase that cleaves off methylated bases (such as 3-methyladenine), which creates an abasic site (a site within DNA without a base) that is further repaired by other proteins.[18,19] AlkB is a protein that contains an Fe^{2+} center and an α ketoglutarate within its active site, and repairs several different methylated groups (such as 1-methyladenine and 3-methylcysteine).[20] There is very little known about AidB, other than it has a similar structure to isovaleryl coenzyme A dehydrogenase, which might be the only clue so far as to what function it performs.[21] There is also a possibility that AidB catalyzes the methylation repair of DNA, based on observations of it being able to bind to double stranded DNA.[22] Nonetheless, all three of these proteins are the minor proteins in the Ada response.

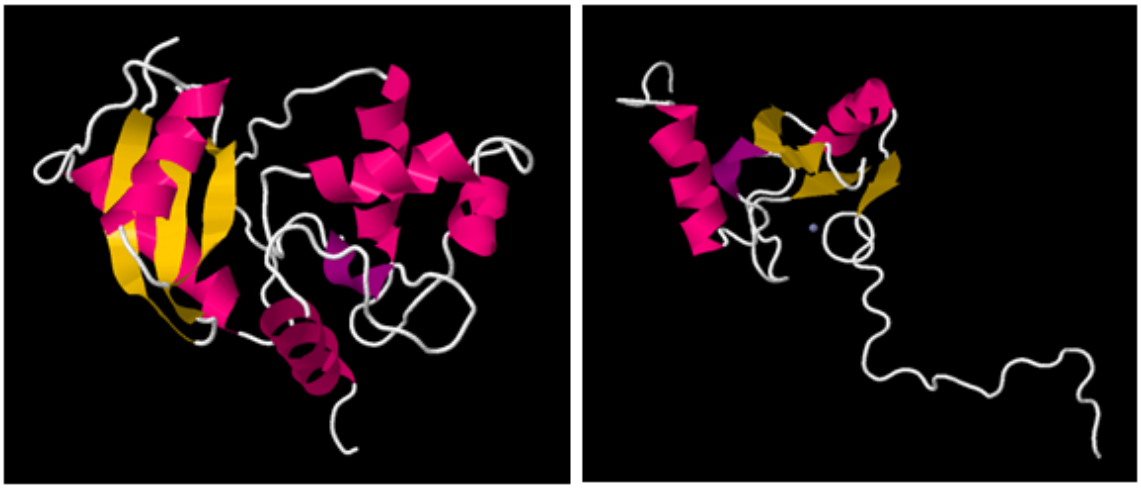

Figure 1. Protein Crystal Structure of C-Terminus (Left) and N-Terminus (Right) of Ada Repair Protein

The major protein of the Ada response is the Ada repair protein (Ada RP). The Ada repair protein (where Ada refers to the name "adaptive") is composed of two termini, an N-terminus and a C-terminus (Figure 1).[23,24] Although both of these termini are connected, they each perform different functions. The C-terminus contains an active site that repairs O^6-methylguanine, methylating its Cys-321 residue to repair the base. The N-terminus repairs the methylated phosphate backbone, containing an active site with four cysteine residues (Cys-42, Cys-69, Cys-72, and Cys-38) and a Zn^{2+} ion center as a ligand.[25] To repair the phosphate, Cys-38 undergoes methylation (via an S_N2 reaction where the thiolate acts as a nucleophile) to fix the phosphate backbone. Ada RP is the most important protein of the Ada response because it regulates the transcription of the other genes.[12] Specifically, once both termini are methylated, the Ada RP becomes an inducer for the Ada regulon by binding to DNA containing the gene for the adaptive response, while also enlisting an RNA polymerase to bind with the site to induce transcription.[17,26] This means that the more methylated DNA within a prokaryote, the

more methylated Ada RP becomes. This will lead to more activity from the Ada regulon response and a stronger defense against methylation.

The N-terminus of Ada RP is an enzyme of interest not only because of its unique active site structure, but also because of the unique way it reacts with the methylated backbone. Although the active site contains four cysteine groups, only one of them reacts. As can be seen in Figure 2, Cys-38 will react in a nucleophilic manner and attack the alkylated group.[27] Since the carbon atom of the methyl group is partially positive (due to the polarization of the carbon-oxygen bond), it will be slightly electrophilic. As the sulfur atom on Cys-38 forms a bond with the methyl group on the phosphate backbone, the electrons in the carbon-oxygen bond will shift and make oxygen an anion, restoring the phosphate. Ada RP performs this reaction rather quickly, with a second order rate constant of 2.8×10^2 M^{-1} s^{-1} at 4°C (pH: 7.8).[28] However, once Cys-38 has been methylated, the reaction cannot be reversed, which makes N-terminus Ada RP a sacrificial metalloprotein rather than a true metalloenzyme.

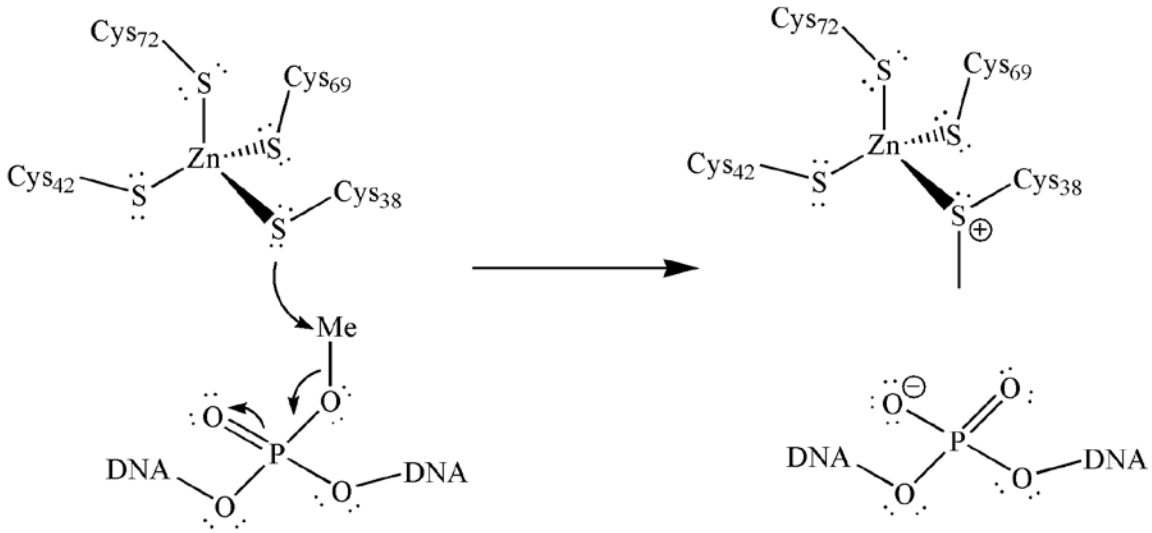

Figure 2. General mechanism of repair by N-terminus Ada RP's active site

Humans have a similar metalloenzyme called O^6-alkylguanine-DNA alkyltransferase (MGMT). MGMT contains a Zn^{2+} ion with two cysteine and two histidine ligands attached to the N-terminus of the protein.[29] However, MGMT does not utilize this complex (the N-terminus is inactive in MGMT), and is known to only repair O^6-methylguanine in human cells. As such, MGMT is not a bifunctional protein, and only the C-terminus of the protein has a functional role. The mechanism of the C-terminus involves methylating the sulfur on Cys-145, which is no longer active after reacting (similar to Ada RP).[30] MGMT also serves another function that is similar to Ada RP in terms of regulations. Once MGMT has been methylated, it will block estrogen receptors from activating cell proliferation (which is what controls cell growth and the number of cells).[31] This is likely to occur due to the human body needing to control damaged cells from growing and keeping the body healthy. There is currently no known human equivalent of N-terminus Ada RP that can fix a methylated phosphate backbone.[11]

Dissociative/Associative Mechanism

As previously mentioned, the mechanism of Ada RP is a subject of inquiry because although it is known that Cys-38 is methylated, the mechanism of this function is not fully understood. Two potential mechanisms have been proposed for the reaction. From Figure 3, the first mechanism is called the dissociative pathway. This pathway involves heterolytic cleavage of the Zn-S bond to form an ion pair, with the zinc becoming cationic and the sulfur of the thiolate becoming anionic.[32] When dissociation forms a free thiolate, it makes the sulfur more electron rich. Since it is now anionic instead of neutral (and less sterically encumbered), one would expect the free thiolate to

be a better nucleophile would undergo alkylation more readily (resulting in a larger rate constant).

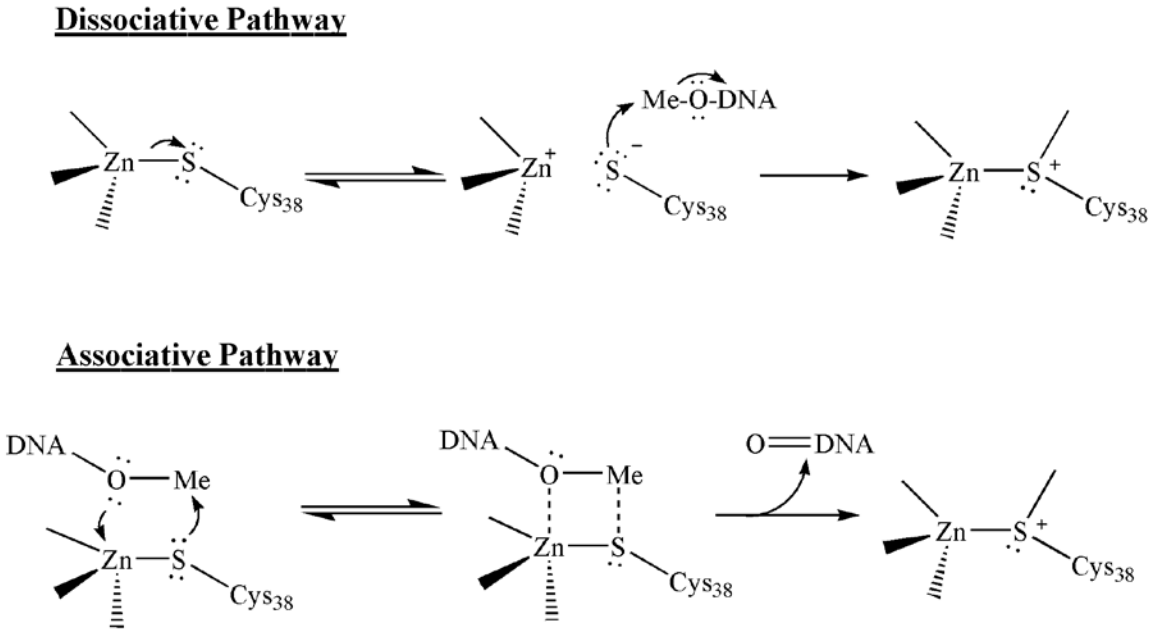

Figure 3. Possible pathways of repair of N-terminus Ada RP's active site

The other potential mechanism is called the associative pathway. Rather than undergoing alkylation with prior dissociation of thiolate, the associative pathway follows a σ-metathesis pathway involving alkylation at the zinc-bound thiolate to form a four membered ring intermediate.[33] Conversion of the four membered ring intermediate via a concerted [2 + 2] cycloaddition results in the methyl group being transferred to the sulfur and the repaired DNA departing. Arguments against this pathway suggest that the steric hindrance of the surrounding protein blocks access to Cys-38, and the fact that a zinc-bound thiolate is a weak nucleophile.[34] Although both of these paths are different in how they react, the same product will occur either way.

In order to study the active site, numerous researchers have used synthetic analogues to investigate the mechanism it utilizes. Synthetic analogues are low molecular-weight complexes that mimic the active site and reactivity of

metalloproteins.[35,36] Rather than work with a bulky metalloprotein, synthetic analogues are complexes that mimic the primary (and sometimes secondary) coordination sphere present in the active site of the metalloprotein. There are many advantages to this approach, such as synthetic analogues being easier to work with using common modern spectroscopy (such as NMR and IR). There is also room for fine tuning (electronically and sterically) with synthetic analogues. For example, the question could be asked as to why Nature has chosen four cysteine residues to be connected to a Zn^{2+} ligand. Using synthetic analogues, changes could be made to the structure (such as replacing a sulfur donor group with a nitrogen or oxygen donor) to study the effects of different donor-types on the reactivity.

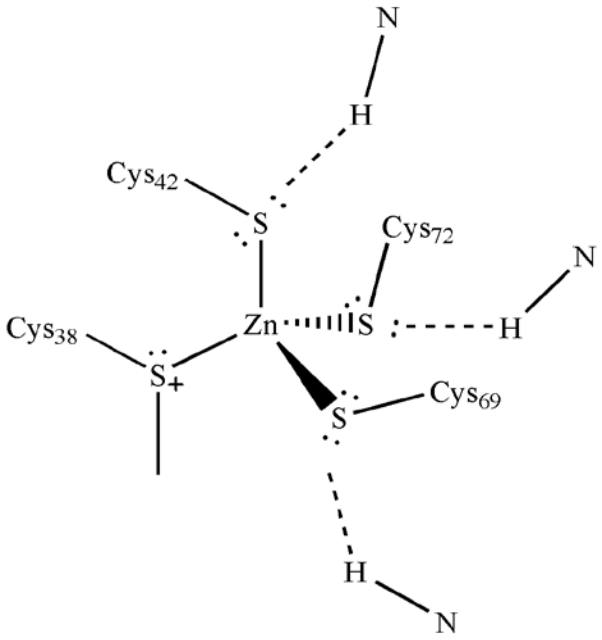

Figure 4. The effects of the primary and secondary coordination spheres in methylated Ada RP's active site

The only disadvantage to using synthetic analogues is that they are not able to mimic all aspects of the protein, which is why there are so many factors to take into account when designing these complexes. Along with requiring the analogue to work in

similar environments as the metalloprotein it mimics (i.e. pH), one of the main factors to take into account when designing synthetic analogues is the coordination spheres of the complex. There are two coordination spheres to bear in mind when designing complexes. The first is the primary coordination sphere. This coordination sphere refers to the donor groups (typically amino acids or aqua ligands) that are directly attached to the metal ion center. In the case of Ada RP, the primary coordination sphere consists of four cysteine thiolates that bind the zinc ion, as shown in Figure 4.

The secondary coordination sphere refers to amino acid residues that do not bind directly to the metal ion but do influence reactivity through non-covalent interactions (i.e. hydrogen bonding interactions). In Ada RP, alkylation occurs regiospecifically with Cys-38, even though three other cysteine residues (Cys 42, 69 and 72) are bound to the zinc center (see Figure 4). [25] Hydrogen bonding interactions between cysteines 42, 69 and 72 (see Figure 4) and amide groups from the protein chain have been used to explain why alkylation is suppressed for these residues.

Previous Synthetic Analogues

Lippard *et. al* were one of the first groups to explore Ada RP's reactivity and mechanism using synthetic analogues.[322] In their research, they wanted to understand why Nature chose four cysteine ligands to bind the zinc (II) ion within the Ada RP active site. They also wanted to know if alkylation occurs at a zinc-bound or dissociated thiolate, along with finding the differences in nucleophilicity when changing the ligand donor groups. As such, they prepared $[Zn(SC_6H_5)_4]^{2-}$, which mimicked the primary coordination sphere of Ada RP (similarities between the Ada RP active site and $[Zn(SC_6H_5)_4]^{2-}$ are evident when comparing Figures 4 and 5). In addition, they also

prepared two other complexes: $[Zn(SC_6H_5)_3(MeIm)]^-$ and $[Zn(SC_6H_5)_2(MeIm)_2$ (Figure 5), which were both made to examine if changes to the primary coordination sphere (replacing a sulfur group with a nitrogen group) influenced the alkylation mechanism.

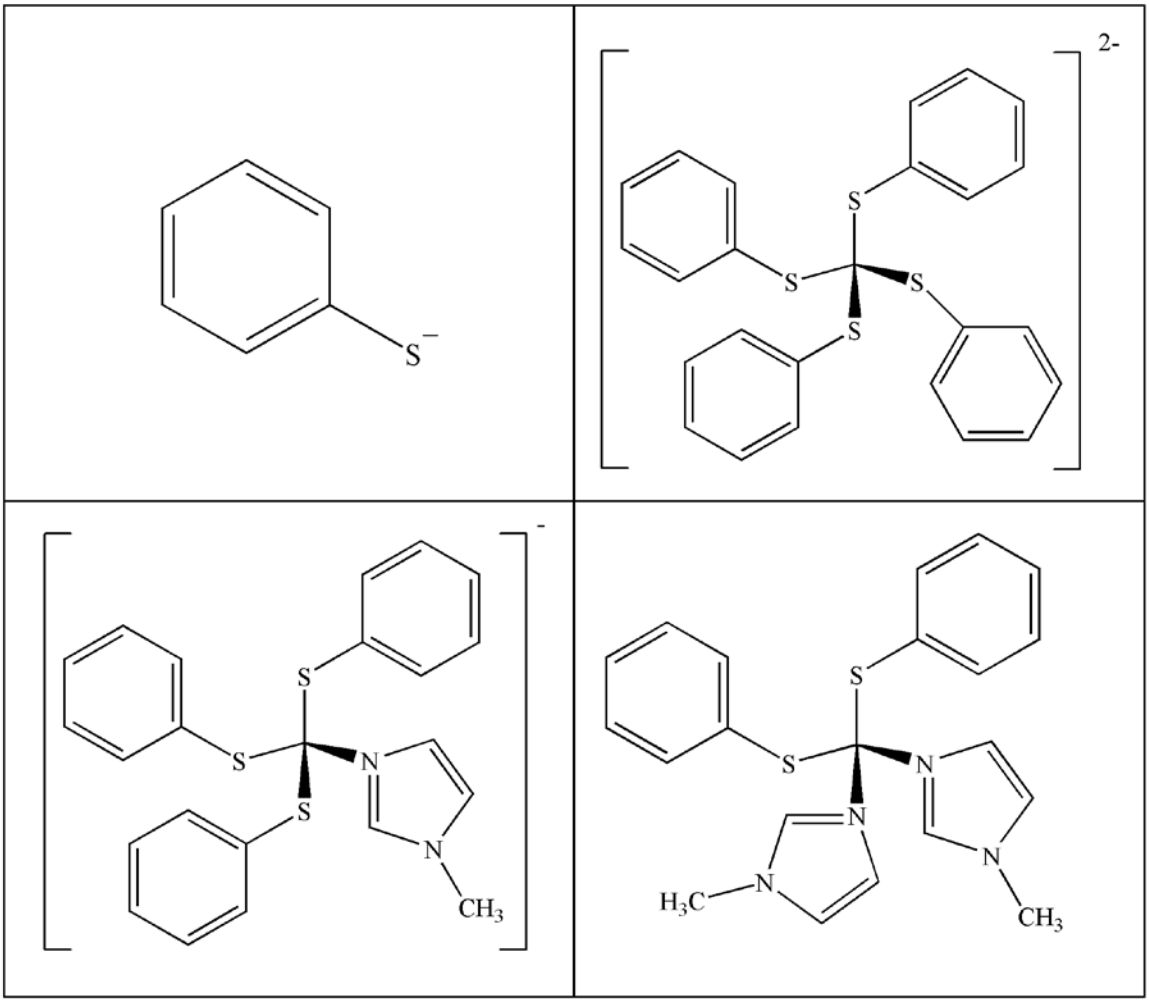

Figure 5. The complexes from Lippard Paper; Top left: $[SC_6H_5]^{2-}$, Top Right: $[Zn(SC_6H_5)_4]^{2-}$, Bottom left: $[Zn(SC_6H_5)_3(MeIm)]^-$, Bottom right: $Zn(SC_6H_5)_2(MeIm)_2$

These complexes were used in kinetic experiments to examine the effect of changing the primary coordination sphere on the rate constant of the alkylation reaction. Trimethyl phosphate was used as the alkylating reagent that reacted with the zinc thiolate complexes, since the structure of trimethyl phosphate is similar to methylated DNA. The

kinetics for each of the complexes were ran under pseudo-first order conditions (the amount of trimethyl phosphate was held constant by using a ten-fold excess, while the amount of zinc-containing complex was changed) in DMSO.

The pseudo-first-order rate constants obtained for the alkylation of benzenethiolate and the zinc complexes with trimethyl phosphate are shown in Table 1. The trend observed was that free benzenethiolate reacted the fastest, followed by $[Zn(SC_6H_5)_4]^{2-}$, $[Zn(SC_6H_5)_3(MeIm)]^{1-}$ and $[Zn(SC_6H_5)_2(MeIm)_2]$ (which was the slowest complex). The interesting result was how complexes with a sulfur-rich environment around zinc result in more reactive compounds towards alkylation. The increase in reactivity for $[Zn(SC_6H_5)_4]^{2-}$ compared to $[Zn(SC_6H_5)_3(MeIm)]^{1-}$ and $[Zn(SC_6H_5)_2(MeIm)_2]$ was attributed to an increase in the ionic nature of the zinc-thiolate bond. This shift in the bonding (from more covalent to more ionic) changes the ease of thiolate dissociation from the complexes (thiolate dissociation is more prevalent in sulfur-rich coordination environments), which then determines the rate of alkylation (a free thiolate should be the most reactive, as observed in Table 1).

Table 1. Results from Lippard's Kinetics and characterized NMR Data

Complex	*Kinetic Rate (s^{-1})*	*^1H NMR Peaks*
$SC_6H_5^-$	$1.1x10^{-4}$	Sharp
$[Zn(SC_6H_5)_4]^{2-}$	$8.2x10^{-5}$	Broad
$[Zn(SC_6H_5)_3(MeIm)]^-$	$6.0x10^{-6}$	Less Broad
$Zn(SC_6H_5)_2(MeIm)_2$	$5.0x10^{-8}$	Sharp

NMR studies provided further evidence to support that thiolate dissociation from the complexes with increased thiolate coordination (the sulfur-rich complexes) was

occurring. Lippard *et. al* noticed the aromatic peaks of $[Zn(SC_6H_5)_4]^{2-}$ were broad, and that when a benzenethiolate ligands was replaced with a methyl imidazole (nitrogen donor) to form $[Zn(SC_6H_5)_3(MeIm)]^{1-}$, the peaks began to sharpen slightly. This sharpening trend continued with an additional nitrogen donor (forming $[Zn(SC_6H_5)_2(MeIm)_2]$), which resulted in a complex with peaks that were sharp and contained resolved spin-spin coupling (comparable to free $[S(C_6H_5)]^-$). Based on both the kinetic data and the spectra from ^1H NMR, Lippard concluded that the thiolates in $[Zn(SC_6H_5)_4]^{2-}$ and $[Zn(SC_6H_5)_3(MeIm)]^{1-}$ were dissociating and thiolate dissociation was occurring more readily in $[Zn(SC_6H_5)_4]^{2-}$ versus $[Zn(SC_6H_5)_3(MeIm)]^{1-}$. The broadness of the aromatic peaks represent a rapid exchange between a zinc-bound thiolate and a dissociated thiolate on the NMR time scale. It became apparent from the ^1H NMR and kinetics results that thiolate dissociation in $[Zn(SC_6H_5)_4]^{2-}$ and $[Zn(SC_6H_5)_3(MeIm)]^{1-}$ was responsible for the increased reactivity. As mentioned previously, a dissociating sulfur is more anionic (and therefore more nucleophilic), which would explain why $[Zn(SC_6H_5)_4]^{2-}$ reacts more quickly. The take-home message was that altering the primary coordination sphere was the cause of the changes, as the other two complexes had sharper peaks and also reacted slower depending on how many imidizoles (nitrogen donors) replaced the thiolate groups (sulfur donors).

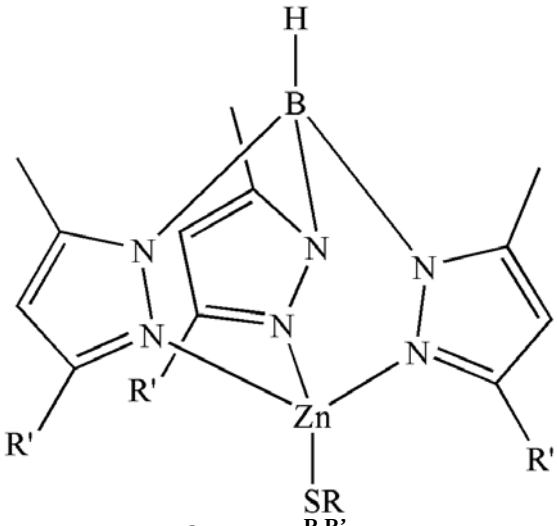

Figure 6. General Structure of the [$Tp^{R,R'}$] complex; R = Ph, Et R' = Ph, T-Bu

Several other groups witnessed a similar trend when using zinc-thiolate synthetic analogues supported with a tris(pyrazolyl)borate (Tp) ligand. These complexes have the form [Tp^{R}Zn-SR'] (Figure 6).[37] Varhenkamp *et. al* synthesized different [Tp^{R}Zn-SR'] complexes with varying degrees of steric hindrance (R' = Ph, t-Bu). They accomplished this by using phenyl rings, t-butyl, or other large nonpolar functional groups to provide steric hindrance, similar to the surrounding protein that would be in Ada RP's active site. Different thiolate groups were also attached to the zinc center, mainly phenyl and ethyl groups. For comparison to our research, the results of complexes containing the thiophenolate group will be focused upon (Figure 7).

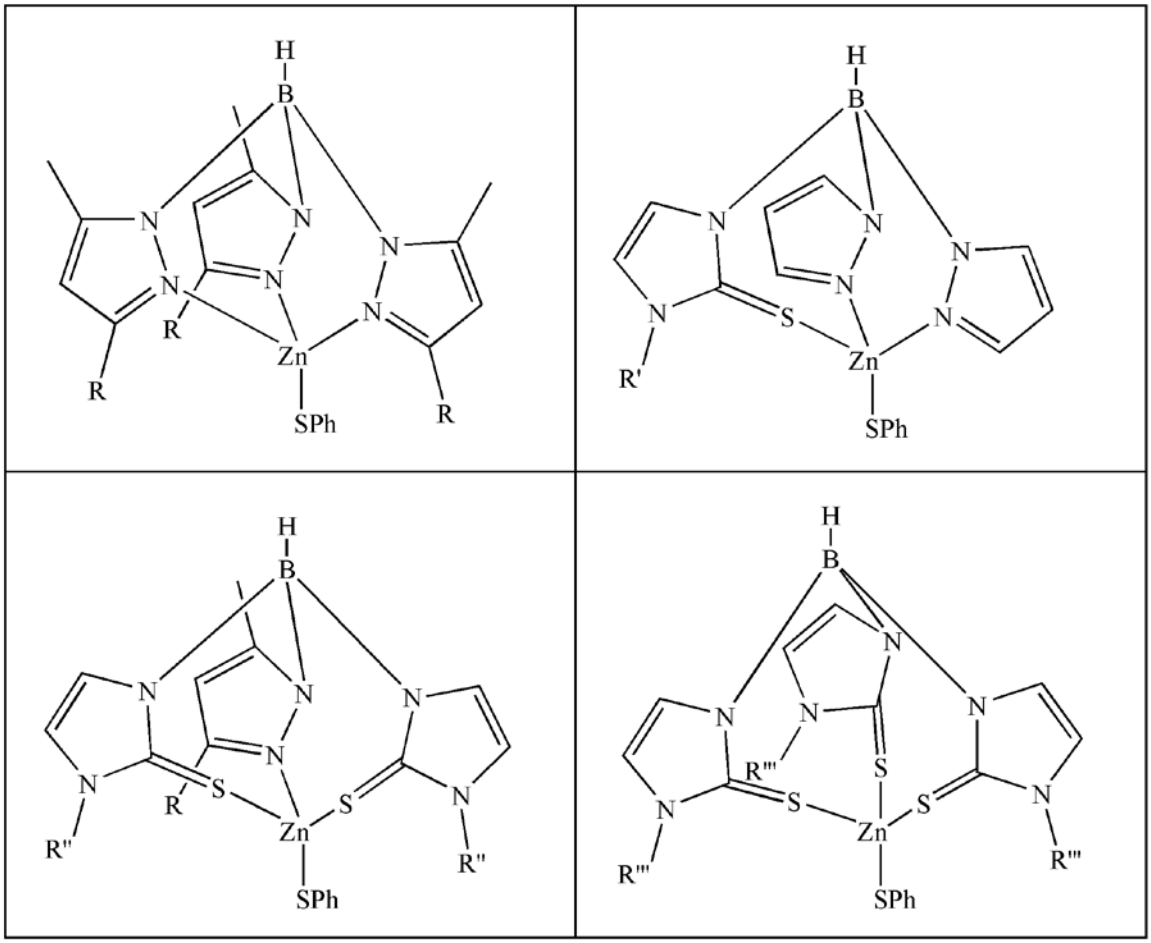

Figure 7. $[Tp^{Ph,R}]$ Complexes with different donating groups; Top left: (N_3)Zn-SPh R=Ph, Top Right: (N_2S)Zn-SPh R′=t-Bu, Bottom Left: (NS_2)Zn-SPh R=Ph, R′′=$(2\text{-}OCH_3)C_6H_4$, Bottom right: (S_3)Zn-SPh R′′′=$(2,6(CH_3)_2C_6H_3$

In addition to preparing zinc-thiolate complexes with a nitrogen-rich coordination environment, Vahrenkamp *et. al* also prepared a series of ligands with different donor-types (i.e nitrogen and sulfur donors). This was done to study the effects of changing the primary coordination sphere on reactivity. Figure 7 provides a small sample of the different complexes that were prepared. Kinetic studies were completed in a similar method to Lippard's experiments. However, instead of having a constant amount of trimethyl-phosphate and varying the amount of complex, a different approach was utilized. Methyl iodide was used as the electrophilic alkylating reagent, and instead of varying the amount of complex (concentration of zinc complexes were held constant), the

concentration of methyl iodide were varied (ranging from 5-20 equivalent excess). This was done to ensure pseudo-first order kinetics, which would eventually lead to second order rate constants.

The results of the kinetics (second-order rate constants) for the alkylation of the [$Tp^{Ph,R'}$] zinc-thiolate complexes can be seen in Table 2. From these results, a similar trend seen from Lippards group was observed. Although (N_3(Ph)(Zn-SPh)) has a slightly faster rate constant than (N_2S(Zn-SPh)), the overall trend from the kinetics matches the results Lippard *et. al* observed (i.e. complexes with sulfur-rich coordination spheres result in faster alkylation rates). This adds further credibility to the theory that sulfur-rich coordination environments favor a dissociative mechanism, and that nitrogen-rich environments proceed through an alternate and slower mechanism.

Table 2. The kinetic results (second order rate constants) for different [$Tp^{Ph,R'}$] complexes

Complex	*Kinetic Rate ($M^{-1}s^{-1}$)*
($N_{3(}$(Ph)(Zn-SPh))	$2.0x10^{-3}$
(N_3(t-bu)(Zn-SPh))	$1.0x10^{-5}$
(N_2S(Zn-SPh))	$1.4x10^{-4}$
(NS_2(Zn-SPh))	$6.2x10^{-2}$
(S_3(Zn-SPh))	$1.1x10^{-1}$

Vahrenkamp *et. al* provide a theory as to why the complexes with nitrogen-rich coordination environments are slower.[38] In previous research with a [Tp^{R}Zn-OH] complex, they noticed a four membered intermediate forming with Zn-O and CO_2 substrates when the complex cleaved the carbonyl bond. This mechanism, defined as σ-metathesis, was theorized to also be the mechanism that Zn-SR and Me-I groups were

following. The reason why this might occur within these complexes was due to the neutral charge of all the nitrogen forming a neutral environment, which would favor a mechanism such as σ-metathesis. Offering this as an explanation as to why the nitrogen-donor complexes were slower, they labeled the mechanism as the "associative" pathway.

Carrano *et. al* performed similar experiments using the heteroscorpionate complexes [(L1O)ZnSPh] and [(L1S)ZnSPh].[39] These complexes both have at least two nitrogen donors and the third donor is either a sulfur donor or an oxygen donor (Figure 8). Similar to Vahrenkamp and Lippard, kinetics experiments were performed to see the changes in the reaction rate. The results from those kinetics followed the same trend from the previous papers, with [(L1S)ZnSPh] having the highest k_{obs} (1.14×10^{-3} s^{-1}) and [(L1O)ZnSPh] having the lower k_{obs} (4.6×10^{-5} s^{-1}). Based on these results, Carrano *et. al* came to the similar conclusion as Lippard, which was that sulfur coordination increased the probability of thiolate dissociation, and that the primary coordination sphere was responsible for which mechanism occurred when reacting with an electrophile.

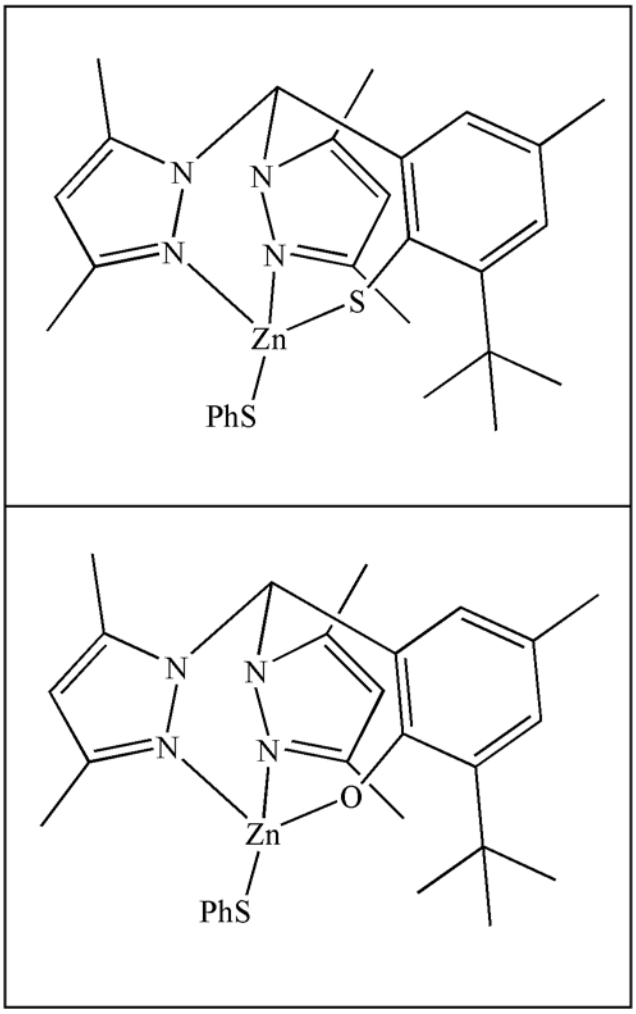

Figure 8. General Structure of Crans' Complex: [(L1O)ZnSPh] and [(L1S)ZnSPh]

Effects of Secondary Coordination Sphere

Based on all of the provided data from previous researchers, it would appear that the major variable that effects how all the complexes react is the primary coordination sphere. But while much of the focus of most research groups was on the primary coordination sphere, there is little data pertaining to how the secondary coordination sphere influences thiolate reactivity. This is surprising, since the solid state structure of the N-terminus of Ada RP obtained by Verdine suggest that hydrogen bonding interactions in the Ada RP active site influence the site of alkylation. [255]

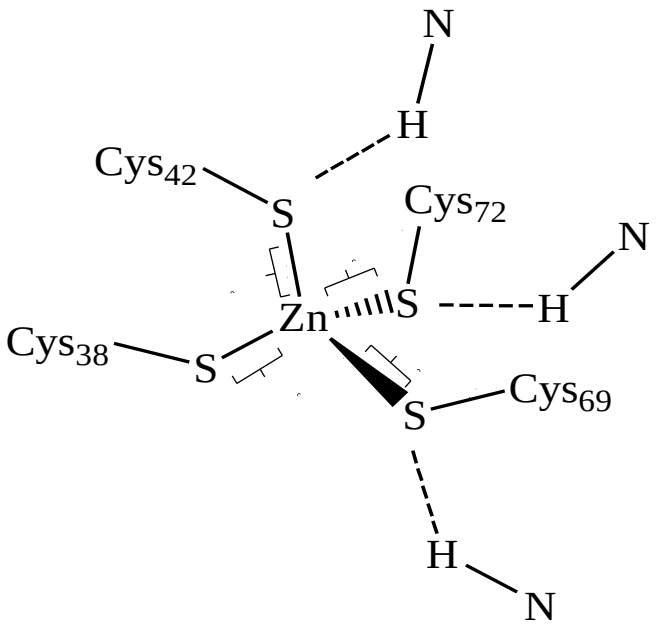

Figure 9. Crystal Structure of the methylated active site of Ada RP with bond distances of the four Zn-S

From Verdine's crystal structure (along with reactivity studies), they determined that Cys-38 was the cysteine that was exclusively methylated.[25] The regiospecificity of the reaction is surprising, since the active site contains four thiolates which are each capable of undergoing alkylation. However, the crystal structure of methylated Ada RP showed that Cys-42, Cys-69 and Cys-72 are all hydrogen-bonded with amide protons on the main protein chain, but Cys-38 is not. The bond lengths for the hydrogen bonded cysteines were shorter (approximately 2.18-2.29 Å), while the methylated Cys-38 had a bond length of 2.47 Å (Figure 9). In another study, Verdine *et. al* replaced Cys-38 with a glycine, and upon addition of an external thiol (methanethiol) and substrate (methyl phosophotriester) the reaction became catalytic.[40] They concluded that although there is a possibility of hydrogen bond donors nearby Cys-38 in non-methylated Ada RP, hydrogen bonding will stabilize and decrease nucleophilicity in cysteines, which makes them less reactive. Evidence supporting this claim comes from both the observed shorter bond

distances and that the reactive cysteine (Cys-38) is devoid of any hydrogen bonding interactions.

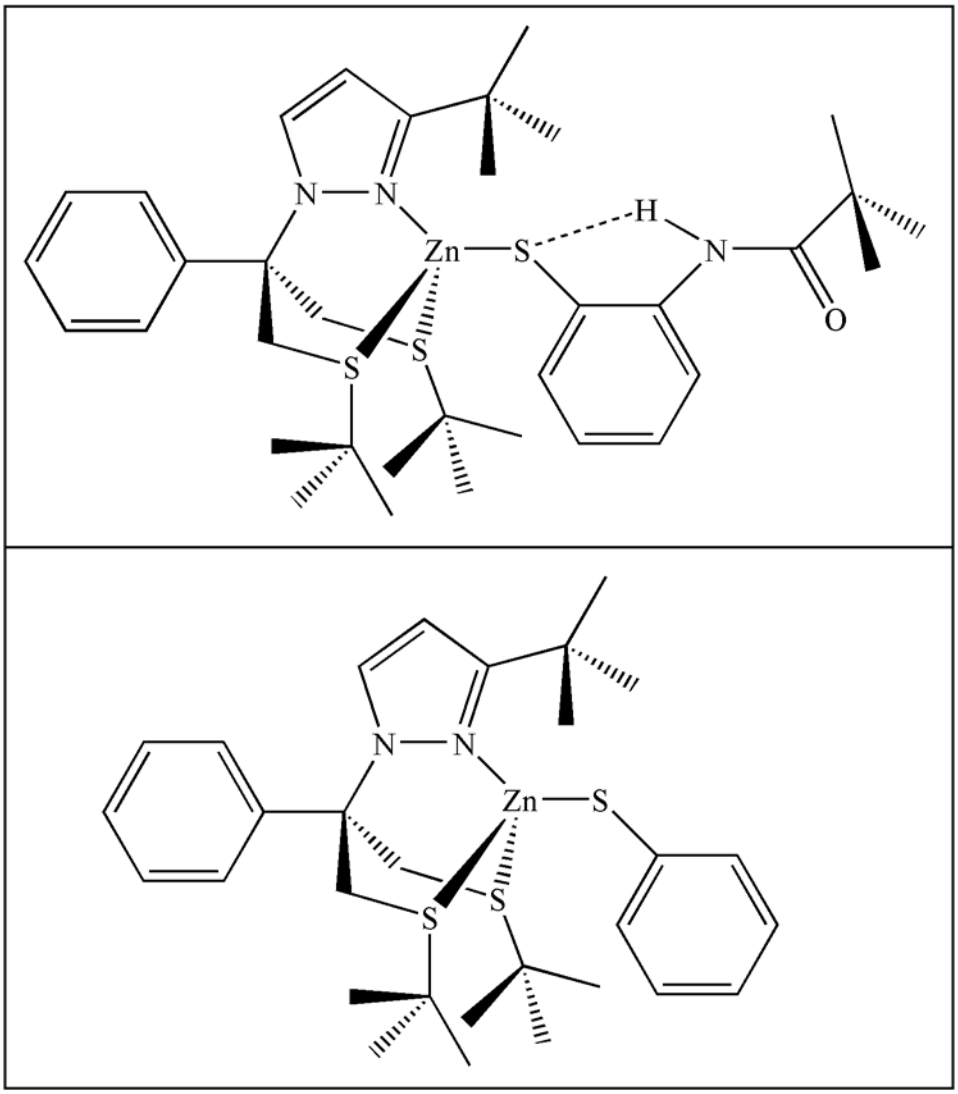

Figure 10. The General Structure of Riordan's Complex: [Ph(pz$^{t\mathrm{Bu}}$)Bt$^{t\mathrm{Bu}}$]Zn(SC$_6$H$_{4o}$-NHC(O)Bu^t) and [Ph(pz$^{t\mathrm{Bu}}$)Bt$^{t\mathrm{Bu}}$]Zn(SC$_6$H$_5$)

Riordan *et. al* concluded a similar finding working with the synthetic analogue [Ph(pz$^{t\mathrm{Bu}}$)Bt$^{t\mathrm{Bu}}$]Zn(SC$_6$H$_{4o}$-NHC(O)Bu^t) (Figure 10).[41] Their synthetic analogue contains a hydrogen bond donor attached to the reacting thiolate. They compared the rate of alkylation (using methyl iodide as the alkylation reagent) to complexes that lacked a hydrogen-bond donor. The complex containing the hydrogen bond donor had a much

smaller second order rate constant ($6.2x10^{-6}$ $M^{-1}s^{-1}$) compared to the complex without a H-bond donor ($2.1x10^{-4}$ $M^{-1}s^{-1}$). Based on this result, they agreed with Verdine's theory that hydrogen bonding will lower the nucleophilicity of the thiolate, which results in lower reactivity.

It would seem based on all the data provided that the primary coordination sphere controls the mechanistic pathway (sulfur-rich coordination environments, as in Ada RP, favor a dissociative mechanism), and that hydrogen bonding interactions reduce the nucleophilicity of a thiolate, making it less likely to undergo alkylation. However, absent from this discussion is whether hydrogen bonding interactions can influence thiolate dissociation, and ultimately the mechanism. As such, no one has explored the idea of strategically placing a hydrogen bond donor(s) onto the ligand scaffolding instead of the reacting thiolate.

We propose as a hypothesis that hydrogen bonding interactions between the hydrogen bond donor and the reacting phenylthiolate can influence thiolate dissociation from the zinc metal ion. The focus of our research was to explore the effect on the alkylation rate of placing a hydrogen bond donor onto the supporting ligand instead of the reacting thiolate. While Riordan's complex contained a hydrogen bond donor, we believe that if the thiolate underwent a dissociative process it would still result in a reduced rate since it departs with the hydrogen bond donor. The hydrogen bonding interaction is not disrupted upon thiolate dissociation, so a reduced rate of alkylation would be observed, which might result in the mechanism being mistakenly assigned as associative instead of dissociative. With the hydrogen donor on the complex itself, we will be able to avoid the

reduced rate (due to the hydrogen staying behind on the scaffolding. This will also allow us to see the effects of the secondary coordination sphere from a different perspective.

Hydrogen Bonding Scaffolding

The ligand systems that were used in this research as the scaffolding for our zinc-thiolate compounds are shown in Figure 11. Tris(2-pyridylmethyl)amine (TPA) was chosen as one of the ligands. [42] The TPA ligand is not intended to mimic the primary coordination environment in Ada RP, since we already know a sulfur-rich environment favors a dissociative pathway. Instead, TPA was chosen due to the relative ease of synthesis and because it can be modified to include an H-bond donor(s). The hydrogen bond donating ligand that was prepared was called *N*-benzyl-6-((bis(pyridin-2-ylmethyl)amino)methyl)pyridin-2-amine (BA-TPA), which can hydrogen bond with the sulfur atom of the zinc-bound thiolate. [43] This will allow us to probe if secondary coordination sphere effects have any influence on the reactivity and mechanism of thiolate alkylation.

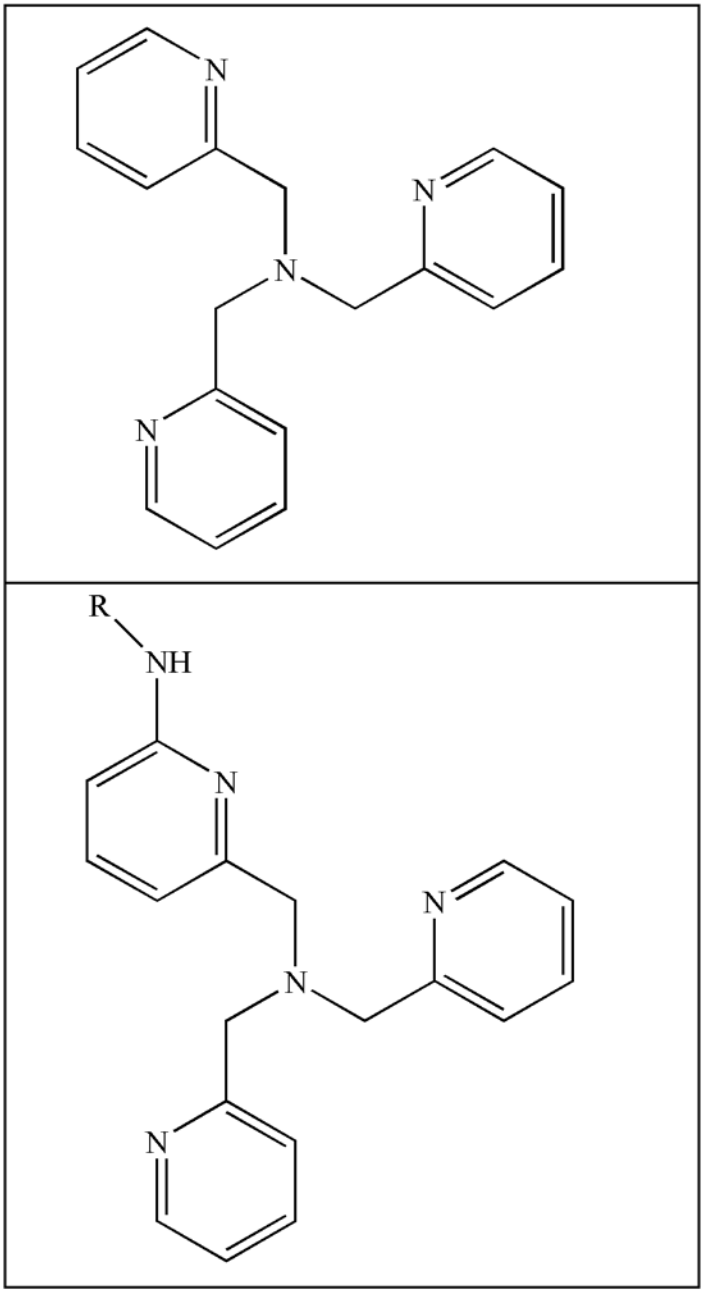

Figure 11. The chosen scaffolding to test the secondary coordination sphere: TPA (Top) and BA-TPA (Bottom) R= CH_2Ph

One of the obvious differences between our planned complexes and the ADA repair protein is the molecular geometry of the active site. While the zinc center in ADA repair protein has a tetrahedral geometry, the zinc ion in both $[(TPA)ZnSPh]^+$ and $[(BA\text{-}TPA)ZnSPh]^+$ have a trigonal bipyramidal geometry. The main reason why we chose

ligand systems that would result in complexes with trigonal bipyramidal geometries is because the extra nitrogen donor is required to prevent demetallation and formation of insoluble zinc-sulfides upon addition of sulfur-containing reagents. Demetallation is particularly problematic for neutral ligands and is often avoided by utilizing anionic ligand systems.

We also expect the thiolate to be in the apical position, which was later confirmed by X-ray crystallography for $[(TPA)Zn\text{-}SPh]^{+}$ (see Chapter 5). From VSPER theory, it is predicted that the apical (axial) ligand will be more sterically crowded due to the three equatorial ligands. Because of this steric crowding, it is assumed if thiolate dissociation occurs then it will occur most readily from the apical position in order to distance itself from the three sterically bulky equatorial ligands (in this case the pyridine rings from the supporting ligands). The reason why the thiolate in the apical position is important is because if the thiolate was in the equatorial position, it would not be in a prime position to leave. As such, the complex would need to perform a pseudo rotation to move the thiolate from the equatorial to the axial position, which is unlikely due to the tetradentate nature of the supporting ligands. Therefore, we believe that the apical position of the thiolate allows for focus on the secondary coordination sphere and its effects on dissociation.

CHAPTER TWO: EXPERIMENTAL

General Methods

All reactions were performed under an inert atmosphere using Schlenk and vacuum line techniques. All solvents (unless otherwise noted) were dried using calcium hydride and distilled prior to use. NMR spectra were recorded on either a Bruker Avance III 600 MHz or 300 MHz NMR. ^{1}H and ^{13}C NMR chemical shifts are reported in ppm and were referenced using residual solvent protons. IR spectra were recorded on a Perkin-Elmer Spectrum 100 FT-IR spectrometer.

General Kinetic Methods

Kinetic experiments were monitored using ^{1}H NMR spectroscopy (Bruker 600 MHz) in CD_3CN and were followed for at least four half-lives. Reactions were ran under pseudo-first-order conditions with methyl iodide being added in excess amounts (ranging from 5-30 fold excess of CH_3I) compared to the zinc-thiolate complex (.03 mmol). (0.03 mmol). 1,4-Di-*tert*-butylbenzene (5.71 mg, 0.03 mmol) was used as an internal standard to ensure accurate integrations. All reactions were ran at a temperature range of 23 °C (295 K). The total volume for every run totaled 0.75 mL.

The NMR data was integrated using specific integration ranges to ensure that the data remained consistent. Rate measurements were taken at five different concentrations of CH_3I. Each complex had a total of five kinetic runs with different equivalences of methyl iodide. Every different equivalent set was ran in triplicate for a total of 15 runs for each complex. The integration values of the experiments were plotted over time in the

data analyzing program IGOR Pro, and a curve fitted on each to find the slope, which would give k_{obs} and error. Every k_{obs} at their respective equivalence was averaged, and each average value plotted versus the concentration of methyl iodide (five data points total) in EXCEL. A LINEST function was performed on the data to find a line of best fit, and the slope of that function (along with the uncertainty) was the second order rate constant for that complex.

Variable Temperature Experiment

An NMR sample of $[(BA\text{-}TPA)ZnSPh]ClO_4$ was added to an NMR tube with 0.7 mL of CD_3CN. Once within the NMR (300 MHz), the NMR probe was then cooled via liquid nitrogen to varying amounts of temperature. Data collection began at room temperature (23°C) and was then cooled down slowly in intervals of 10°C until reaching -30°C (243 K). During each interval, a ^1H NMR spectrum was obtained. At -30 °C a ^{13}C, COSY, HSQC and HMBC spectra were also obtained.

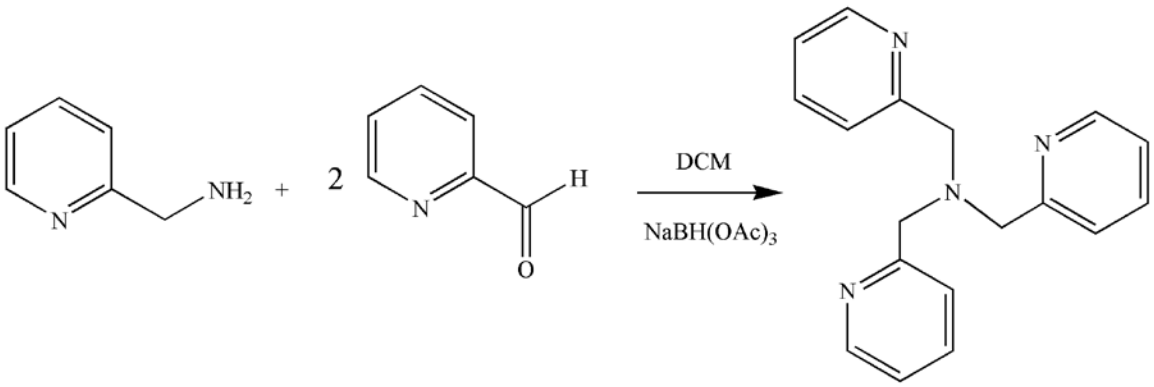

Figure 12. Synthesis of TPA

Synthesis of Tris(2-pyridylmethyl)amine (TPA)

This was prepared according to the synthesis of Dei *et al.* [42] In a dry 250 mL round bottom flask, 2-aminomethyl-pyridine (1.03 mL, 1.049 g, 10 mmol) and dichloromethane (100 mL) were added, along with a stir bar. While stirring, 1.9 mL

(1.126g, 20 mmol) of 2-pyridine-carboxaldehyde was added, and the solution became a clear yellow color. Sodium triacetoxyborohydride (4.24 g, 20 mmol) was then added, and the solution stirred overnight. After stirring overnight, 100 mL of saturated sodium bicarbonate solution was added followed by portions of ethyl acetate (~15 ml each). The organic layer was collected, dried with $MgSO_4$, filtered and the solvent removed by reduced pressure. An oily solid was left behind, with a dark orange color. Pentane (20 mL) was then added to the flask and stirred to extract the product. The pentane solution (yellow in color) was then collected and the solvent removed, leaving an orange solid. Multiple pentane washes were performed to extract the product from the orange solid (0.87 g, 30%). ^{1}H NMR ($CDCl_3$, 600 MHz): δ 3.89 (s, 6H), 7.14 (td, 3H), 7.58 (d, 3H), 7.66 (td, 3H), 8.54 (d, 3H)

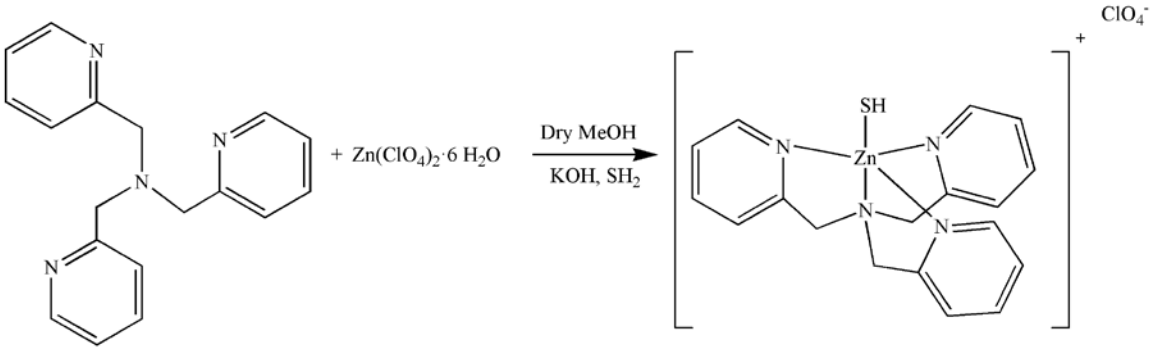

Figure 13. Synthesis of [(TPA)ZnSH]ClO_4

Synthesis of [(TPA)ZnSH]ClO_4

To a solution of tris(2-pyridylmethyl)amine (150 mg, 0.516 mmol) dissolved in dry methanol (30 mL) was added $Zn(ClO_4)_2 \cdot 6H_2O$ (192 mg, 0.516 mmol).[44] After stirring for 5 min, KOH (29 mg, 0.516 mmol) was added to the solution, which caused the formation of a white precipitate. Hydrogen sulfide gas was then bubbled through the solution and the reaction was allowed to stir under an H_2S atmosphere overnight, during which time a yellow precipitate formed. The solid was collected and extracted with

dichloromethane (5 mL). The dichloromethane solution was concentrated and addition of diethyl ether (15 mL) resulted in a yellowish white solid. The solid was collected, washed with diethyl ether (3 x 3 mL) and dried under vacuum (0.14g, 55%). ^{1}H NMR (CD_3CN, 300 MHz): δ -1.55 (s, 1H), 4.12 (s, 6H), 7.51 (d, 3H), 7.6 (t, 3H), 8.03 (dt, 3H), 8.95, (d, 3H). ^{13}C NMR (CD_3CN, 150 MHz): δ155.1, 148.8, 141.1, 125.0, 124.6, 56.4. IR (ATR, cm^{-1}): 3071, 2915, 2020, 1608, 1575, 1484, 1437, 1371, 1316, 1296, 1270, 1160, 1076, 1053, 1021, 981, 908, 838, 766, 733. Anal. Calc. for $C_{18}H_{19}ZnClN_4O_4S$: C, 44.27; H, 3.92; N, 11.47. Found: C, 44.01; H, 3.92; N, 11.29%.

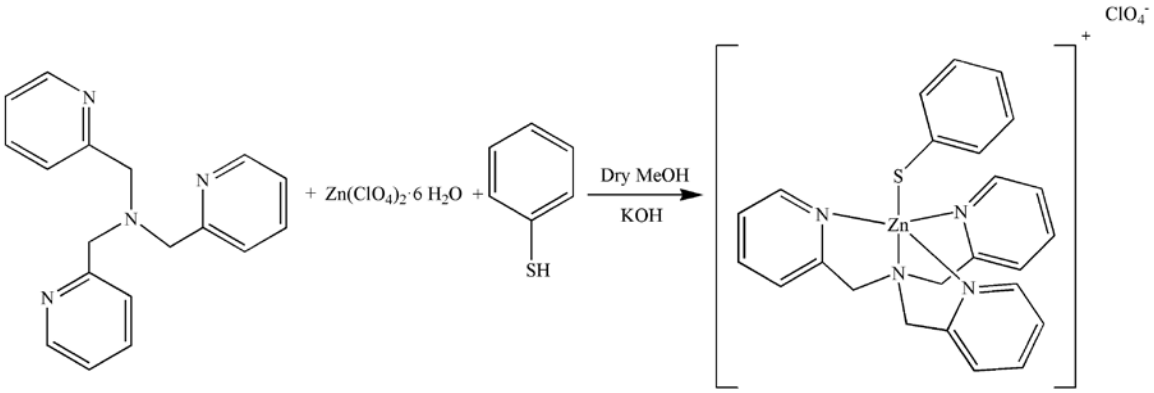

Figure 14. Synthesis of [(TPA)ZnSPh]ClO_4

Synthesis of [(TPA)ZnSPh]ClO_4

To a solution of tris(2-pyridylmethyl)amine (150 mg, 0.52 mmol) dissolved in dry methanol (30 mL) was added $Zn(ClO_4)_2 \cdot 6H_2O$ (192 mg, 0.52 mmol). After stirring for 5 min, KOH (29 mg, .516 mmol) was added to the solution, which caused the formation of a white precipitate. Thiophenol (53 μL, 0.52 mmol) was then added and the reaction was stirred overnight. The solvent was then removed under reduced pressure and the residue extracted with dry dichloromethane (6 mL). The solution was then passed through a celite plug to remove any insoluble solid. The volume was then reduced (~2 mL) by reduced pressure and addition of diethyl ether (2-3 mL) caused the formation of a pale yellow

solid. The solid was collected by fritted filter, washed with multiple amounts of diethyl ether (2 mL each) and dried under vacuum (180 mg, 62%). Colorless crystals suitable for crystallographic characterization were obtained by diethyl ether diffusion into acetonitrile at room temperature. ^{1}H NMR (CD_3CN, 600 MHz): δ 4.18 (s, 6H), 6.92 (m, H), 6.96 (m, 2H) 7.28 (d, 2H), 7.48 (t, 3H), 7.55 (d, 3H), 8.02 (t, 3H), 8.70 (d, 3H). ^{13}C NMR (CD_3CN, 150 MHz): δ 156.7, 150.4, 144.6, 142.6, 133.7, 129.6, 126.6, 126.0, 123.6, 57.9. IR (ATR, cm^{-1}): 3066 (w), 2015 (w), 1942 (w), 1873 (w), 1973 (w), 1730 (w), 1609 (m), 1574 (m), 1483 (m), 1474 (m), 1439 (m), 1370 (w), 1315 (m), 1296 (w), 1269 (m), 1226 (w), 1157 (w), 1128 (m), 1082 (s), 1021 (s), 999 (m), 979 (m), 952 (m), 909 (w), 838 (w), 769 (s), 744 (s), 696 (m).

Synthesis of Dipoclylamine

This was prepared according to the synthesis of Brown et al. [45] In a dry, 250 mL round bottom flask, 4.8 mL (4.8 g, 46.6 mmol) of 2-aminomethylpyridine was added along with dry MeOH (150 mL). Then 4.40 mL (4.93g, 46.6 mmol) of 2-pyridine carboxyaldehyde was added and stirred for 3 hrs. Then 3.52 g (93.07 mmol) of sodium borohydride was slowly added at 0°C and stirred overnight. Concentrated hydrochloric acid was added until a pH of 1 was achieved, whereby the solution became an orange color with a large amount of white precipitate. The solution was stirred for 3 hours. Then a 50 % solution of sodium hydroxide and water was added slowly until a pH of 11 was reached. The solution became a red-orange color, and a large amount of precipitate formed in solution. After allowing the solution to stir for an hour, the solution was passed through a fritted filter to remove any insoluble solids. The solvent from the eluent was then removed to leave behind a red oil. Deionized water (50 mL) was added to the oil and

the product extracted with dichloromethane (3 x 10 mL). The collected dichloromethane layers were dried with anhydrous $MgSO_4$, filtered and the solvent removed to yield an orange colored liquid. (8.8g, 95%) ^{1}H NMR ($CDCl_3$, 600 MHz): δ 3.04 (b, 1H), 3.99 (s, 4H), 7.16 (m, 2H), 7.36 (d, 2H), 7.64 (dt, 2H), 8.56 (d, 2H).

Synthesis of Bromo-TPA

In a 1-neck, 200 mL round bottom flask, 2.25 g (11.29mmol) of dipicolylamine was dissolved in 100 mL of dichloromethane.[43] While stirring, 2.1 g (11.29 mmol) of 6-bromo-2-pyridine carboxaldehyde was added to the mixture. The solution was stirred for 30 minutes, then 2.63g (12.42 mmol) of sodium triacetoxyborohydride was added to the flask and stirred overnight at room temperature.. The solution was then transferred to a 500 mL seperatory funnel where it was washed (3 x 10-15 mL) with a saturated aqueous sodium bicarbonate solution. The collected organic layer was dried with $MgSO_4$, filtered and then the solvent removed to yield a red-brown oil. (3.78g, 90%) ^{1}H NMR ($CDCl_3$, 600 MHz): δ 3.90 (m, 6H), 7.16 (t, 2H), 7.34 (d, 1H), 7.52, (t, 1H), 7.57 (d, 2H), 7.60 (d, 1H), 7.68 (t, 2H), 8.55 (m, 2H).

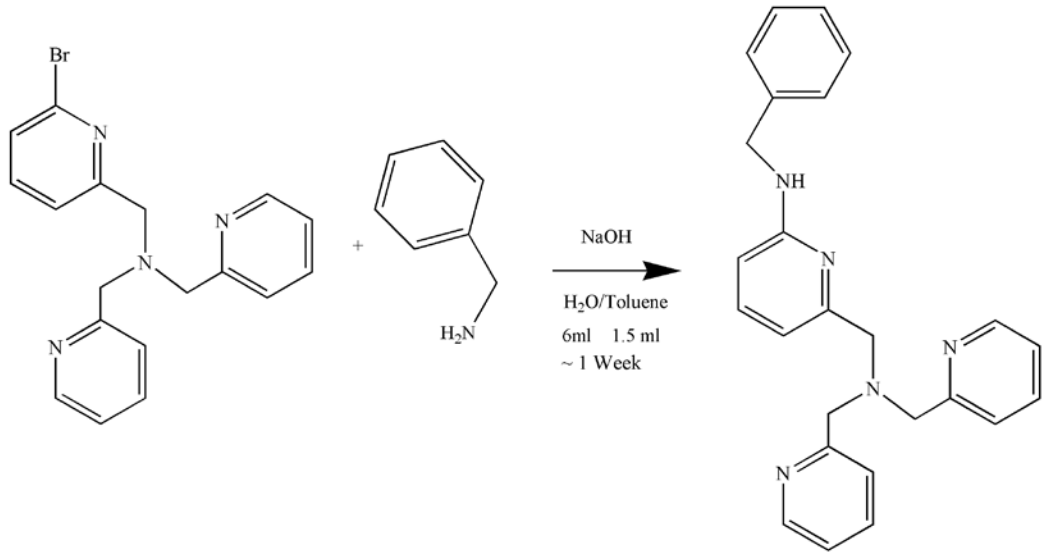

Figure 15. Synthesis of *N*-Benzyl-6-((bis(pyridin-2- ylmethyl)amino)methyl) pyridin-2-amine (BA-TPA)

Synthesis of Benzylamine-TPA (BA-TPA)

This was procedure was modified according to the procedure reported by Karlin et al.[3] In a pressure tube, 1.00 g (2.7 mmol) of bromo-TPA and 2.96 mL (2.90 g, 27 mmol) of benzylamine were added to a mixture containing 6 mL of water, 1.5 mL of toluene and 0.0521 g (1.3 mmol) of NaOH. The pressure tube was sealed and heated to 160° C in an oil bath. After heating for seven days, the solution was cooled to room temp. The solution was then extracted with t dichloromethane (3 x 15 mL). The dichloromethane was collected, dried with $MgSO_4$, filtered and the dichloromethane removed under reduced pressure. A short path distillation was used to remove unreacted benzylamine (125 °C at 0.05 torr). The distillation was followed by ^{1}H NMR until all impurities were removed, leaving behind the BA-TPA ligand, which was an orange oil. (0.70g, 65.6 %) ^{1}H NMR (CD_3CN, 600 MHz): δ 3.57 (s, 2H), 3.79 (s, 4H), 4.53 (m, 2H), 5.60 (b, N-H, 1H), 6.31 (d, 1H), 6.74 (d, 1H), 7.16 (t, 2H), 7.20 (t, 1H), 7.28 (t, 2H), 7.35 (m, 3H), 7.60 (d, 2H), 7.67 (td, 2H), 8.46 (d, 2H).

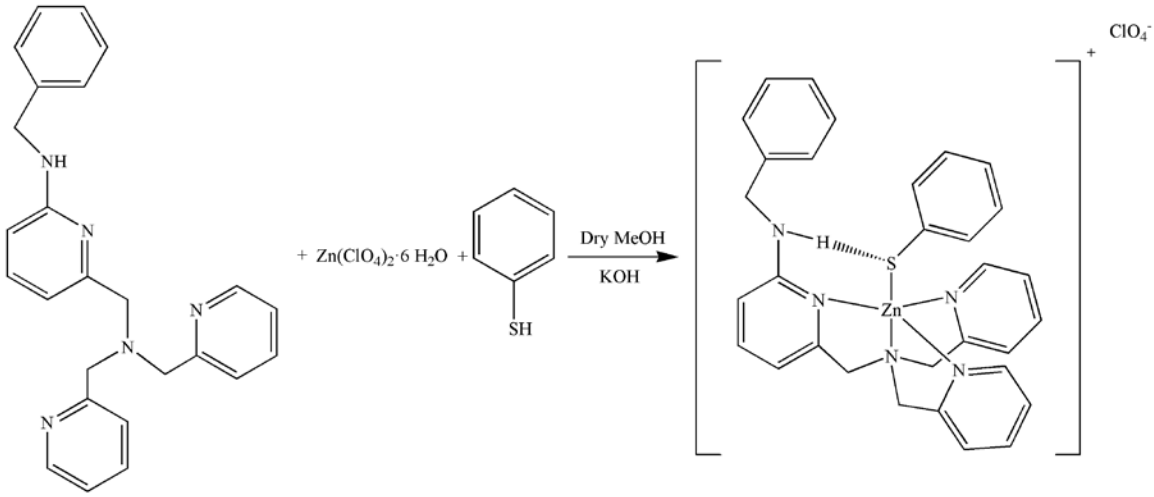

Figure 16. Synthesis of [(BA-TPA)ZnSPh]ClO_4

Synthesis of [(BA-TPA)ZnSPh]ClO_4

To a solution of *N*-benzyl-6-((bis(pyridin-2- ylmethyl)amino)methyl)pyridin-2-amine (BA-TPA) (150 mg, 0.379mmol) dissolved in dry methanol (30 mL) was added $Zn(ClO_4)_2 \cdot 6H_2O$ (145 mg, 0.379 mmol). After stirring for 5 min, KOH (22 mg, 0.379 mmol) was added to the solution with little visible change. Thiophenol (40 μL, .379 mmol) was then added and the reaction was stirred overnight. The solvent was removed under reduced pressure and the residue extracted with dry dichloromethane (6 mL). The solution was then passed through a celite plug to remove any insoluble solid. The volume was reduced (~2 mL) by reduced pressure and addition of diethyl ether (2-3 mL) caused the formation of a pale yellow solid. The solid was collected by filtration, washed with diethyl ether (3 x 2 mL) and dried under vacuum (180 mg, 62%). Colorless crystals suitable for crystallographic characterization were obtained by diethyl ether diffusion into acetonitrile at room temperature. ^{1}H NMR (CD_3CN, 600 MHz): δ 4.02 (s, 2H), 4.16 (m, 6H), 6.44 (d, 1H), 6.67 (d, 1H), 7.04 (m, 5H), 7.22 (m, 4H), 7.34 (m, 3H), 7.57 (m, 5H), 8.05 (t, 2H), 8.69 (d, 2H), 9.23 (b, 1H). ^{13}C NMR (CD_3CN, 150 MHz): δ 160.5, 155.1, 152.6, 149.0, 141.2, 141.1, 137.6, 132.3, 128.5, 127.2, 127.1, 125.0, 124.6, 123.2, 112.0, 107.4, 57.0, 55.9, 46.0. IR (ATR, cm^{-1}): 3238 (w), 3067 (w), 2928 (w), 2857 (w), 2170 (w), 2019 (w), 1976 (w), 1698 (w), 1610 (m), 1576 (m), 1526 (w), 1478 (m), 1438 (m), 1365 (w), 1345 (w), 1321 (w), 1286 (w), 1173 (w), 1082 (s), 1022 (s), 1004 (m), 925 (w), 905 (w), 840 (w), 739 (s), 692 (s), 664 (m).

Trapping Experiment

To perform this experiment, 10 mg (0.018 mmol) of [(TPA)ZnSPh]ClO_4 and 11.9 mg (0.018 mmol) of [(BA-TPA)ZnSPh]ClO_4 were added into separate NMR tubes, along

with 3.4 mg (0.018 mmol) of 1,4-ditertbutylbenzene as a internal standard. Each sample tube had 0.7 mL of deuterated acetonitrile added as the solvent, and a ^{1}H NMR taken as a pre-addition run. Then approximately 2.2 mg (0.018 mmol) of N-ethylmaleimide was added to each sample. The reaction was followed by ^{1}H daily to see if a reaction had occurred. Another set of tubes were prepared the exact same way as the previous set, but N-ethylmaleimide was added in ten-fold excess (22 mg, .177 mmol) to ensure complete reaction with each complex.

CHAPTER THREE: SYNTHESIS AND VARIABLE TEMPERATURE

Synthesis of [(TPA)ZnSPh]ClO_4

The synthesis of [(TPA)ZnSPh]ClO_4 began by taking the scaffolding ligand tris(2-methylpyridyl)amine (TPA) and reacting it with $Zn(ClO_4)_2 \cdot 6H_2O$. Reaction of the TPA ligand and zinc perchlorate salt results in the formation of a zinc aqua complex of the form [(TPA)Zn-OH_2]$(ClO_4)_2$. Deprotonation of the zinc aqua complex with base (KOH) and reaction with thiophenol results in the product [(TPA)Zn-SPh]ClO_4, where the sulfur atom of the thiolate is bound to the zinc ion, in a yield of 55% after workup. The zinc thiolate compound was characterized by NMR (^1H, ^{13}C, COSY, HSQC and HMBC) and IR spectroscopies along with x-ray crystallography.

The ^1H NMR (Appendix A1 and A2) provides evidence that the complex was synthesized and the proposed connectivity is correct. Peaks representing the phenyl group of the thiophenolate were observed as two multiplets at 6.92 and 6.96 ppm and as a doublet at 7.28 ppm. In addition to the thiolate phenyl peaks, the proton resonances for the TPA ligand are observed. Likewise in the ^{13}C NMR spectrum (Appendix A3 and A4), a total of ten peaks are observed, which matches the number of peaks predicted based off the symmetry of the compound, with peaks at 144.6, 133.7, 129.6 and 123.6 ppm representing the thiolate aromatic ring carbon resonances. The COSY spectrum (Appendix A5 and A6), provided information concerning which proton resonances were coupled to each other (i.e. the TPA and thiolate spin systems could be distinguished from each other and the connectivity of each neighboring proton within each spin system

determined). The HSQC (Appendix A7 and A8),, which allows the heteronuclear correlation between hydrogen and carbon atoms separated by a single bond, allowed assignment of the ^{13} C. Finally, the HMBC (Appendix A9 and A10), which provides heteronuclear correlations over 2-4 bonds, allowed us to assign the quaternary carbon of the thiolate. For instance, the peak in the ^{13}C at 144.6 ppm (which had no carbon/hydrogen correlation in the HSQC) correlated with the two multiplets at 6.92 ppm and 6.96 ppm, which are the hydrogen atoms in the ortho and meta positions of the thiolate aromatic ring. The infrared spectrum (Appendix A11) shows two strong aromatic peaks at 2015 cm^{-1} and 1730 cm^{-1}, consistent with the monosubstituted benzene of the thiophenolate.

Synthesis of [(BA-TPA)ZnSPh]ClO_4

The synthesis of [(BA-TPA)ZnSPh]ClO_4 is similar to [(TPA)ZnSPh]ClO_4. *N*-benzyl-6-((bis(pyridin-2- ylmethyl)amino)methyl)pyridin-2-amine (BA-TPA) and $Zn(ClO_4)\bullet 6H_2O$ initially form a zinc-aqua complex that is then reacted with KOH and thiophenol to give [(BA-TPA)ZnSPh]ClO_4 in a 62% yield after workup. Similar to the [(TPA)ZnSPh]ClO_4 complex, characterization of [(BA-TPA)ZnSPh]ClO_4 was done by IR and NMR (^{1}H, ^{13}C, COSY, HSQC and HMBC) spectroscopies.

In the ^{1}H NMR (Appendix B1 and B2), the best evidence that this reaction was successful was the downfield shift of the secondary amine proton, contained in the scaffolding of the BA-TPA. In free BA-TPA (with no zinc ion bound), the amine proton appears at 5.62 ppm in the ^{1}H spectrum. In [(BA-TPA)ZnSPh]ClO_4, the secondary amine appears at 9.23 ppm. This downfield shift is a result of the secondary amine's proton hydrogen bonding with the sulfur atom of the zinc-bound thiophenolate. Hydrogen

bonding makes the amine proton shift downfield due to a lower electron density. This means the thiophenol was able to bind with the zinc, and that the hydrogen bonding effect is occurring on the sulfur of the thiophenolate. The thiophenolate aromatic proton peaks are also observed within the spectrum from 7.70 ppm to 6.90 ppm. The location of these peaks are similar to [(TPA)ZnSPh]ClO_4, except the thiophenolate peaks in [(BA-TPA)ZnSPh]ClO_4 are very broad with little resolved spin-spin coupling (the significance which will be discussed later).

The COSY (Appendix B5 and B6) gave further proof of synthesis, but due to the broadness of the peaks and how close they were, it was difficult to discern with certainty which peaks were correlated. In terms of the ^{13}C NMR (Appendix B3 and B4), the spectrum showed all the peaks of the BA-TPA ligand, but only three carbon peaks of the thiophenolate were observed. These peaks were observed at 132.2, 128.5 and 123.2 ppm and all correlated to protons on the thiophenolate as evident from the HSQC (Appendix B7 and B8) spectrum. However, these three carbon peaks were very broad and the fourth carbon peak (the quaternary carbon of the thiophenolate) was missing in the room temperature spectrum. The infrared spectrum showed aromatic peaks from 2020 cm^{-1} to 1976 cm^{-1} (Appendix B11, although they were not as discernable as they were in the [(TPA)ZnSPh]ClO_4. The IR also provided evidence of the secondary amine, with peaks for N-H stretching and N-H wagging occurring at 3238 cm^{-1} and 739 cm^{-1}, respectively. Overall, the NMR and IR data provided evidence that the synthesis was successful, but due to broadness of peaks and peak overlap it was difficult to discern and assign peaks. As such, a variable temperature experiment was performed to determine if the peak broadness in the ^{1}H and ^{13}C NMR spectra was due to a fluxional process.

Broad Peaks and Variable Temperature NMR

The peaks that pertain to the thiophenolate in both complexes are shown in Figure 17. As evident from the top spectrum in the figure, the thiophenolate peaks (labeled “e”, “f” and “g”) of the $[(TPA)ZnSPh]^+$ complex are sharp with observable spin-spin splitting. The spectrum on the bottom depicts the thiophenolate peak range of the $[(BA\text{-}TPA)ZnSPh]^+$ complex, with peaks that are broad and have no discernable splitting (specifically, peaks labeled as “g”, “h” and “k” in Figure 17). The rationale for the cause of this broadness in the spectrum of $[(BA\text{-}TPA)ZnSPh]^+$ is believed to be due to thiolate dissociation, which is occurring quickly on the NMR time scale. This phenomenon of thiolate dissociation is similar to what Lippard observed with $[Zn(SC_6H_5)_4]^{2-}$, as the thiophenolate proton peaks were broad as well. However, thiolate dissociation was only witnessed for complexes in a sulfur-rich primary coordination sphere environment, not a nitrogen-rich coordination environment like the $[(BA\text{-}TPA)ZnSPh]^+$ complex. This implies that the hydrogen bonding interaction in $[(BA\text{-}TPA)ZnSPh]^+$ is causing thiolate dissociation, which is absent (observe sharp thiophenolate peaks) in $[(TPA)ZnSPh]^+$, which lacks a H-bond donor. However, in order to confirm that a fluxional thiolate dissociation process is operating in $[(BA\text{-}TPA)ZnSPh]^+$, a variable temperature NMR study of the $[(BA\text{-}TPA)ZnSPh]^+$ complex was necessary.

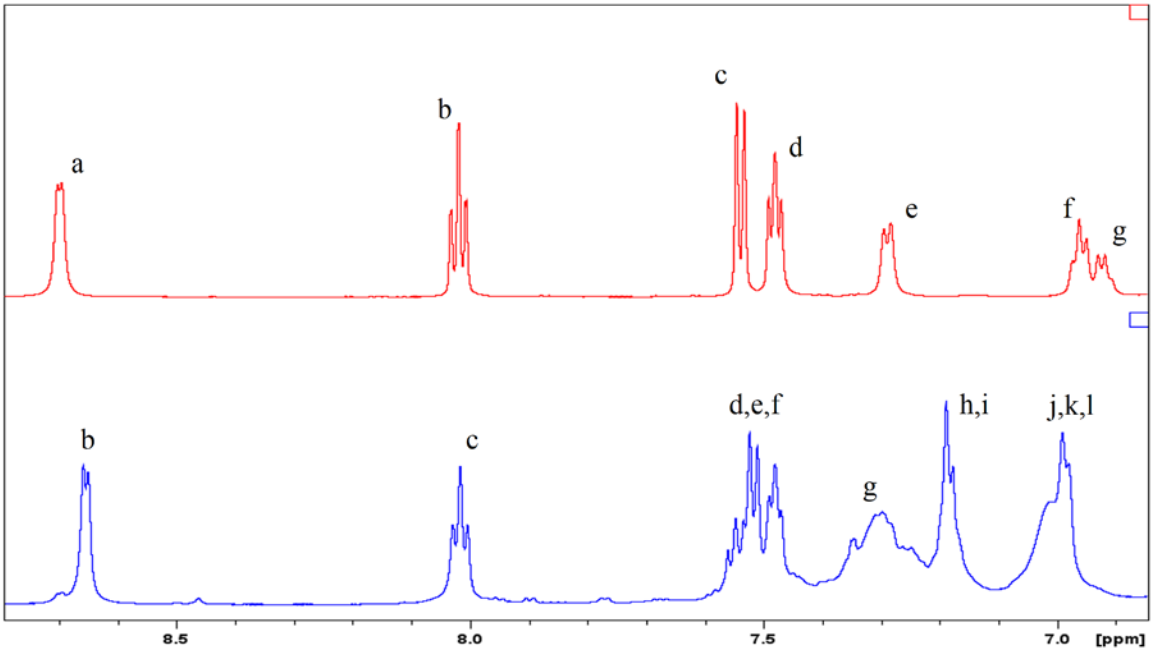

Figure 17. Thiophenolate aromatic peak regions of $[(TPA)ZnSPh]^+$ (top) and $[(BA\text{-}TPA)ZnSPh]^+$ (bottom). The labeled products can be found within the appendix.

To be able to discern if the broadness of the thiophenolate resonances are due to a fluxional process, a variable temperature NMR experiment was performed. The proposed reason for the broadness within the NMR spectrum is due to thiolate dissociation from the zinc-bound thiolate complex (as shown in Figure 18).

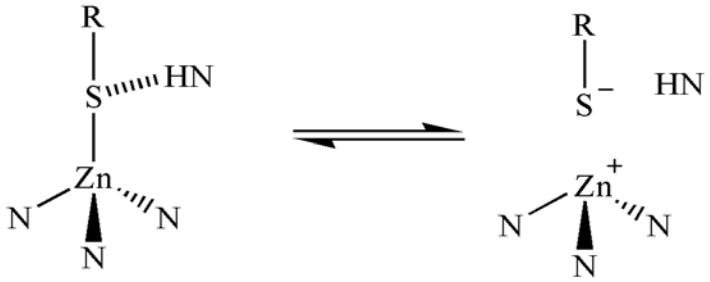

Figure 18. Theoretical resonance occurring during NMR acquisition with $[(BA\text{-}TPA)ZnSPh]^+$. Cooling down the sample may lead to resonance favoring the left molecule

The exchange between the zinc-bound thiolate and the free thiolate in $[(BA\text{-}TPA)ZnSPh]^+$ is rapid (fast exchange) on the NMR time scale resulting in an average signal (broad peak) with no discernable features. In theory, when the sample in the NMR

is cooled down, the rate of dissociation should slow down. This cooling should also favor the zinc-bound thiolate species at low temperatures. Therefore, upon cooling, the thiophenolate should sharpen and become more distinct. To perform this experiment, several ^{1}H NMR spectra were taken over different temperatures (23 °C to -30 °C) of $[(BA\text{-}TPA)ZnSPh]^{+}$ in CD_3CN. When the temperature reached -30 °C, a ^{13}C, COSY, HSQC and HMBC were also taken of the sample.

Variable Temperature ^{1}H NMR Results

The results of the variable temperature ^{1}H NMR study are shown in Figure 19 (can also be seen in Appendix C1 and C2). From the figure, there is a noticeable change within the proton peaks. The first major difference is that the secondary amine proton peak (at 9.23 ppm in the 23°C ^{1}HNMR spectrum and labeled as "a" in Figure 19) has changed. Originally, it was a broad peak, but as the temperature is lowered, the peak begins to sharpen and spin-spin coupling becomes apparent (a triplet is observed). This is significant, as this splitting means the amine proton is seeing/being influenced by the magnetic interaction of the protons on the adjacent secondary carbon, which would be expected if cooling the sample shifted the equilibrium to the zinc-bound thiolate complex. Furthermore, the secondary amine proton shifts downfield from 9.23 ppm to 9.47 ppm as the temperature is lowered. This downfield shift is consistent with the species observed at low temperatures being the zinc-bound thiolate complex, due to the stronger hydrogen bonding interaction in the zinc-bound thiolate complex (a stronger H-bonding interaction will result in a decrease in the amount of electron density on the hydrogen resulting in a downfield shift).

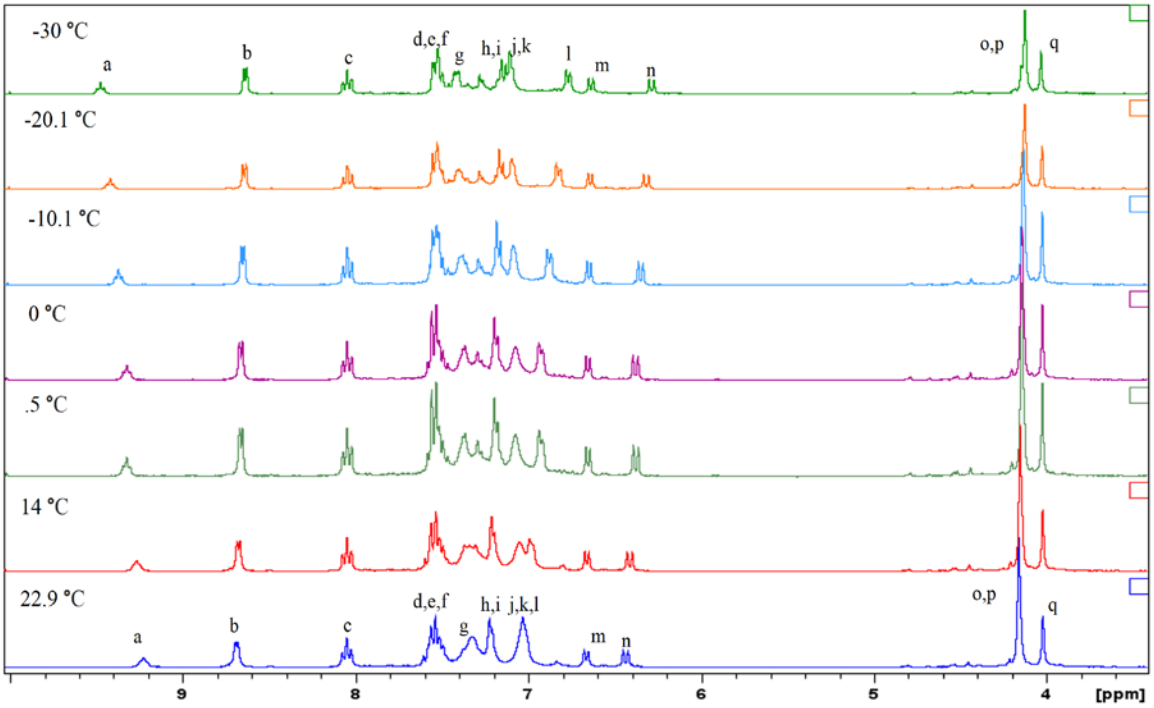

Figure 19. Results of the variable temperature experiment over lowering temperatures (^{1}H NMR spectra)

The other major result from the VT NMR study is the difference in some of the aromatic peaks in both the thiophenolate and the benzylamine. As the temperature is lowered to -30 °C, many of the aromatic peaks begin to shift either upfield or downfield, as well as spin-spin splitting becoming more apparent. One of the obvious peak shifts when comparing the 23 °C and -30 °C spectra is the shift of the ortho protons (labeled as "l") of the benzylamine group of the scaffolding ligand. At room temperature (23° C), the benzylamine peak at 7.03 ppm is a large, broad peak containing multiple peaks (the HSQC provides evidence that there are three peaks corresponding to protons attached to three unique carbon atoms; peaks labeled as j, k and l in Figure 19) that coincidently overlap with one another. However, when cooled down to 14 °C, the broad peak begins to split and forms two peaks. As the sample is further cooled, the downfield broad peak (this peak contains two overlapping peaks) at 7.1 ppm hardly moves, while the other peak

begins to move significantly upfield. The peak that is moving upfield also begins to sharpen and exhibit spin-spin coupling, revealing a doublet. At -30 °C the chemical shift of the peak is observed at 6.77 ppm. From the COSY, HSQC and HMBC characterization data obtained at -30 °C, this peak was identified to be the ortho protons on the benzylamine aromatic ring. This movement can be seen especially when comparing the HSQC (Appendix C7 and C8), as the carbon that the proton is bonded with remains the same in the ^{13}C NMR, but the position of the peak in the ^{1}H NMR moves (labeled as "l" in Figure 20) upon lowering the temperature. The rational for the upfield shift for the ortho protons but not the meta and para protons on the benzylamine may be due to magnetic anisotropic shielding of the ortho protons by the thiophenolate aromatic ring. However, in lieu of an X-ray crystal structure for $[(BA\text{-}TPA)ZnSPh]^{+}$, the rationale is conjecture.

The other peak that splits off from this large peak slightly moves downfield. While this peak at 7.12 ppm does begin to sharpen, no real splitting (there is a shoulder) is observed. However, the HSQC taken at -30 °C does clearly show there is two proton peaks overlapping with each other (Figure 20), and both of them scarcely move during the cooling. From examination of the two spectra, the protons assigned to the overlapping peaks that barely shift are 1) the proton para to the quaternary carbon on the benzylamine, and 2) the two protons that are meta to the quaternary carbon on the thiophenol (labeled as "j" and "k" respectively in Figure 20).

Another peak that shifted upfield was the peak at 7.22 ppm (labeled as h,i in Figure 19) at 23°C. This peak originally started as a broad multiplet, but as the temperature was cooled, it began to move upfield slightly. Eventually, this peak at -30 °C

nearly merges with the previously mentioned peak at 7.12 ppm. However, before it merges, it can be seen at -20°C that the broad multiplet has sharpened enough that two peaks could be observed. When the HSQC of both the room temperature and -30 °C spectra are reviewed, there is confirmation that the two protons are in fact overlapping with each other. These protons were identified as 1) the two protons that are ortho to the quaternary carbon on the thiophenolate, and 2) the two protons meta to the quaternary carbon on the benzylamine (labeled as “h” and “i” respectively in Figure 20).

The last peak of interest occurred at 7.34 ppm (labeled as “g” in Figure 19 and 20). When the temperature was at 22.9 °C, the peak was a wide, broad peak with no visible splitting. As the temperature of the sample was lowered, the peak began to form a slightly sharper peak while another peak split off from it. The peak that shifted slightly downfield to 7.41 ppm was identified to be the proton in the para position from the quaternary carbon of the thiophenolate. The identity of the other peak splitting upfield to 7.27 ppm (labeled as a circle in Figure 20) is an impurity and was not fully identified. One idea is that the impurity is unreacted benzenethiol (consistent with chemical shifts).

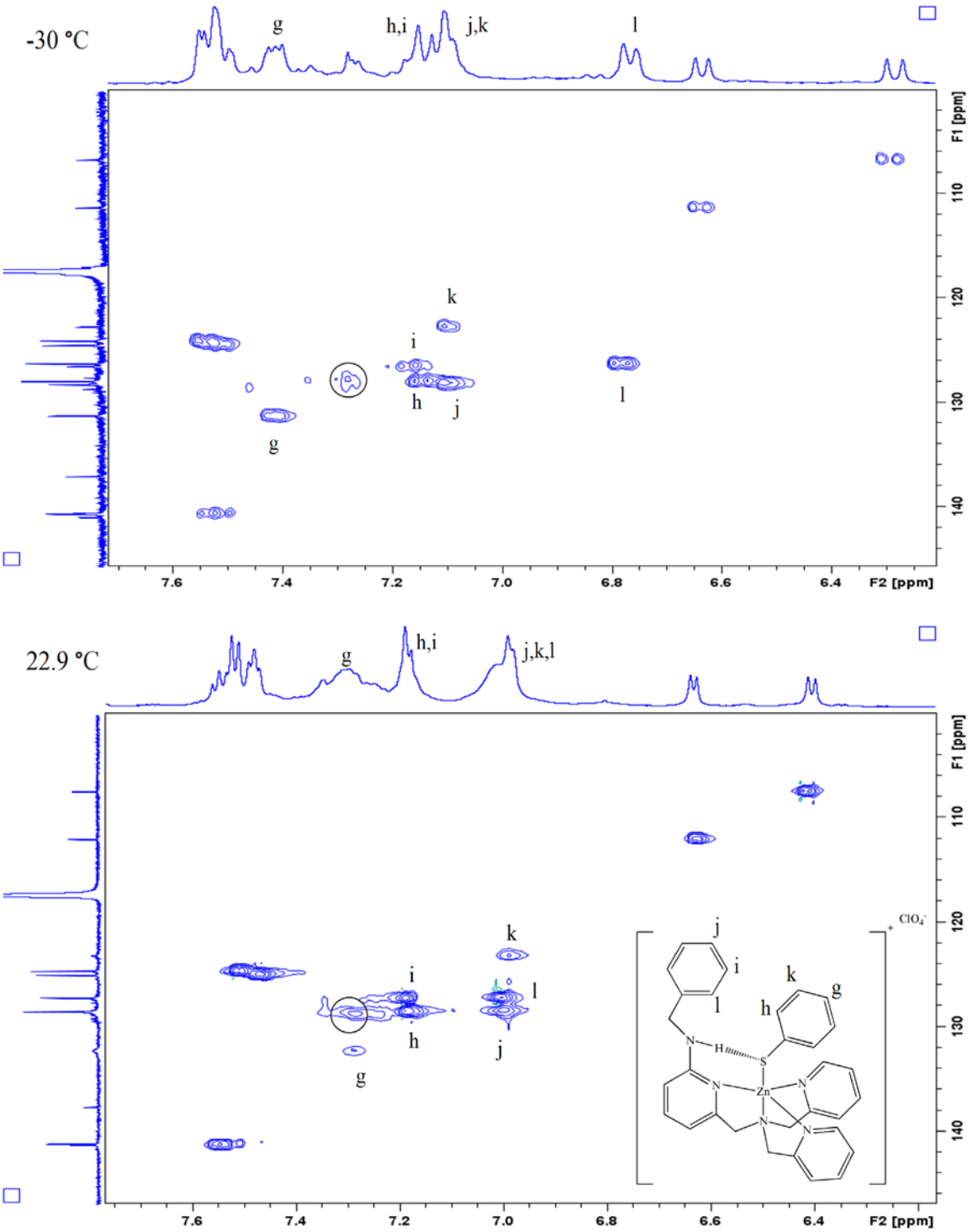

Figure 20. HSQC comparison of $[(BA\text{-}TPA)ZnSPh]^+$ at 22.9 °C and -30°C. The peaks that are labeled pertain to proton peaks that shifted when the sample was cooled. The circle represents refers to a possible impurity within the sample

Variable Temperature ^{13}C NMR Results

The fact that we are seeing differences in the ^{1}H NMR spectra at different temperatures gives credibility to the theory that thiolate dissociation can occur with secondary coordination effects. However, ^{1}H NMR results were not the only evidence from the variable temperature experiment. Not only are there differences in the ^{1}H NMR spectra when cooled, but there were visible differences in the ^{13}C NMR spectra as well (which can be seen in Appendix C3 and C4). Based on the structure of [(BA-TPA)ZnSPh]$^{+}$ as shown in Figure 16, one would expect to observe four different peaks in the ^{13}C NMR spectrum for the thiophenolate ligand. One important observation was that the thiophenolate carbon peaks were either broad (peaks labeled I and P) or missing (peaks labeled G and K) in the room temperature ^{13}C spectrum of [(BA-TPA)ZnSPh]$^{+}$. However, once the sample is cooled to -30 °C, the two missing peaks (G and K) appear and the broad peaks (I and P) sharpen. Based on the HMBC, the most downfield thiophenolate carbon peak (labeled as "G" in Figure 21) at 141.9 ppm was identified to be the missing quaternary carbon of the thiophenolate. This assignment was made based not only due to there being no proton attached to that carbon (based off the HSQC), but also because the carbon is correlated to several thiophenolate protons in the HMBC. We would also expect it to be the most downfield peak since it is directly attached to the sulfur heteroatom. The peak at 128.5 ppm (labeled "K" in Figure 21) was also missing in the room temperature spectrum but appears in the -30 °C spectrum. This peak represents the two ortho carbons ("K") of the thiophenolate ligand.

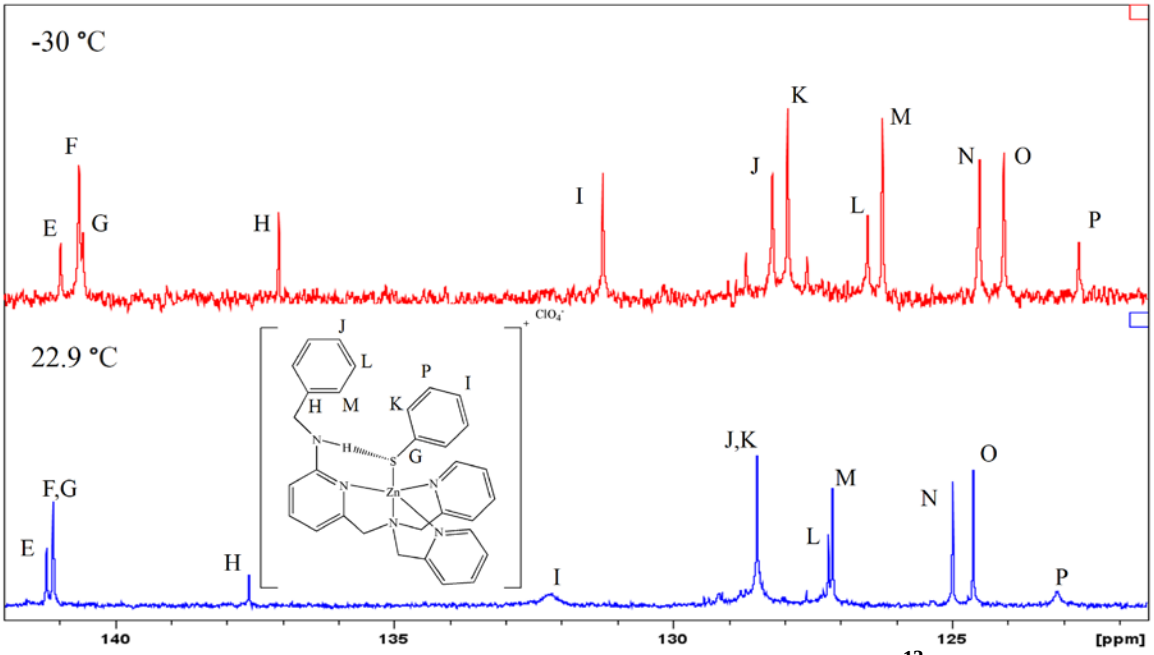

Figure 21. Results of the variable temperature experiment on ^{13}C NMR spectra

The two other broad peaks that became sharp are the peaks at 132.3 ppm ("I") and 123.2 ppm ("P"). Unlike the previous peaks, these two peaks are short and broad and are not overlapping with other peaks at room temperature. Once the sample is cooled, these peaks become sharp and tall. These peaks were identified to be the carbons that are meta and para to the quaternary carbon on the thiophenolate (based on the HSQC and HMBC).

The significance of the dynamic behavior in the ^{1}H and ^{13}C NMR is consistent with thiolate dissociation in $[(BA\text{-}TPA)ZnSPh]^{+}$ being rapid at room temperature but slow at low temperature, with the zinc-bound thiolate complex being the major species at low temperature. Lippard et al. observed similar peak broadening in his complexes due to thiolate dissociation, but peak broadening was only observed with complexes in sulfur-rich primary coordination environments.[32] Our results show that the primary coordination sphere is not the only possible source that influence thiolate dissociation. When hydrogen bonding is introduced in our complexes, thiolate dissociation occurs, even though the

zinc ion is in a nitrogen-rich environment. Our results give credibility to our hypothesis that secondary coordination effects may also influence which pathway Ada RP takes.

CHAPTER FOUR: KINETICS AND TRAPPING EXPERIMENT

Kinetics

A kinetics study examining the alkylation of our zinc thiolate complexes was undertaken to develop a better understanding of the thiolate alkylation mechanism. Typical kinetics runs consisted of preparing NMR tubes containing zinc complex ([(BA-TPA)ZnSPh]ClO_4, [(TPA)ZnSPh]ClO_4 or [(TPA)ZnSH]ClO_4) and 1,4-di-tert-butylbenzene (integration standard) in 1:1 ratio in dry CD_3CN. A ^1H NMR spectrum was taken prior to the addition of the electrophile. The electrophile used for the alkylation experiments was methyl iodide (ranging from 5-30 fold excess of CH_3I relative to the zinc-thiolate). Methyl iodide was used instead of alkylated DNA due to its inexpensive cost. Once methyl iodide was injected, the reaction was followed by ^1H NMR for at least four half-lives. The number of scans for each kinetic run varied, as the time required to reach four half-lives varied based on the amounts of methyl iodide used. Each kinetic run was repeated three times, and the averaged data were reported.

The kinetic study was carried out with an excess of methyl iodide (flooding technique) in order to simplify the kinetics. The general rate equation for a second order reaction is rate = $k[A]^x[B]^y$. [46] One of the challenges of performing kinetics on a reaction like this is in order to get an accurate rate constant, the concentrations of both reagents needs to be followed closely. To make it easier for one to obtain the rate constant, the method of flooding allows us to treat the second-order reaction as a first-order reaction. What this involves is literally flooding the reaction with a large amount of one of the

reagents of the reaction. For example, let's assume for one sample the concentration of [B] is at least twenty times in excess compared to [A]. This in turn will make [A] the limiting reagent. After the reaction has gone to completion, [A] will have been completely reacted. The concentration of [B], however, will have remained relatively unchanged. This allows [B] to be treated as a constant variable ($[B]_o^{\,y}$). The form of the rate equation can then be changed from rate = $k[A]^x[B]^y$ to rate = $k_{obs}[A]^x$, where $k_{obs}=k[B]_o^{\,y}$. In essence, the secondary rate equation has now become a pseudo-first order equation.

This pseudo-first order reaction is important, as it is now possible to perform kinetics in a more efficient and accurate manner. Since $k_{obs} = k[B]_o^{\,y}$, the second-order rate constant "k", can be found by plotting k_{obs} versus $[B]_o^{\,y}$. In order to make this plot, the kinetics of [A] with different equivalents of [B] is required. The equivalents can vary, but the important condition of the experiment is that [B] must be in a large excess. Once these kinetics are performed and plotted, the graph should be exponential, due to it being pseudo-first order. To find k_{obs}, one takes the ln [A] versus time, which should give a straight line if the reaction is first order. Since the integrated rate law of a first order reaction ($\ln[A] = -k_{obs}t + \ln[A_o]$) is in the form y = mx+b, k_{obs} is the slope of the plot. After performing mulitple kinetic experiments, the collected k_{obs} values were plotted versus [B] to find the second-order rate constant "k".

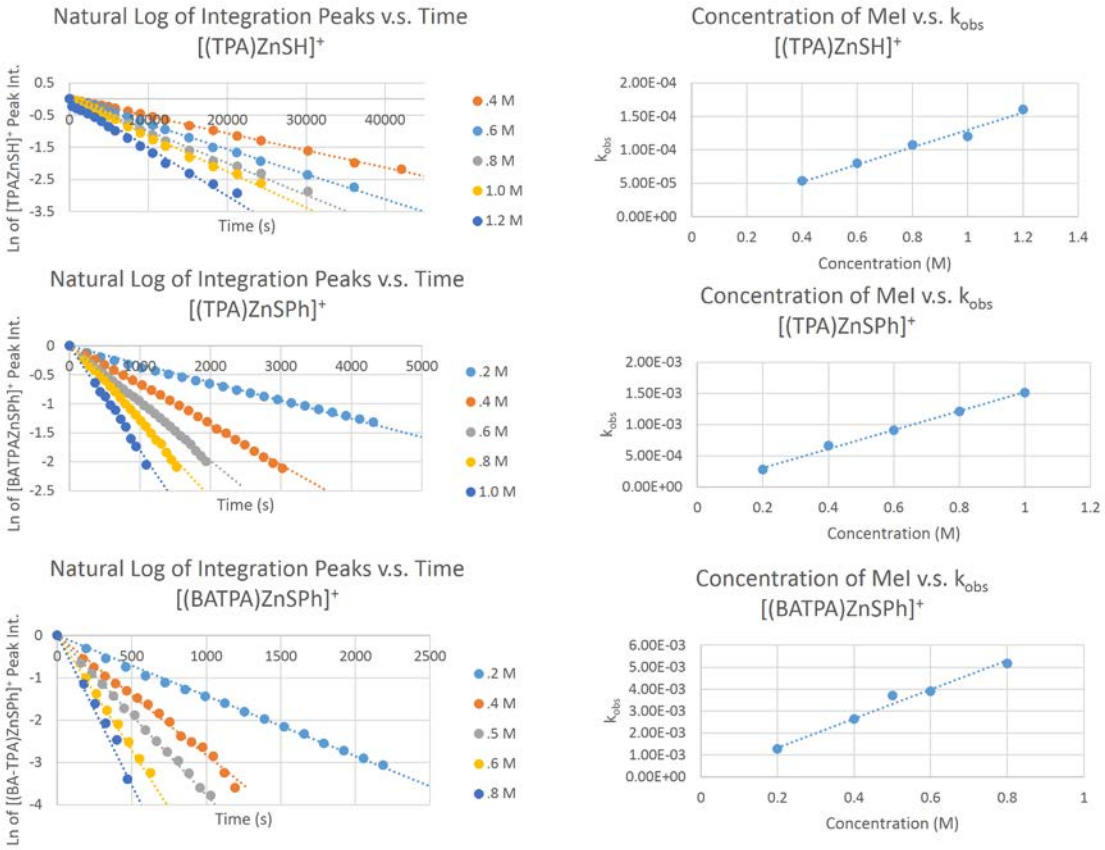

Figure 22. Natural log of kinetics versus time (left) and concentration versus k_{obs} values (right) from multiple concentrations of methyl iodide for the $[(TPA)ZnSH]^+$, $[(TPA)ZnSPh]^+$ and $[(BA\text{-}TPA)ZnSPh]^+$ complexes

The results of these experiments were all plotted in Excel and confirmed to be pseudo-first order. The logarithmic plots of the intensity of the zinc complex ^{1}H NMR resonance versus time for five different concentrations of CH_3I are shown on the left of Figure 22. After the natural log of the integration peaks over time were plotted, k_{obs} for each set of experiments was obtained from the slope of each plot. The data was plotted within the data analysis program IGOR to calculate error. After the error was calculated for each set of kinetics, the average of all three sets was calculated for each concentration of methyl iodide. The five averaged k_{obs} were then plotted versus concentration of methyl iodide (M), and a trendline plotted for each complex (Figure 22 Right). The slope of each

trendline provided the second-order rate constant "k" for each zinc complex. The uncertainty value was calculated using the LINEST function in Excel.

Table 3. Kinetic results of $[(TPA)ZnSPh]^+$ and $[(BA\text{-}TPA)ZnSPh]^+$ compared to $[(TPA)ZnSH]^+$ (a previous complex) with errors calculated from IGOR and the LINEST function in EXCEL

Complex	*Second Order Rate Constant ($M^{-1}s^{-1}$)*
$[(TPA)ZnSH]^+$	$1.26x10^{-4} \pm 2.94x10^{-6}$
$[(TPA)ZnSPh]^+$	$1.51x10^{-3} \pm 6.00x10^{-5}$
$[(BA\text{-}TPA)ZnSPh]^+$	$6.49\ x10^{-3} \pm 5.41x10^{-4}$

Table 3 contains the second order rate constants for our complexes and their relative errors. $[(TPA)ZnSH]^+$ was included in our study since a zinc-hydrosulfide should exhibit similar reactivity to a zinc-thiolate. $[(TPA)ZnSPh]^+$ had a second order rate constant of about $1.51 \times 10^{-3}\ M^{-1}s^{-1}$, while $[(BA\text{-}TPA)ZnSPh]^+$ had a rate of about $6.49 \times 10^{-3}\ M^{-1}s^{-1}$. This results in a four-fold increase in the rate when the hydrogen bond donor is introduced into the complex. The larger rate constant for $[(BA\text{-}TPA)ZnSPh]^+$ required us to reconsider our initial mechanistic model. Based off of Lippard's results, we had expected the alkylation mechanism for our complexes to proceed through an associative mechanism (Lippard demonstrated nitrogen-rich zinc-thiolates were shown to proceed through an associative alkylation mechanism) and that $[(BA\text{-}TPA)ZnSPh]^+$ would result in the smallest rate constant (since a hydrogen bonding interaction with the sulfur atom of the thiolate would lower its nucleophilicity). [322] However, our kinetic results show that the hydrogen bonding [(BA-TPA)ZnSPh] complex has a faster rate, meaning that the secondary coordination sphere (hydrogen bonding interaction) is having an effect on the rate and mechanism.

Table 4. Kinetic results of $[(TPA)ZnSPh]^+$ and $[(BA\text{-}TPA)ZnSPh]^+$ compared to previous complexes. (*) Refers to rate constants that are pseudo-first order k_{obs}, but are included for comparison.

Complex	*Rate Constant ($M^{-1}s^{-1}$)*
TPA Complexes	
$[(TPA)ZnSPh]^+$ (No H-Bond Donor)	*$1.51x10^{-3}$*
$[(BA\text{-}TPA)ZnSPh]^+$ (H-Donor)	*$6.49x10^{-3}$*
Lippard's Complexes	
*$[Zn(SC_6H_5)_4]^{2-}$**	*$8.2x10^{-5}(s^{-1})$*
*$[Zn(SC_6H_5)_2(MeIm)_2]^{2-}$**	*$5.0x10^{-8}(s^{-1})$*
Vahrenkamp's Complexes	
$[TpPh,R'](S_3Zn\text{-}SPh)$	*$1.1x10^{-1}$*
$[TpPh,R'](N_3(t\text{-}bu)Zn\text{-}SPh)$	*$1.0x10^{-5}$*
Cran's Complexes	
*[(L1S)ZnSPh]**	*$1.14x10^{-3}(s^{-1})$*
*[(L1O)ZnSPh]**	*$4.6x10^{-5}(s^{-1})$*
Riordan's Complexes	
[Ph(pztBu)BttBu]ZnSPh	*$2.1x10^{-4}$*
$[Ph(pz^{tBu})Bt^{tBu}]Zn(SC_6H_{4o}\text{-}NHC(O)Bu^t)$	*$6.2x10^{-6}$*

The rate constants of our complexes compared to previous complexes are shown in Table 4. The trend that Lippard and previous research groups observed was that complexes with sulfur-rich primary coordination spheres had larger rate constants.[32,37,39] This trend can be confirmed from the values in Table 4, as the sulfur-rich complexes have larger rate constants compared to their nitrogen/oxygen-rich counterparts. The explanation for the rate increase in complexes in sulfur-rich environments is attributed to

a dissociative versus an associative mechanism (the two different mechanisms are shown in Figure 3).

From the trend observed in table 4, we would expect to observe a rate decrease upon introduction of a hydrogen bond donor, while also expecting the mechanism to proceed through an associative mechanism. However, our kinetics results show the opposite. Although both our complexes contain a nitrogen-rich primary coordination spheres, the observation that the $[(BA\text{-}TPA)ZnSPh]^+$ complex is faster than $[(TPA)ZnSPh]^+$ suggests that $[(BA\text{-}TPA)ZnSPh]^+$ is proceeding through a thiolate dissociative process. This is in contrast to the associative mechanism predicted by Lippard and others prior results with nitrogen-rich environments. The fluxional behavior of $[(BA\text{-}TPA)ZnSPh]^+$ in the NMR as well as the kinetic results support the thiolate dissociative mechanism claim. The effect of the hydrogen bonding interaction in $[(BA\text{-}TPA)ZnSPh]^+$ appears to be enough to make the thiophenolate dissociate, and therefore react more quickly with electrophiles. The importance of this result is that the secondary coordination sphere is also an important factor that may influence thiolate dissociation.

As expected, our results contrast with the findings by Riordan *et. al.*[41] Riordan's group had compared complexes with and without hydrogen bond donors, and their results showed that hydrogen bonding interactions slow the rate of thiolate alkylation. They believed this to be in agreement with Verdine's theory, where hydrogen bonding lowered the nucleophicity of a thiolate (based on Ada RP's crystal structure) and the rate constants. Our complexes contradict this theory, as $[(BA\text{-}TPA)ZnSPh]^+$ has a higher rate constant than the non-hydrogen bonding complex. This leads to the question of why are these results contradictory.

A proposed theory for the difference in rate constants is based on the placement of the hydrogen bond donor. As previously mentioned in the introduction, while Riordan's complex had the hydrogen donor attached to the thiolate, our complex contains the donor within the supporting ligand BA-TPA scaffolding. As such, in our complex we believe the hydrogen bonding interaction aids in the dissociation of the thiophenolate, but once it has dissociated the hydrogen bonding/thiophenolate interaction is believed to be lost. This is not the case for Riordan's complex, as the hydrogen bonding interaction remains even after the thiolate has dissociated (as seen in Figure 23). This will make the sulfur less nucleophilic, similar to how a protic solvent can quench nucleophicity. Based on this information, we believe the placement of the hydrogen bond donor to be the reason for the difference in kinetic rates between the two studies.

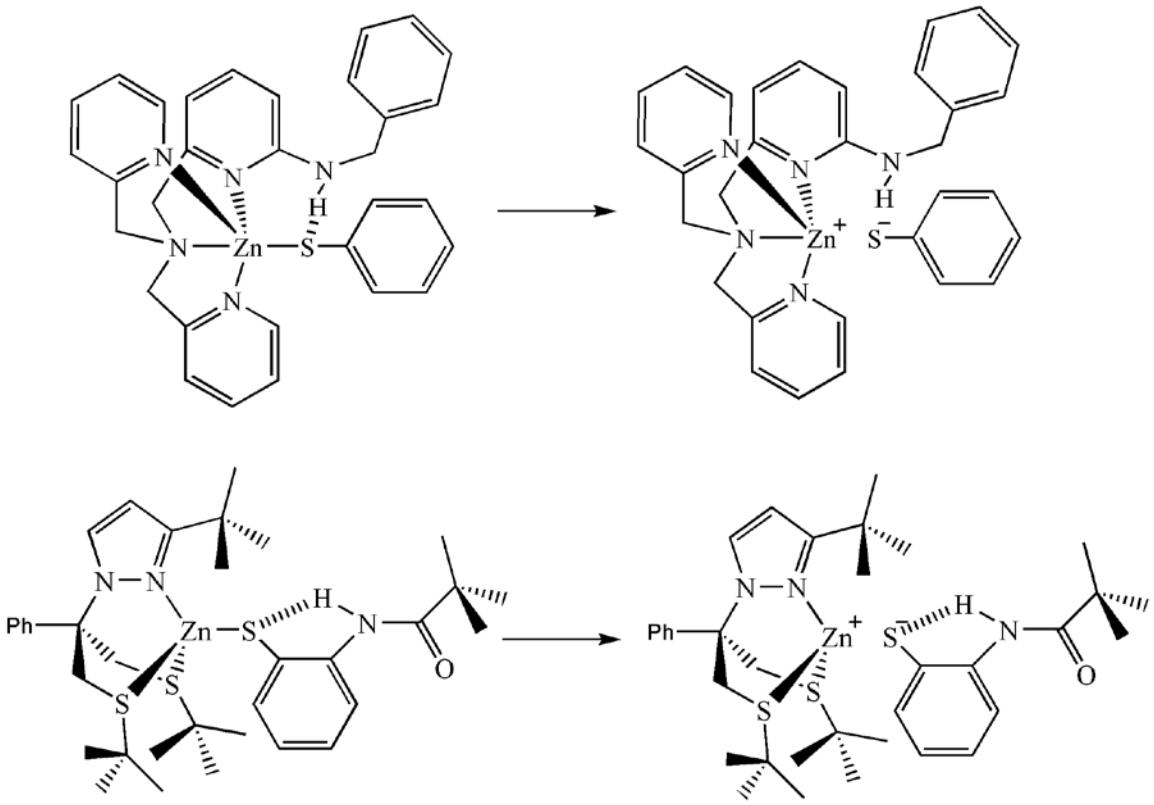

Figure 23. Comparison of hydrogen bonding effects in $[(BA\text{-}TPA)ZnSPh]^+$ (top) and Riordan's Complex (bottom)

Trapping Experiment

An additional experiment that was performed was a trapping experiment, which involved mixing our zinc-thiolate complexes with N-ethylmaleimide (NEM). NEM is an alkene-containing molecule that is highly reactive towards thiols and thiolates. NEM is a Michael acceptor and undergoes a Michael addition reaction (see Figure 24) with nucleophiles. The Michael reaction involves a nucleophile attacking the β carbon of an α,β-unsaturated carbonyl compound to form an enol, which then tautomerizes to give a ketone as the Michael addition product.[47]

The trapping experiment is similar to the thiolate alkylation kinetic experiments described earlier, except NEM is used as the electrophile instead of methyl iodide. The experiment is designed to trap dissociated thiolate by reacting with NEM to form the Michael addition product shown in Figure 18. A zinc-bound thiolate is expected to be inert or extremely slow to react with NEM since it should be less nucleophilic and more sterically hindered compared to a free thiolate. What this experiment should confirm is that the thiolate in $[(BA\text{-}TPA)ZnSPh]^+$ is rapidly dissociating to form free thiophenolate unlike $[(TPA)ZnSPh]^+$, which we believe, based off of the characterization and kinetics data, remains as a zinc-bound thiolate complex at room temperature. As such, $[(BA\text{-}TPA)ZnSPh]^+$ should react with NEM to form the Michael addition product, while $[(TPA)ZnSPh]^+$ will be unreactive.

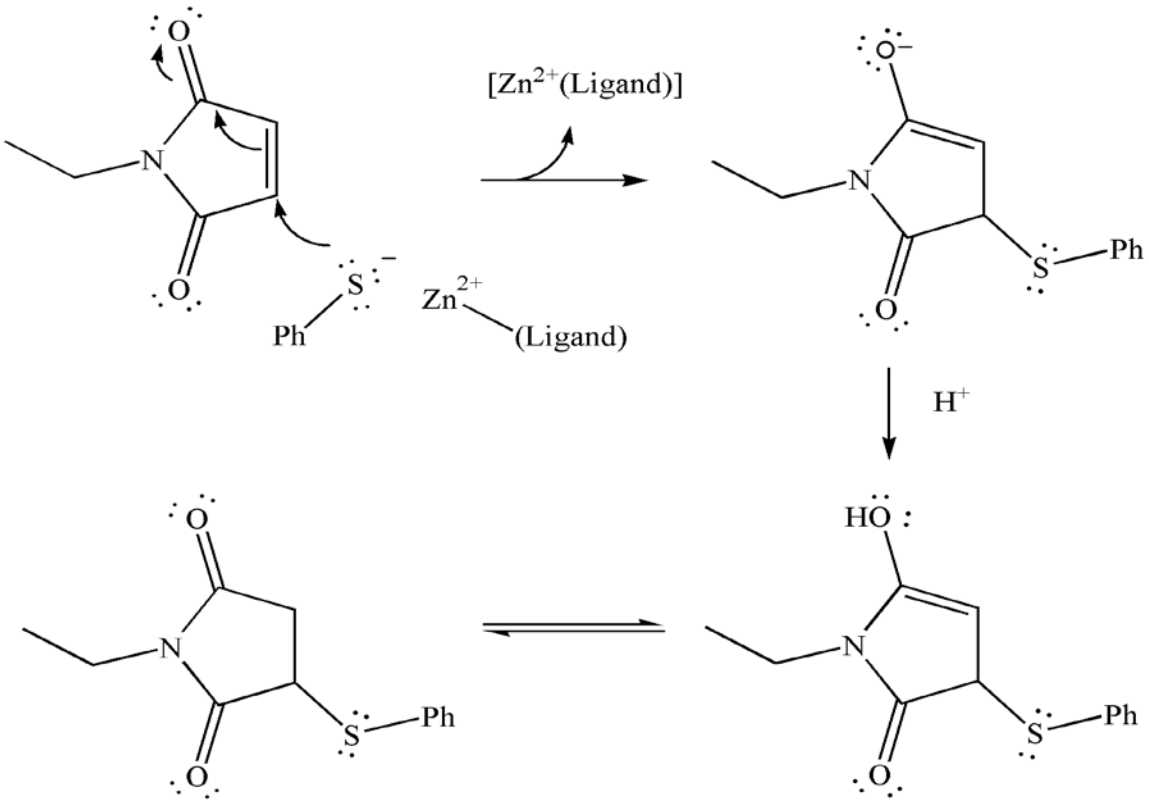

Figure 24. General Mechanism of the Trapping Experiment with N-ethylmaleimide (NEM)

The NMR trapping reactions were done in a similar manner to the alkylation kinetics and involved following the reactions by NMR at room temperature. Both [(BA-TPA)ZnSPh]$^+$ and [(TPA)ZnSPh]$^+$were placed in separate NMR tubes that contained 1,4-di-*tert*-butylbenzene ((added as an internal standard in a 1:1 zinc-thiolate:internal standard ratio) and CD_3CN (0.75 mL). After taking an initial background scan, 1 equivalent of NEM was added to each tube. The reaction was followed for 11 days by ^{1}H NMR. Similar to the alkylation kinetics, a series of peaks were followed (described below) to quantify the extent of reaction over time and to ensure formation of the Michael addition product (1-ethyl-3-(phenylthio)pyrrolidine-2,5-dione).

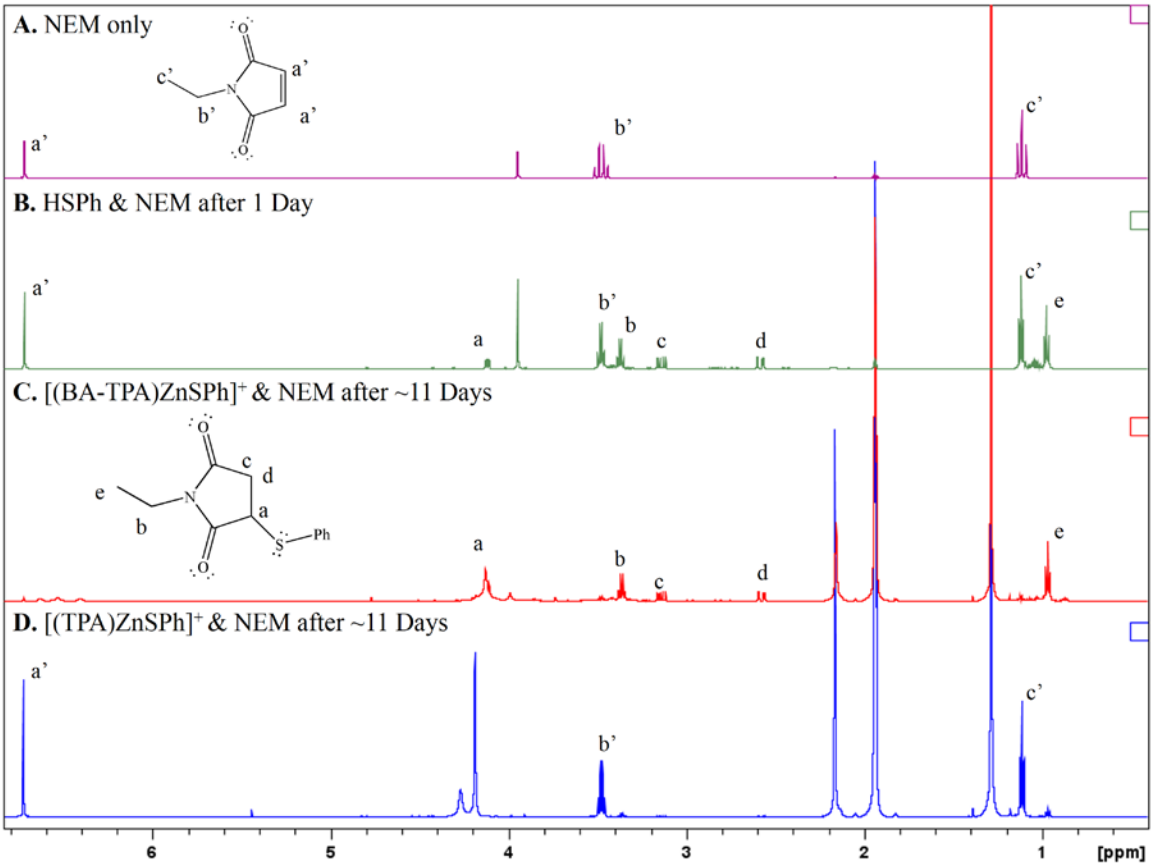

Figure 25. ^{1}H NMR Results of Trapping Experiment. The peaks of the NEM trapping product have been labeled (The aromatic Ph peaks are not shown).

The results of the reaction between NEM and our zinc-thiolate compounds are shown in Figure 25. The $[(TPA)ZnSPh]^{+}$ complex (Figure 25 D) showed almost no reaction with NEM after 11 days (only 13 % conversion to 1-ethyl-3-(phenylthio)pyrrolidine-2,5-dione). With $[(BA\text{-}TPA)ZnSPh]^{+}$, complete conversion of NEM to 1-ethyl-3-(phenylthio)pyrrolidine-2,5-dione (the Michael addition product) is observed after 11 days. The formation of 1-ethyl-3-(phenylthio)pyrrolidine-2,5-dione from the reaction of NEM and $[(BA\text{-}TPA)ZnSPh]^{+}$ is consistent with the NMR shown in Figure 25 C. The peaks for 1-ethyl-3-(phenylthio)pyrrolidine-2,5-dione are labeled in the spectrum. The peaks at 0.98 and 3.37 ppm (labeled “b” and “e” in Figure 25) grow in over time, and represent the ethyl chain of the product. In addition, the three

diastereotopic protons (doublet of doublets labeled a, c and d in Figure 25) are observed as a result of the chiral center formed in the product. The growth of these peaks are observed over time, and coincide with the same peaks for 1-ethyl-3-(phenylthio)pyrrolidine-2,5-dione that is formed upon reaction of NEM with HSPh (Figure 25 B).

The significance of the reactivity of $[(BA\text{-}TPA)ZnSPh]^+$ and $[(TPA)ZnSPh]^+$ with NEM is consistent with the characterization and alkylation kinetics results. While $[(TPA)ZnSPh]^+$ had little to no reactivity with NEM, $[(BA\text{-}TPA)ZnSPh]^+$ reacted with NEM, albeit not as fast as thiophenol. What this means is that the thiolate within $[(BA\text{-}TPA)ZnSPh]^+$ is more available to react compared to $[(TPA)ZnSPh]^+$. Therefore, the fact that $[(BA\text{-}TPA)ZnSPh]^+$ reacts faster with NEM means that thiolate dissociation is occurring readily with $[(BA\text{-}TPA)ZnSPh]^+$, consistent with alkylation kinetics and characterization data.

CHAPTER FIVE: CRYSTALLOGRAPHY

Crystal Structure of Complexes

The molecular structure of $[(TPA)ZnSPh]^+$ and important bond lengths are shown in Figure 26. A summary of the X-ray crystallographic data and refinement parameters for the two complexes is provided in Table 5. While the crystallography results confirm the structure, the most important result is the determination of the Zn-S bond distance. In the $[(TPA)ZnSPh]^+$ complex, the atomic distance of the Zn-S bond was 2.3215 Å. This distance gives insight into the complex and how reactive it is with electrophiles. For comparison, the bond distances of the Zn-S bonds for reacting Ada RP was 2.18-2.29 Å for the non-reacting cysteines, and 2.47 Å for Cys38 (the reacting cysteine).[25] Although not as long as the Zn-S of Cys38, the Zn-S of $[(TPA)ZnSPh]^+$ is longer than the non-reactive cysteines. It is possible that the $[(TPA)ZnSPh]^+$ complex is near the threshold of thiolate dissociation, but the bond length isn't long enough for it to readily occur at room temperature.

Multiple efforts were made to grow suitable crystals of the $[(BA\text{-}TPA)ZnSPh]^+$ complex for X-ray diffraction, but no attempts were successful. A possible explanation as to the reason for this difficulty may be due to thiolate dissociation occurring readily at room temperature (this is the temperature that the attempted crystallizations were conducted). The crystals may not be able to form due to two species competing against each other, which can make growing crystals difficult.

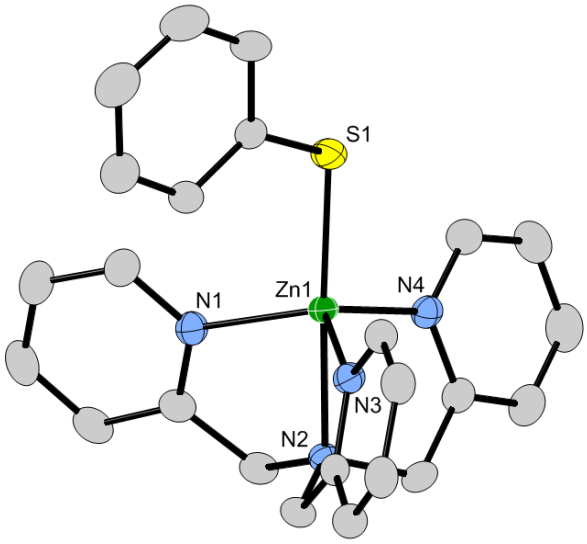

Figure 26. Representation of the cationic portion of the X-ray structure of $[(TPA)ZnSPh]^+$ with thermal ellipsoids drawn at 50% probability level and hydrogen atoms omitted for clarity. Important bond lengths (Å): Zn1-S1 2.3214(5), Zn1-N1 2.1104(16), Zn1-N2 2.252715, Zn1-N3 2.0803(16), Zn1-N4 2.0943(17). Bond angles (°) N1-Zn1-S1 104.91(5), N2-Zn1-S1 176.62(4), N3-Zn1-S1 104.62(5), N4-Zn1-S1 99.32(5), N1-Zn1-N2 76.75(6), N1-Zn1-N3 116.24(6), N1-Zn1-N4 112.10(6), N2-Zn1-N3 76.99(6), N2-Zn1-N4 77.30(6), N3-Zn1-N4 116.95(6).

Table 5. Crystallopgraphic data and parameters for $[(TPA)ZnSPh]^+$

	$[(TPA)ZnSPh]^+$
Chemical Formula	*$C_{24}H_{23}ClN_4O_4SZn$*
Formula Weight (g/mol)	*564.34*
Crystal System	*orthorhombic*
Space Group	*P b c a*
a(Å)	*9.4146(3)*
b(Å)	*14.9247(4)*
c(Å)	*34.6711(10)*
α(°)	*90*
β(°)	*90*
γ(°)	*90*
Volume($Å^3$)	*4871.6(2)*
Z	*8*
Density (g/cm^3)	*1.539*
Temperature (K)	*150*
Color	*Colorless*
Crystal Size (mm)	*0.140 x 0.280 x 0.420*
Absorption Coefficient (mm^{-1})	*1.243*
Theta Range (°)	*2.35 to 27.88*
Completeness to θ (%)	*100.0%*
Reflections Collected	*41910*
Independent Reflections	*5805*
Parameters	*325*
R_1/wR_2 (all data)	*0.0367/0.0732*
Goodness-of-fit	*1.139*
Difference in peak/hole ($e/Å^{-3}$)	*.344/-.311*

The bond distance of $[(TPA)ZnSPh]^+$ in comparison to previous complexes can be found in Table 6. From the table, a correlation between the kinetics and the Zn-S bond length is observed. In Lippard's complexes, for example, the Zn-S bond of $[Zn(SC_6H_5)_4]^{2-}$ has a bond length of 2.353 Å. Their other complex, $[Zn(SC_6H_5)_2(MeIm)_2]^{2-}$, had a Zn-S bond length of 2.291 Å. [48,49] Recalling the trend seen in the kinetics, $[Zn(SC_6H_5)_4]^{2-}$ had a k_{obs} of $8.2x10^{-5}$ s^{-1}. This was much faster than the k_{obs} value for $[Zn(SC_6H_5)_2(MeIm)_2]^{2-}$ (which was $5.0x10^{-8}$ s^{-1}). The reason why this is significant is because $[Zn(SC_6H_5)_4]^{2-}$ has a longer Zn-S bond length and is faster than

$[Zn(SC_6H_5)_2(MeIm)_2]^{2-}$. From there results, there seems to be a correlation between the length of the Zn-S bond and the kinetic rate.

Table 6. Bond distances of [(TPA)ZnSPh]+ compared to previous complexes. (*) Refers to approximate values

Complex	*Zn-S Bond Distance (Å)*
TPA Complexes	
$[(TPA)ZnSPh]^+$ (No H-Bond Donor)	2.321(5)
$[(BA\text{-}TPA)ZnSPh]^+$ (H-Donor)	*N/A*
Lippard's Complexes	
*$[Zn(SC_6H_5)_4]^{2-}$**	*2.353(1)*
*$[Zn(SC_6H_5)_2(MeIm)_2]^{2-}$**	*2.291(7)*
Vahrenkamp's Complexes	
[TpPh,R'](S$_3$Zn-SPh)	*2.248(2)*
[TpPh,R'](N$_3$(t-bu)Zn-SPh)	*2.232(0)*
Cran's Complexes	
*[(L1S)ZnSPh]**	*2.259**
*[(L1O)ZnSPh]**	*2.202**
Riordan's Complexes	
[Ph(pztBu)BttBu]ZnSPh	*2.260*
$[Ph(pz^{tBu})Bt^{tBu}]Zn(SC_6H_{4o}\text{-}NHC(O)Bu^t)$	*2.265*

This correlation was also seen with the [TpPh,R'] complexes that were made by different collaborators. [TpPh,R'](S$_3$Zn-SPh), the Tp complex that only contained sulfur donors in the primary coordination sphere, had a Zn-S bond length of 2.248 Å.[50] While crystal data for [TpPh,R'](NS$_2$Zn-SPh) is unavailable, the [TpPh,R'](N$_2$SZn-SPh) complex showed a Zn-S bond length of 2.235 Å (not shown in table). [51,52] After all three

sulfur groups were replaced with nitrogen donors, the atomic radii became 2.232 Å.[33] This trend of the Zn-S bond length becoming shorter follows the same trend Lippard observed. This trend can also be seen in both Carrano's and Riordan's complexes ([(L1S)ZnSPh], [Ph(pz^{tBu})Bt^{tBu}]Zn(SC_6H_{4o}-NHC(O)Bu^t) and [Ph(pz^{tBu})Bt^{tBu}]ZnSPh; see Figures 8 and 10 for structures of complexes), but the decrease in the bond length is not as large as the changes Lippard or the Tp collaborators witnessed.

This trend in bond length is important because a similar trend was also seen in the kinetic results with our complexes. When the primary coordination sphere of the zinc ion is more sulfur-rich, there is two observations. The first is that the rate constant of all of the sulfur-rich complexes is higher than complexes containing nitrogen or oxygen donors. The second observation is that the bond length of the Zn-S bond of the sulfur-rich complexes is longer than any of the other complexes. The increased rate of reaction with increased Zn-S distance is to be expected, due to the correlation of bond length and thiolate dissociation (longer Zn-S distance then increased thiolate dissociation, which translates to an increase in thiolate reactivity). The greater the distance of the sulfur atom from the zinc ion, the higher the likelihood of thiolate dissociation occurring since a longer bond results in a more ionic bond, which should be more prone to dissociation. Along with that, dissociation causes the sulfur of the thiolate to be more nucleophilic, which in a more reactive zinc-thiolate complexes. As such, the bond distance and the kinetic rate are correlated.

The reason why this is pertinent to our results is because our complexes show a similar trend, but with a major difference. While the previous complexes showed changes when the primary coordination sphere was altered, our complexes had differences only in

the secondary coordination sphere. When the hydrogen bonding group was added to the complex, the complex became more reactive (as evident by the kinetics data). This is important, because although we do not have the crystal structure of $[(BA\text{-}TPA)ZnSPh]^+$, the kinetic results gives insight into what the bond length could potentially be. Since the Zn-S bond length of $[(TPA)ZnSPh]^+$ could be sitting on the threshold of thiolate dissociation, the hydrogen bonding interaction present in the $[(BA\text{-}TPA)ZnSPh]^+$ complex may be the push that results in a lengthening of the Zn-S bond such that thiolate dissociation occurs at room temperature, which results in the increased reactivity.

CONCLUSION

From previous research, the theory was that the primary coordination sphere was the main variable in determining if a complex would dissociate. Based on the results of these experiments, it becomes clear that the primary coordination sphere is not the only factor that increases the occurrence of dissociation. In the [(TPA)ZnSPh]ClO_4 and [(BA-TPA)ZnSPh]ClO_4 complexes synthesized, we noticed a trend when a single hydrogen bond donor was added to the ligand scaffolding. [(BA-TPA)ZnSPh]ClO_4 had broad thiophenol peaks (with no discernable splitting) in the ^{1}H NMR and ^{13}C NMR, and these broad peaks sharpened when the temperature was cooled during the variable temperature experiment. This also had an effect on the speed of the kinetic experiments, with [(BA-TPA)ZnSPh]ClO_4 having a rate constant at least four times greater than [(TPA)ZnSPh]ClO_4. From these results, the evidence points to [(BA-TPA)ZnSPh]ClO_4 showing signs of dissociation, even though it is not contained within a sulfur-rich environment. Although a suitable [(BA-TPA)ZnSPh]ClO_4 crystal was not grown for X-ray crystallography, the fact the growth wasn't occurring adds to the likelihood that [(BA-TPA)ZnSPh]ClO_4 is dissociating. In conclusion, we were able to show that the secondary coordination sphere has a role in promoting dissociation within a metal-containing complex. It is our belief that from this research, future research will expand our theory, and that more accurate, improved synthetic analogues will be the result.

REFERENCES

1. Shiver, D., & Atknis, P. (1999). *Chapter 19, Bioinorganic chemistry, Inorganic Chemistry.* Oxford University Press.

2 . Lindskog, S. (1997). Structure and Mechanism of Carbonic Anhydrase. Pharmacology and Therapeutics, 74, 1-20.

3 . Maton, A., Hopkins, J., & Mclaughlin, C. W. (1993). *Human Biology and Health.* Englewood Cliffs, New Jersey, USA: Prentice Hall.

4 . Klug, A. (2010). The discovery of zinc fingers and their applications in gene regulation and genome manipulation. *Annual Review of Biochemistry, 79*, 213-31.

5 . White, R., Margolis, P., & Trias, J. (2003). Targeting Metalloenzymes: A Strategy That Works. *Current Opinion in Pharmacology, 3*, 502-507.

6 . Pastorekova, S., Zatovicova, M., & Pastorek, J. (2008). Cancer-Associated Carbonic Anhydrases and Their Inhibition. *Current Pharmaceutical Design, 14*, 685-698.

7 . Boone, C., Gill, S., Habibzadegan, A., & McKenna, R. (2013). Carbonic Anhydrase: An efficient enzyme with Possible Global Implications. *International Journal of Chemical Engineering*, 1-6.

8 . Eadie, J. S., Conrad, M., Toorchen, D., & Topal, M. D. (1984). Mechanism of Mutagenesis by 06-Methylguanine. *Nature*, 201-203.

9 . Benjamin, F., Li, L., Reese, C. B., & Swann, P. (1987). Synthesis and Characterization of Oligodeoxynucleotides Containing 4-O-Methylthymine. *Biochemistry, 26*, 1086-1093.

10 . Noonan, E. M., Shah, D., Yaffe, M. B., Lauffenburger, D. A., & Samson, L. D. (2012). O6-Methylguanine DNA lesions induce an intra-S-phase arrest from

which cells exit into apoptosis governed by early and late multi-pathway signaling network activation. *Integrative Biology (Camb), 4*(10), 1237-1255.

11 . Mishina, Y., Duguid, E. M., & He, C. (2006). Direct Reversal of DNA Alkylation Damage. *Chemical Reviews, 106*(2), 215-232.

12 . McCarthy, T. V., & Lindahl, T. (1985). Methyl Phosphotriesters in Alkylated DNA are repaired by the Ada regulatory protein of E. Coli. *Nucleic Acids Research, 13*(8), 2683-2698.

13 . Sedgwick, B. (2004). Repairing DNA-Methylation Damage. *Nature Reviews: Molecular Cell Biology, 5*, 148-157.

14 . Vaughan, P., Sedgwick, B., Hall, J., Gannon, J., & Lindahl, T. (1991). Environmental mutagens that induce the adaptive response to alkylating agents in Escherichia coli. *Carcinogenesis, 12*(2), 263-268.

15 . Lijinsky, W. (1999). N-Nitroso compounds in the diet. *Mutation Research, 443*, 129-138.

16 . Hecht, S. (2008). Carcinogenesis Progress and Challenges in Selected Areas of Tobacco. *Chemical Research in Toxicology, 21*, 160-171.

17 . Landini, P., & Volkert, M. (2000). Regulatory Responses of the Adaptive Response to Alkylation Damage: a Simple Regulon with Complex Regulatory Features. *Journal of Bacteriology*, 6543-6549.

18 . Lindahl, T., & Sedgwick, B. (1988). Regulation and Expression of the Adaptive Response to Alkylating Agents. *Annual Review of Biochemistry, 57*, 133-157.

19 . Volkert, M. R. (1988). Adaptive Response of Escherichia coli to Alkylation Damage. *Environmental and Molecular Mutagenesis, 11*, 241-255.

20 . Li, D., Delaney, J., Page, C., Chen, A., Wong, C., Drennan, C., & Essigmann, J. (2010). Repair of DNA Alkylation Damage by the Escherichia coli Adaptive Response Protein AlkB as Studied by ESI-TOFMass Spectrometry. *Journal of Nucleic Acids*, 1-9.

21 . Landini, P., Hajec, L., & Volkert, M. (1994). Structure and Transcriptional Regulation of the Escherichia Coli Adaptive Response Gene AidB. *Journal of Bacteriology*, 6583-6589.

22 . Rohankhedkar, M. S., Mulrooney, S. B., Wedemeyer, W. J., & Hausinger, R. P. (2006). The AidB Component of the Escherichia coli Adaptive Response to Alkylating Agents Is a Flavin-Containing, DNA-Binding Protein. *Journal of Bacteriology, 188*(1), 223-230.

23 . Lin, Y., Dotsch, V., Wintner, T., Peariso, K., Myers, L., Penner-Hahn, J., . . . Wagner, G. (2001). Refined Structure of the DNA Methyl Phosphotriester Repair Domain of E. Coli Ada. *Biochemistry*(40), 4261-4271. PDB ID: 1EYF

24 . Moore, M., Gulbis, J., Dodson, E., Demple, B., & Moody, P. (1994). Crystal structure of a suicidal DNA repair protein: the Ada 06-methylguanine-DNA methyltransferase from E.coli. *The EMBO Journal, 13*(7), 1495-1501. PDB ID: 1SFE

25 . He, C., Hus, J.-C., Sun, L. J., Zhou, P., Norman, D., Dotsh, V., . . . Verdine, G. (2005). A Methylation-Dependent Electrostatic Switch Controls DNA Repair and Transcriptional Activation by E. coli Ada. *Molecular Cell, 20*, 117-129.

26 . Sakumi, K., Igarashi, K., Sekiguchi, M., & Ishihama, A. (1993). The Ada Protein Is a Class I Transcription Factor of Escherichia coli. *Journal of Bacteriology*, 2455-2457.

27 . Myers, L., Wagner, G., & Verdine, G. (1995). Direct Activation of the Methyl Chemosensor Protein N-Ada by CH3I. *Journal of the American Chemical Society, 117*, 10749-10750.

28 . Myers, L., Jackow, F., & Verdine, G. (1995). Metal Dependence of Transcriptional Switching in Escherichia Coli Ada. *The Journal of Biological Chemistry, 270*(12), 6664-6670.

29 . Daniels, D., Mol, C., Arvai, A., Kanugula, S., Pegg, A., & Tainer, J. (2000). Active and Alkylated Human AGT Structures: a Novel Zinc Site, Inhibitor and Extrahelical Base Binding. *The EMBO Journal, 19*(7), 1719-1730.

30 . Hazra, T., Roy, R., Biswas, T., Grabowski, D., Pegg, A., & Mitra, S. (1997). Specific Recognition of O6-Methylguanine in DNA by Active Site Mutants of Human O6-Methylguanine-DNA Methyltransferase. *Biochemistry, 36*, 5769-5776.

31 . Teo, A., Oh, H. K., Ali, R., & Li, B. (2004). The Modified Human DNA Repair Enzyme O6-Methylguanine-DNA Methyltransferase Is a Negative Regulator of Estrogen Receptor-Mediated Transcription upon Alkylation DNA Damage. *Molecular and Cellular Biology*, 7105-7114.

32 . Wilker, J., & Lippard, S. (1997). Alkyl Transfer to Metal Thiolates: Kinetics, Active Species Identification, and Relevance to the DNA Methyl Phosphotriester Repair Center of Escherichia coli Ada. *Inorganic Chemistry, 36*, 969-978.

33 . Brand, U., Rombach, M., Seebacher, J., & Vahrenkamp, H. (2001). Functional Modeling of Cobalamine-Independent Methionine Synthase with Pyrazolylborate-Zinc-Thiolate Complexes. *Inorganic Chemistry, 40*, 6151-6157.

34 . Brand, U., Rombach, M., & Vahrenkamp, H. (1998). Methylation of Zinc Bound Thiolates; a Model for Cobalamine Independent Methionine Synthase. *Chemistry Communications*, 2717-2718.

35 . Ibers, J., & Holm, R. (1980). Modeling Coordination Sites in Metallobiomolecules. *Science, New Series, 209*(4453), 223-235.

36 . Parkin, G. (2004). Synthetic Analogues Relevant to the Structure and Function of Zinc Enzymes. *Chemical Reviews, 104*(2), 699-768.

37 . Rombach, M., Seebacher, J., Ji, M., Zhang, G., He, G., Ibrahim, M., . . . Vahrenkamp, H. (2006). Thiolate Alkylation in Tripod Zinc Complexes: A Comparative Kinetic Study. *Inorganic Chemistry, 45*, 4571-4575.

38 . Rombach, M., Maurer, C., Weis, K., Keller, E., & Vahrenkamp, H. (1999). Evidence for a Trajectory of Hydrolytic Reactions Brought about by [L3Zn-OH] Species. *Chemistry: A European Journal, 5*(3), 1013-1027.

39 . Warthen, C., Hammes, B., Carrano, C., & Crans, D. (2001). Methylation of Neutral Psuedotetrahedral Zinc Thiolate Complexes: Model Reactions for Alkyl Group Transfer to Sulfur by Zinc-Containing Enzymes. *Journal of Biological Inorganic Chemistry, 6*, 82-90.

40 . He, C., Wei, H., & Verdine, G. (2003). Converting the Sacrificial DNA Repair Protein N-Ada into a Catalytic Phosphotriester Repair Enzyme. *Journal of the American Chemical Society, 125*, 1450-1451.

41 . Chiou, S.-J., Riordan, C., & Rheingold, A. (2003). Synthetic Modeling of Zinc Thiolates: Quantitative Assessment of Hydrogen Bonding in Modulating Sulfur Alkylations Rates. *PNAS, 100*(7), 3695-3700.

42 . Beni, A., Dei, A., Laschi, S., Rizzitano, M., & Sorace, L. (2008). Tuning the Charge Distribution and Photoswitchable Properties of Cobalt–Dioxolene Complexes by Using Molecular Techniques. *Chemistry: A European Journal, 14*, 1804-1813.

43 . Kim, S., Saracini, C., Siegler, M., Drichko, N., & Karlin, K. (2012). Coordination Chemistry and Reactivity of Cupric-hydroperoxide Species Featuring a Proximal H-bonding Substituent. *Inorganic Chemistry, 51*(23), 12603-12605.

44 . Spiropulos, N., Standley, E., Shaw, I., Ingalls, B., Diebels, B., Krawczyk, S., . . . Brown, E. (2012). Synthesis of Zinc and Cadmium O-alkyl Thiocarbonate and Dithiocarbonate Complexes and a Cationic Zinc Hydrosulfide Complex. *Inorganic Chimica Acta, 386*, 83-92.

45. Raycroft, M., Maxwell, C., Robyn, O., Andrea, A., Neverov, A., & Brown, S. (2012). *Trifunctional Metal Ion-Catalyzed Solvolysis: Cu(II)-Promoted Methanolysis of N,N-bis(2-picolyl) Benzamides Involves Unusual Lewis Acid Activation of Substrate, Delivery of Coordinated Nucleophile, Powerful Assistance of the Leaving Group Departure.* Inorganic Chemistry.

46 . *Technique Primer: Pseudo-First Order Kinetics- Determination of a Rate Law*. (n.d.). Retrieved from http://sitesmedia.s3.amazonaws.com/chem/files/2012/08/Pseudo_first_order_ Primer.pdf

47 . Nelson, D. L., & Cox, M. (2000). *Lehninger, Principles of Biochemistry* (Vol. III). New York: Worth Publishing.

48 . Swenson, D., Baenziger, N., & Coucouvanis, D. (1978). Tetrahedral mercaptide complexes. Crystal and molecular structures of [(C6H5)4P]2M(SC6H5)4 complexes (M = cadmium(II), zinc(II), nickel(II), cobalt(II), and manganese(II)). *Journal of the American Chemical Society*, 1932-1934.

49 . Wilker, J., & Lippard, S. (1997). Alkyl Transfer to Metal Thiolates: Kinetics, Active Species Identification, and Relevance to the DNA Methyl Phosphotriester Repair Center of Escherichia coli Ada. *Inorganic Chemistry, 36*, 969-978.

50 . Ibrahim, M., Seebacher, J., Steinfeld, G., & Vahrenkamp, H. (2005). Tris(thioimidazolyl)borate-Zinc-Thiolate Complexes for the Modeling of Biological Thiolate Alkylations. *Inorganic Chemistry, 44*, 8531-8538.

51 . Ibrahim, M., He, G., Seebacher, J., Benkmil, B., & Vahrenkamp, H. (2005). Biomimetic Thiolate Alkylation with Zinc Pyrazolylbis(thioimidazolyl)borate Complexes. *European Journal of Inorganic Chemistry*, 4070-4077.

52 . Ji, M., Benkmil, B., & Vahrenkamp, H. (2005). Zinc-Thiolate Complexes of the Bis(pyrazolyl)(thioimidazolyl)hydroborate Tripods for the Modeling of Thiolate Alkylating Enzymes. *Inorganic Chemistry*(44), 3518-3523.

APPENDIX A

Spectra and Characterization of $[(TPA)Zn\text{-}SPh]^{+}$

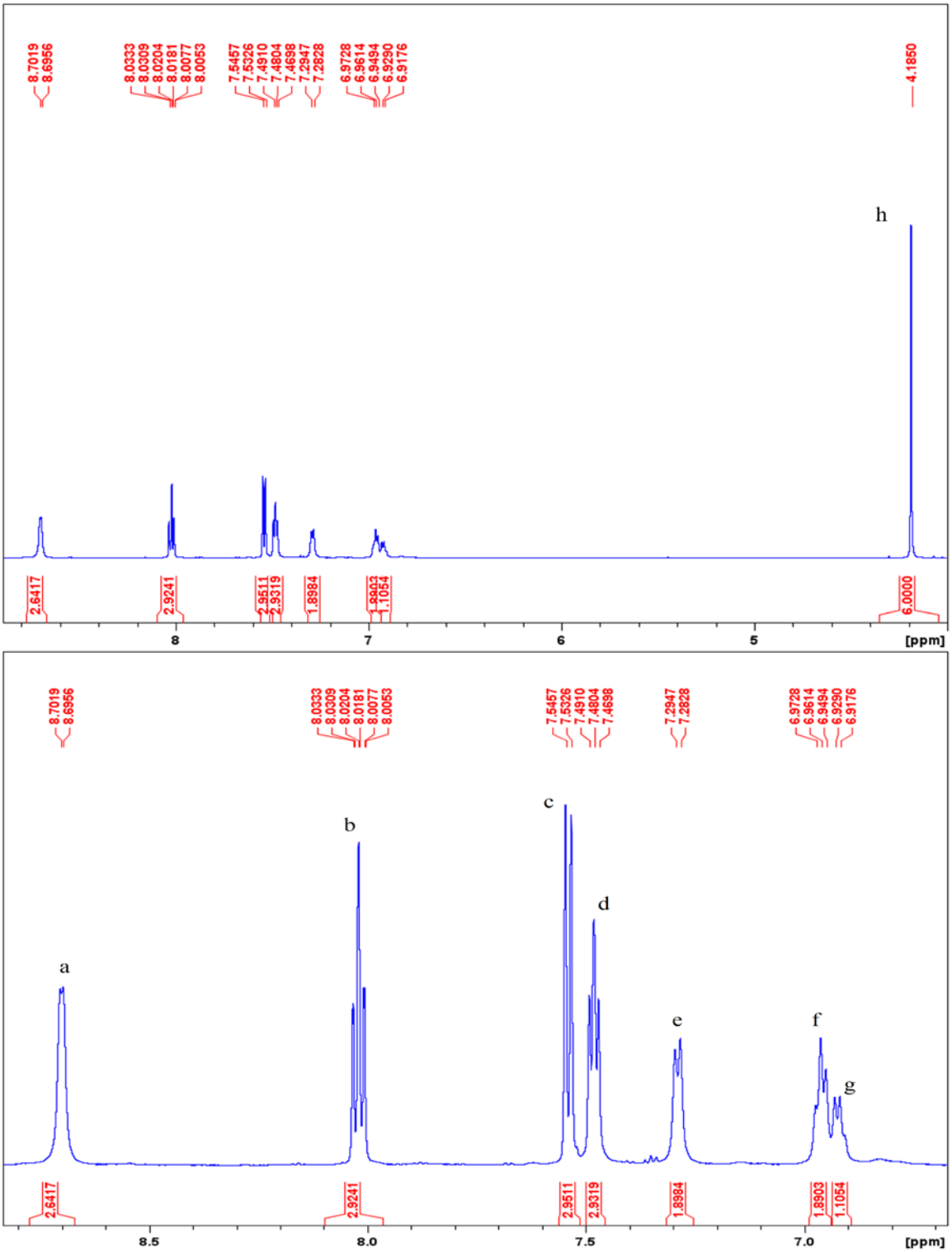

Figure A1: Full 1H NMR spectrum (Top) and Zoomed region (6.0 ppm-9.0 ppm, Bottom) of ^{1}H spectra of [(TPA)Zn-SPh]$^{+}$ (Solvent: CD_3CN)

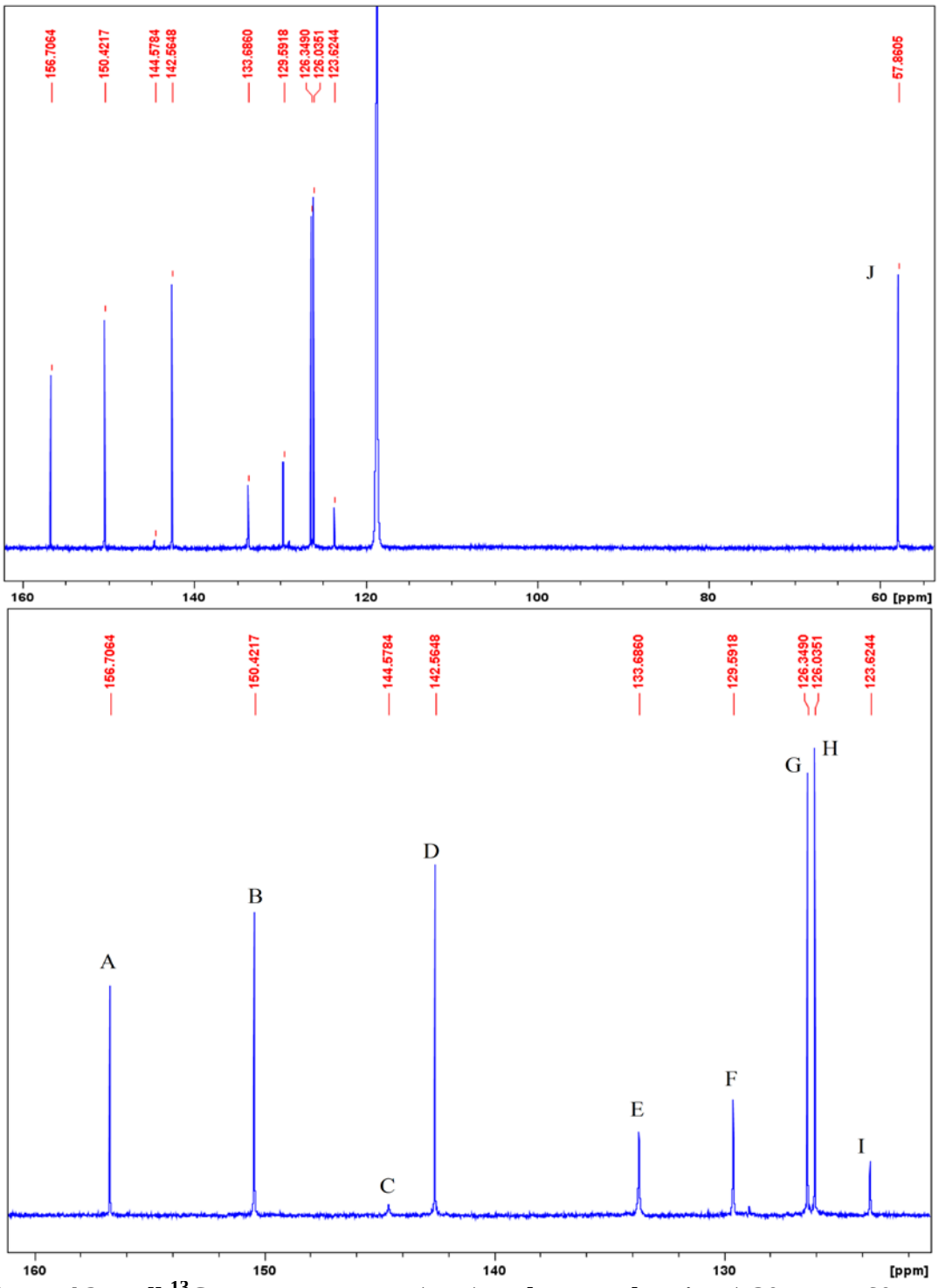

Figure A2: Full ^{13}C NMR spectrum (Top) and Zoomed region (120 ppm-160 ppm, Bottom) of ^{13}C spectra of $[(TPA)Zn\text{-}SPh]^+$ (Solvent: CD_3CN)

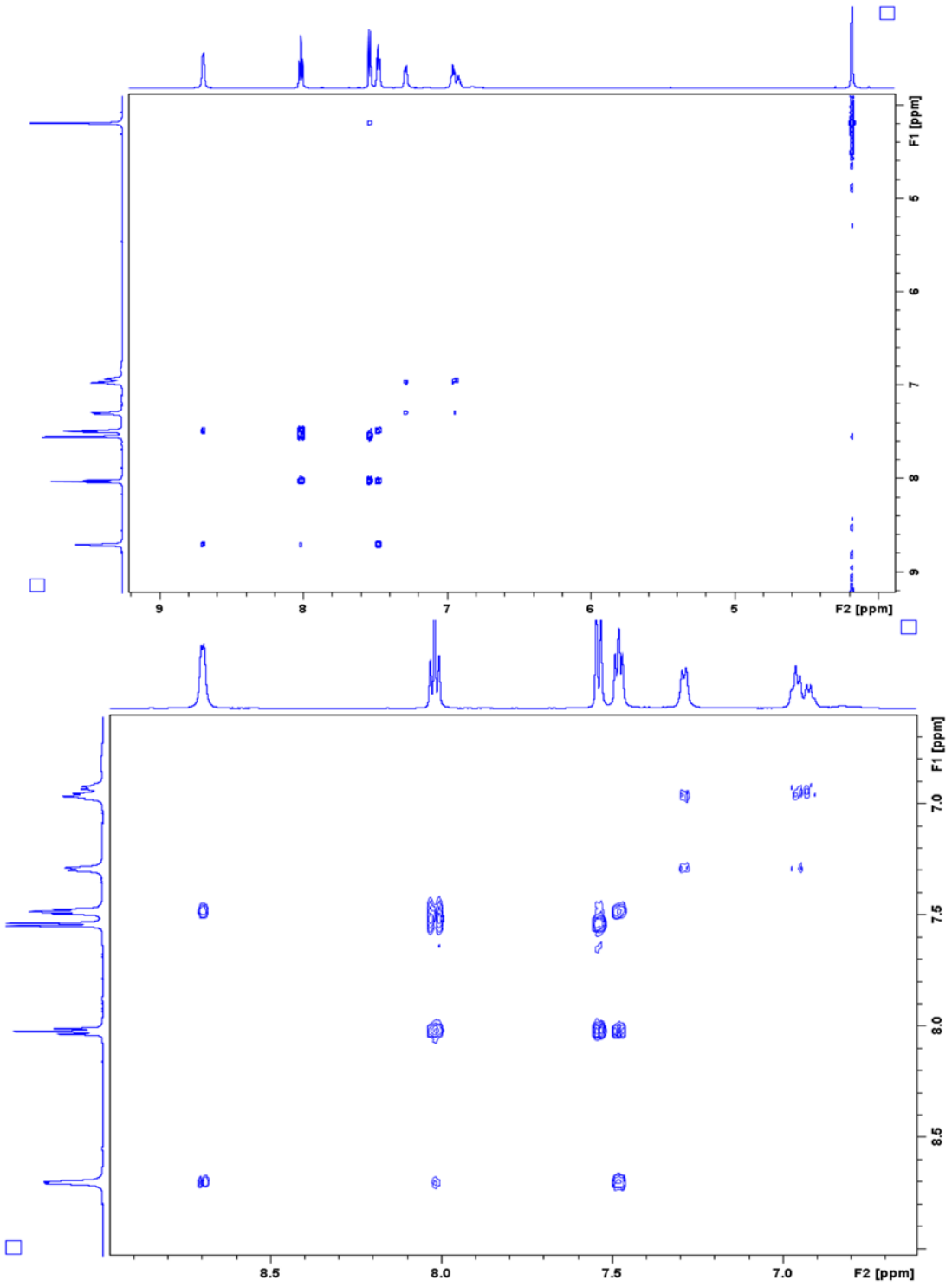

Figure A3: Full COSY spectrum (Top) and Zoomed region (6.0 ppm-9.0 ppm Bottom) of COSY of $[(TPA)Zn\text{-}SPh]^+$ (Solvent: CD_3CN)

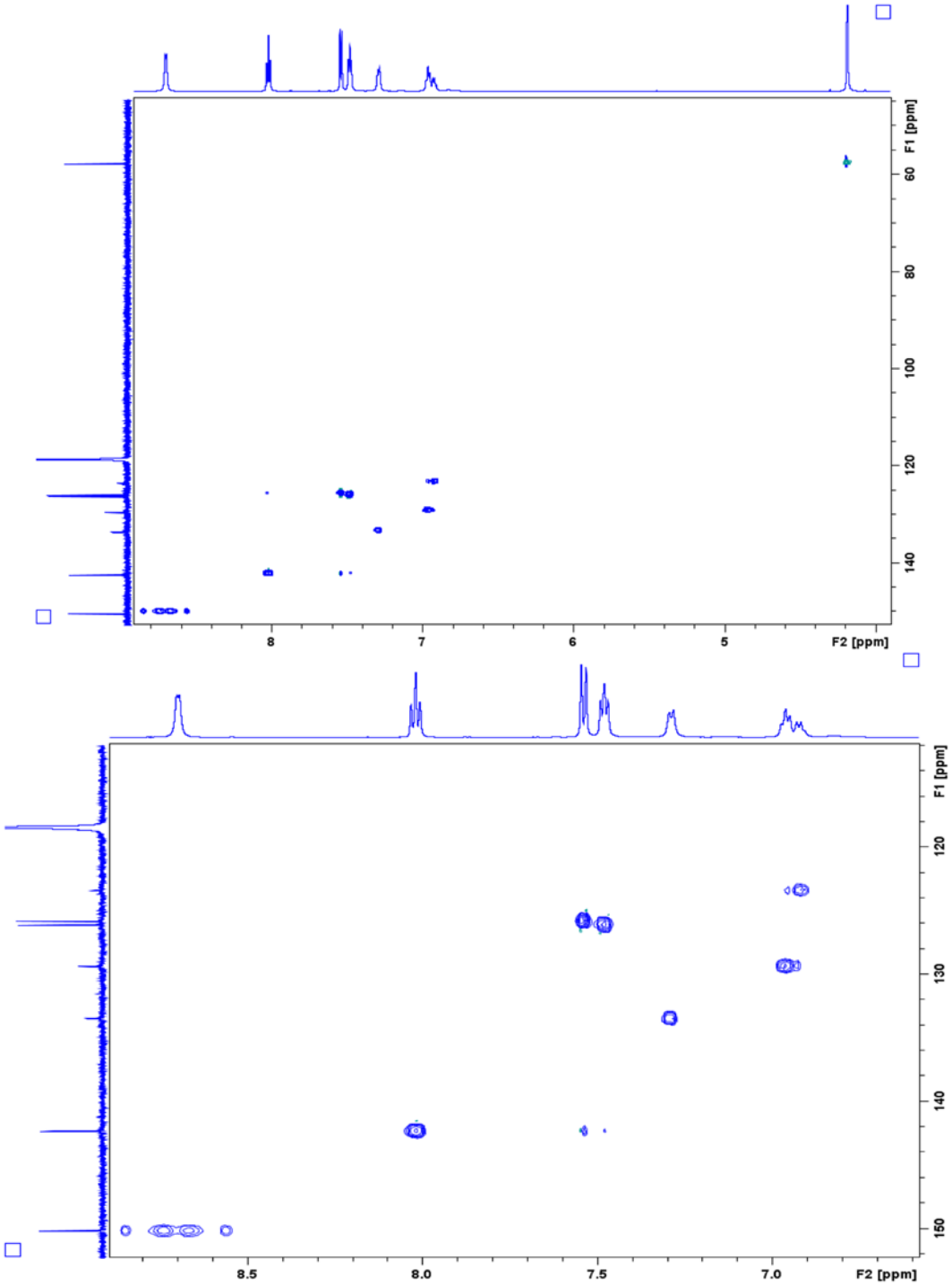

Figure A4: Full HSQC spectrum (Top) and Zoomed region (6.0 ppm-9.0 ppm, 110 ppm-150 ppm, Bottom) of HSQC of $[(TPA)Zn\text{-}SPh]^+$ (Solvent: CD_3CN)

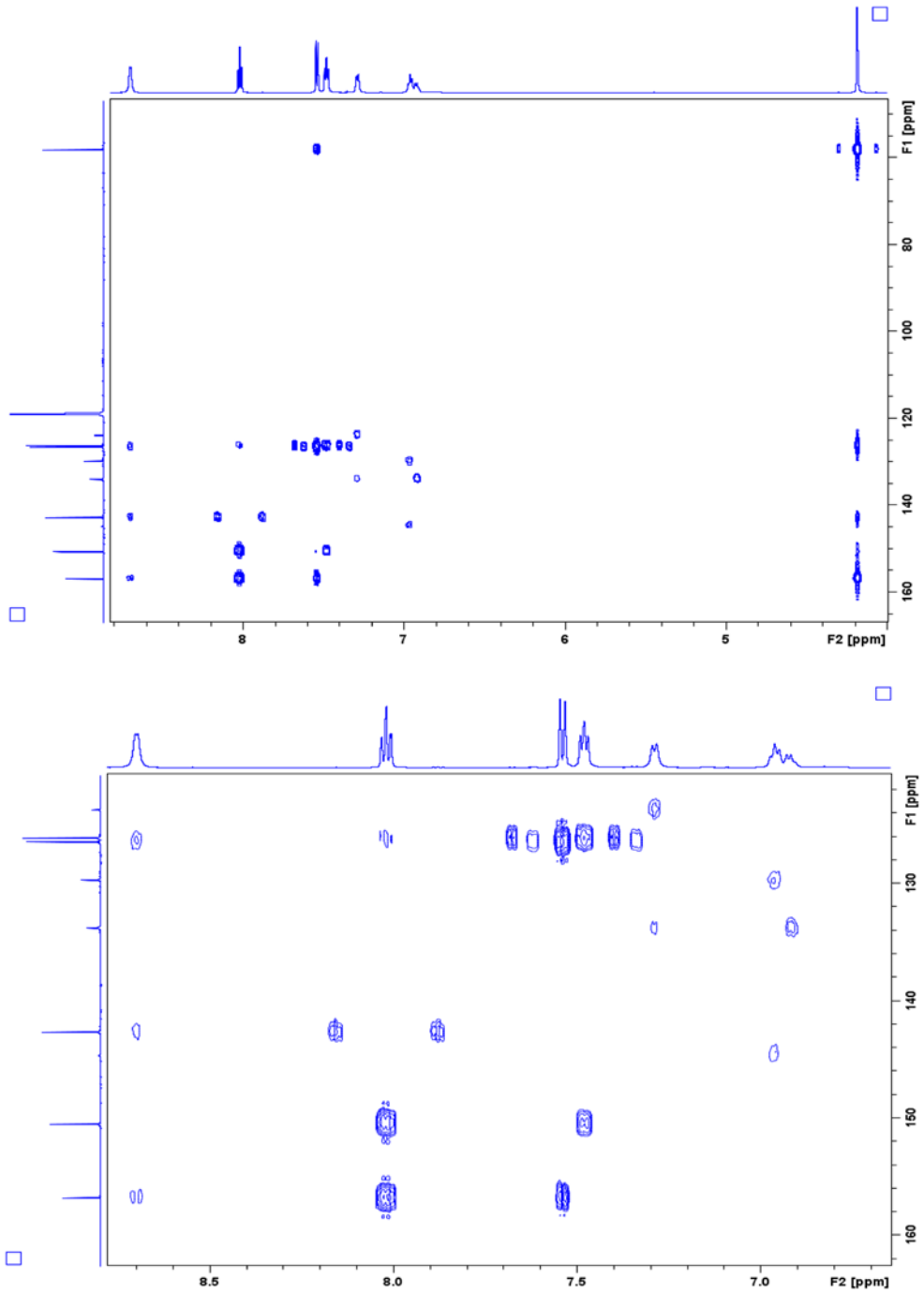

Figure A5: Full HMBC spectrum (Top) and Zoomed region (6.5 ppm-9.0 ppm, 120 ppm-162 ppm, Bottom) of HMBC of $[(TPA)Zn\text{-}SPh]^+$ (Solvent: CD_3CN)

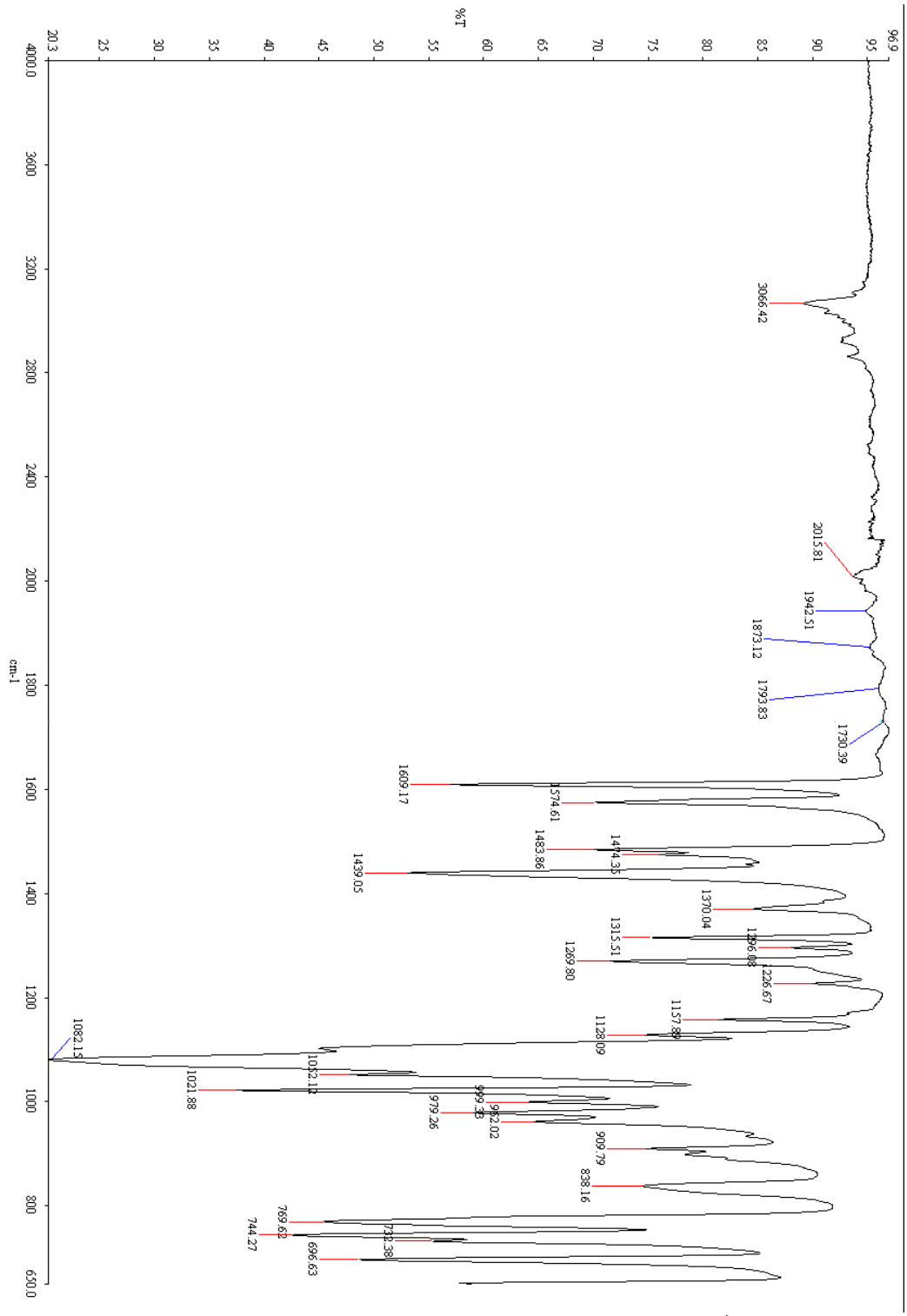

Figure A6: IR Spectrum of [(TPA)Zn-SPh]$^{+}$

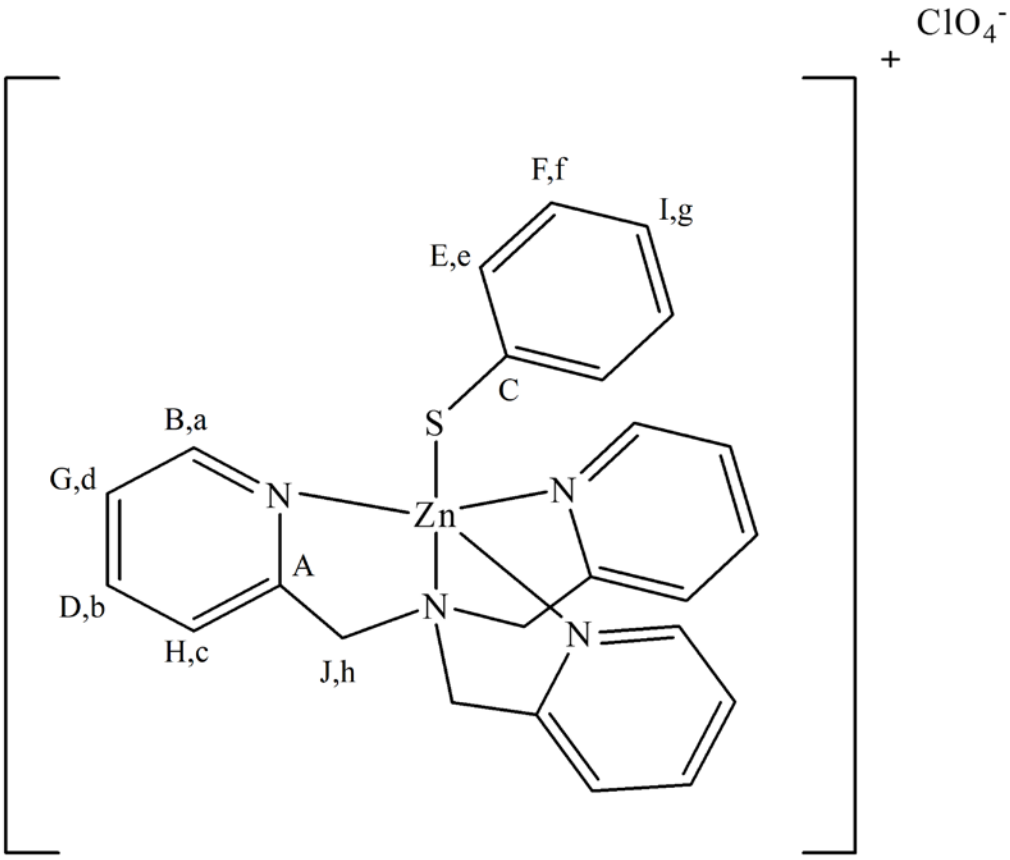

Figure A7: [(TPA)Zn-SPh]ClO_4 with peak labels corresponding to which carbon peak (capital letters) and proton peak (lower-case letters) they match to in the spectra

APPENDIX B

Spectra and Characterization of $[(BA\text{-}TPA)Zn\text{-}SPh]^{+}$

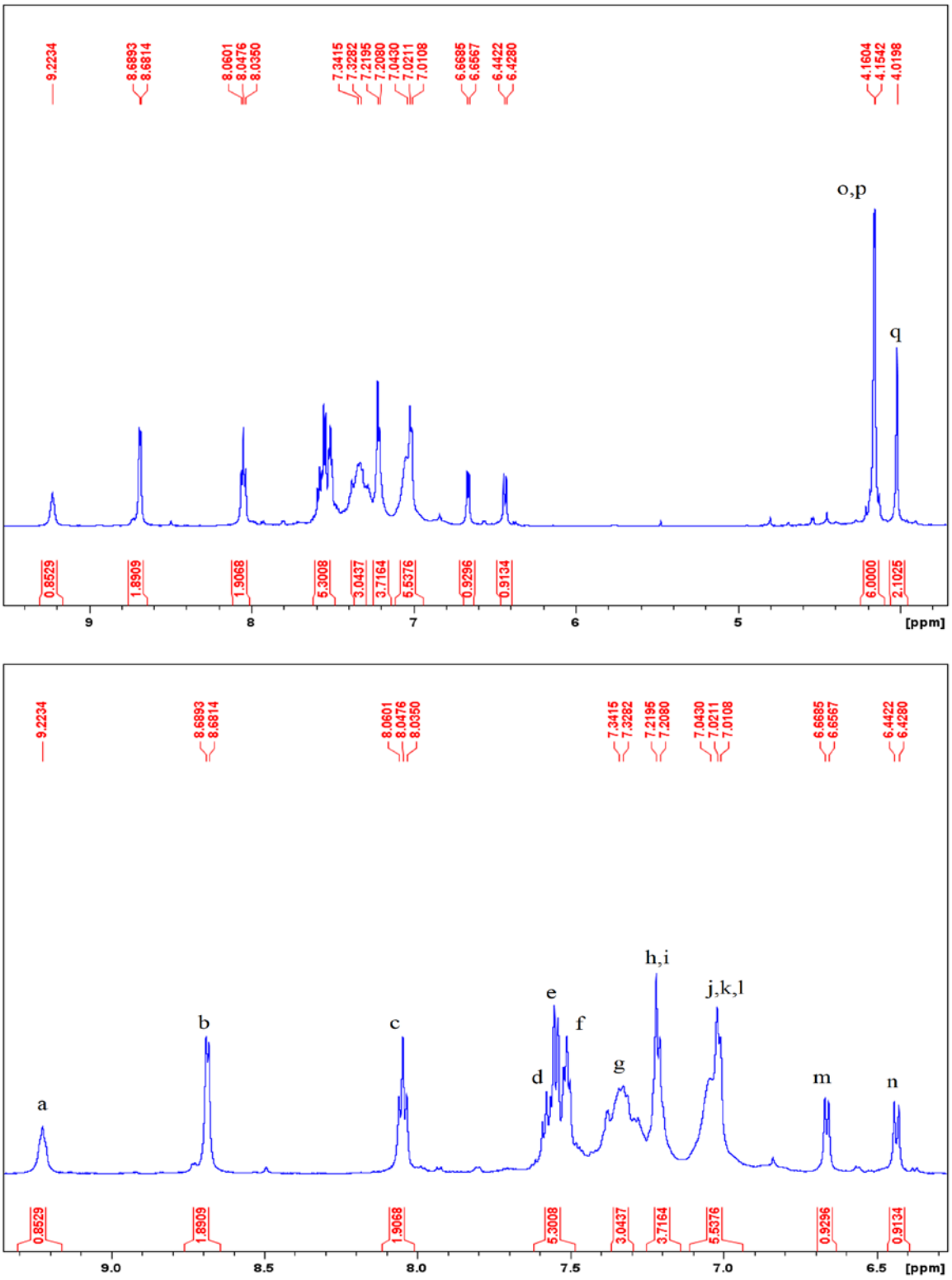

Figure B1: Full ^{1}H NMR spectrum (Top) and Zoomed region (6.2 ppm-9.6 ppm Bottom) of ^{1}H spectra of [(BA-TPA)Zn-SPh]$^{+}$ (Solvent: CD_3CN)

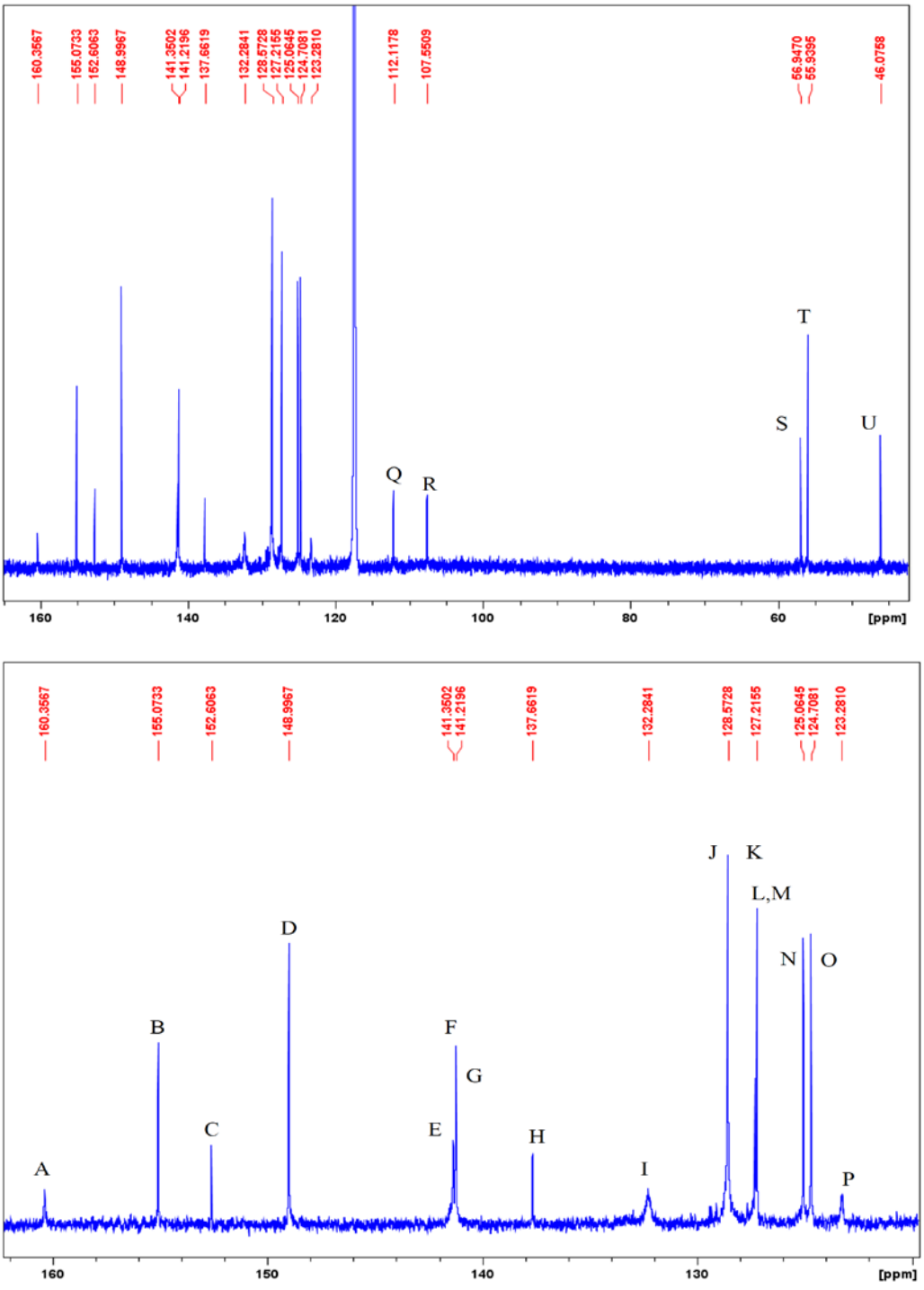

Figure B2: Full ^{13}C NMR spectrum (Top) and Zoomed region (120 ppm-162 ppm Bottom) of ^{13}C spectra of $[(BA\text{-}TPA)Zn\text{-}SPh]^+$ (Solvent: CD_3CN)

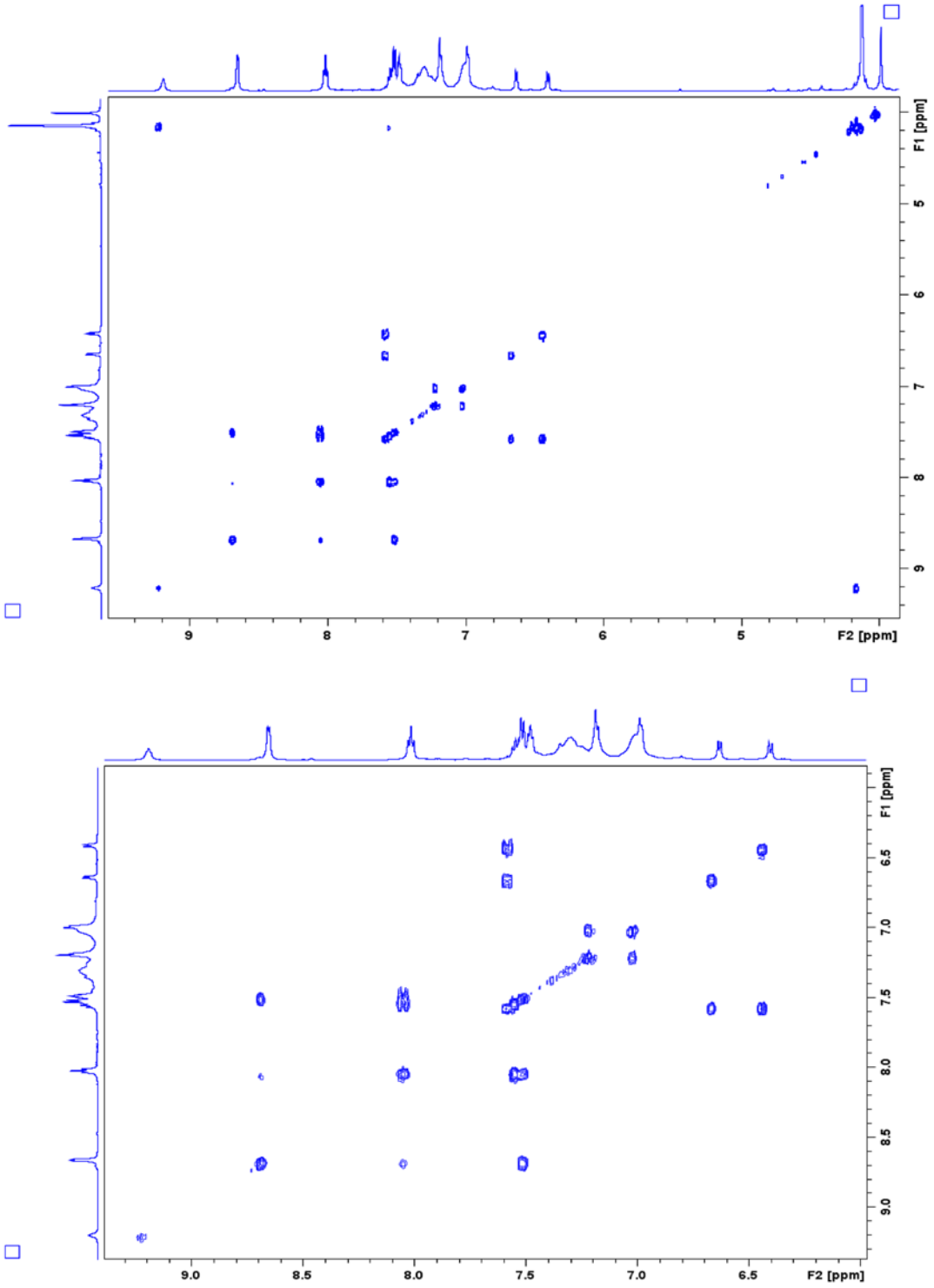

Figure B3: Full COSY spectrum (Top) and Zoomed region (6.0-9.5 ppm, Bottom) of COSY of $[(BA\text{-}TPA)Zn\text{-}SPh]^+$ (Solvent: CD_3CN)

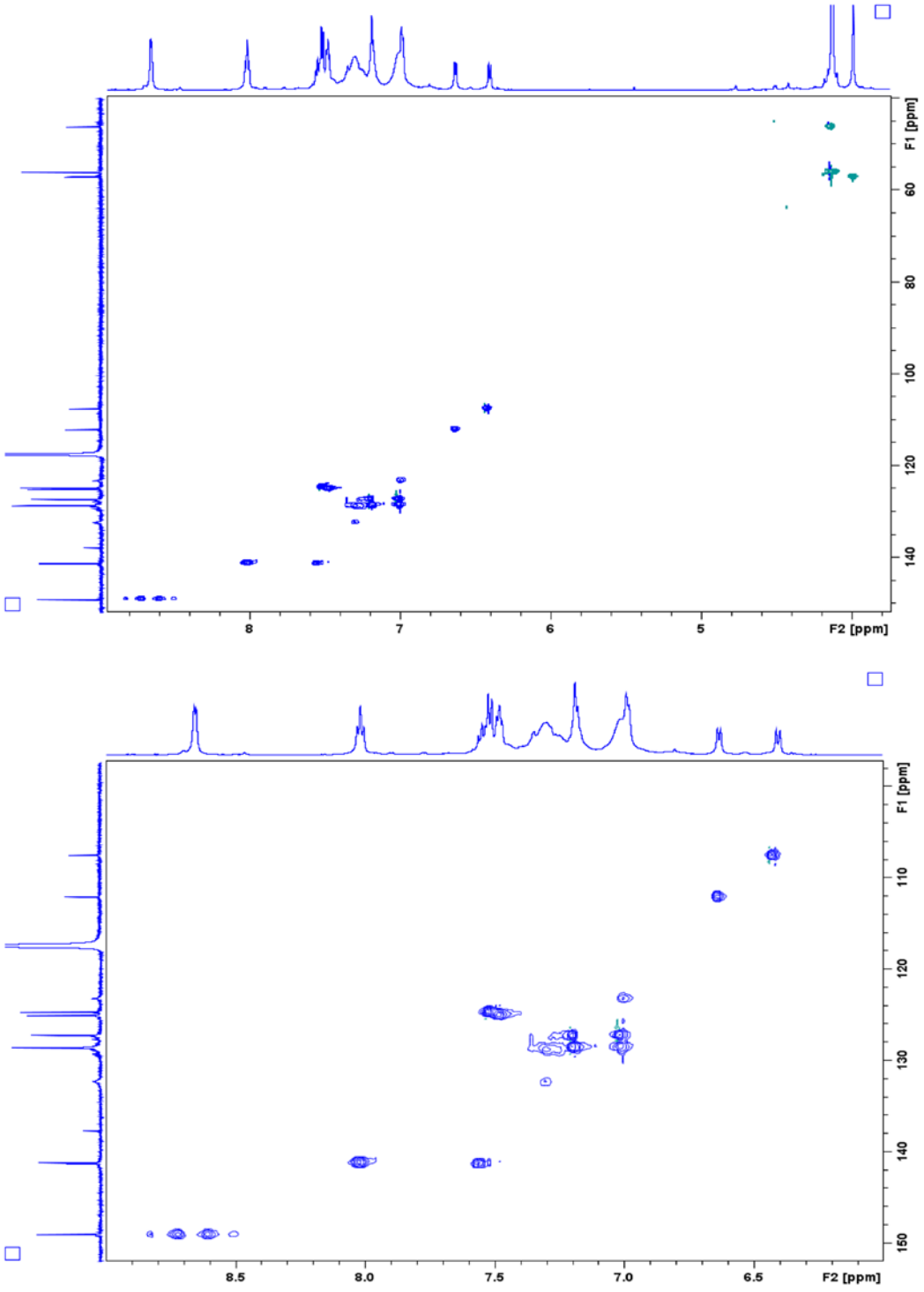

Figure B4: Full HSQC spectrum (Top) and Zoomed region (6.0-9.5 ppm, 100-150 ppm, Bottom) of HSQC of $[(BA\text{-}TPA)Zn\text{-}SPh]^+$ (Solvent: CD_3CN)

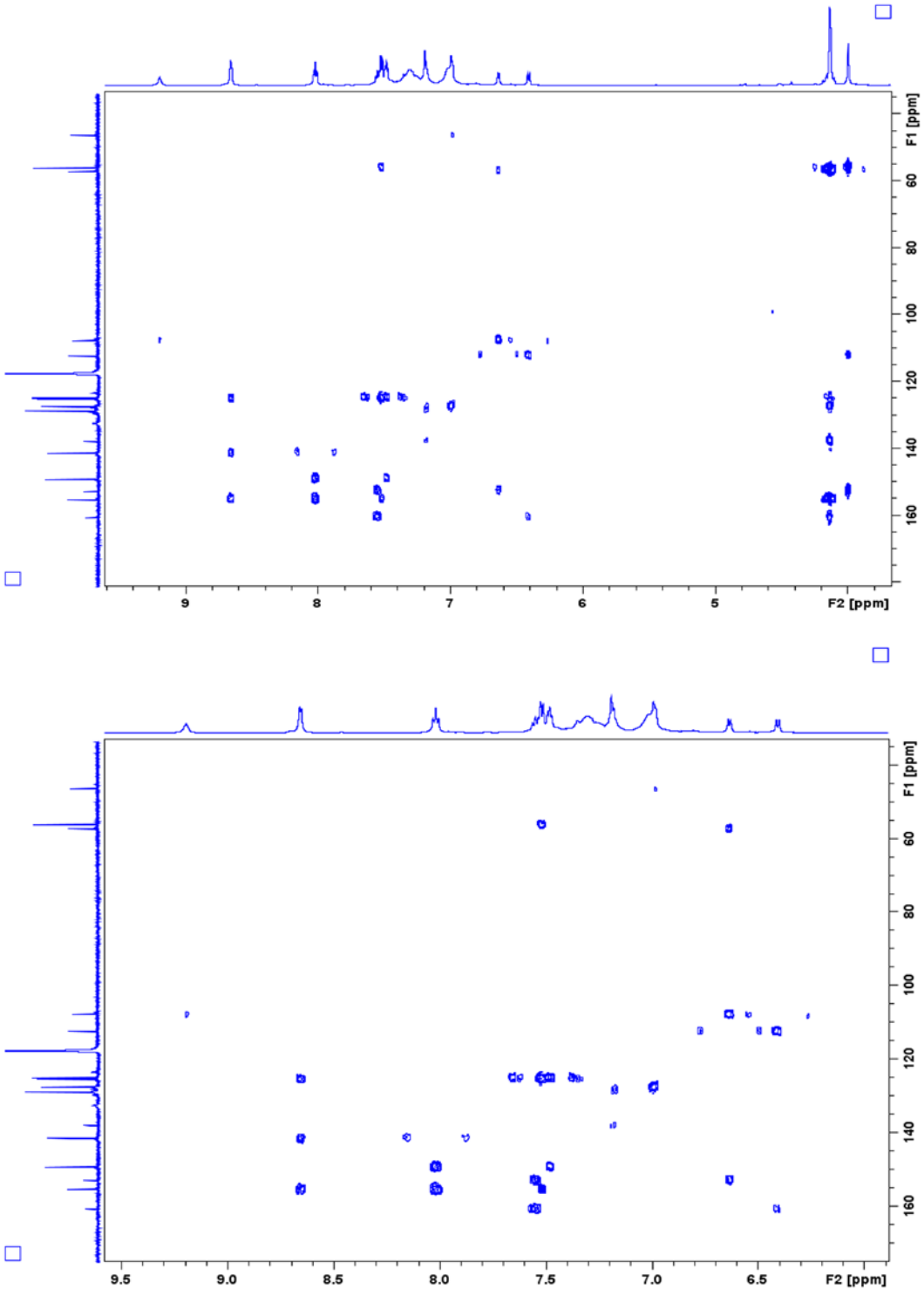

Figure B5: Full HMBC spectrum (Top) and Zoomed region (6.0 ppm-9.5 ppm, 100 ppm-170 ppm, Bottom) of HMBC of $[(BA\text{-}TPA)Zn\text{-}SPh]^+$ (Solvent: CD_3CN)

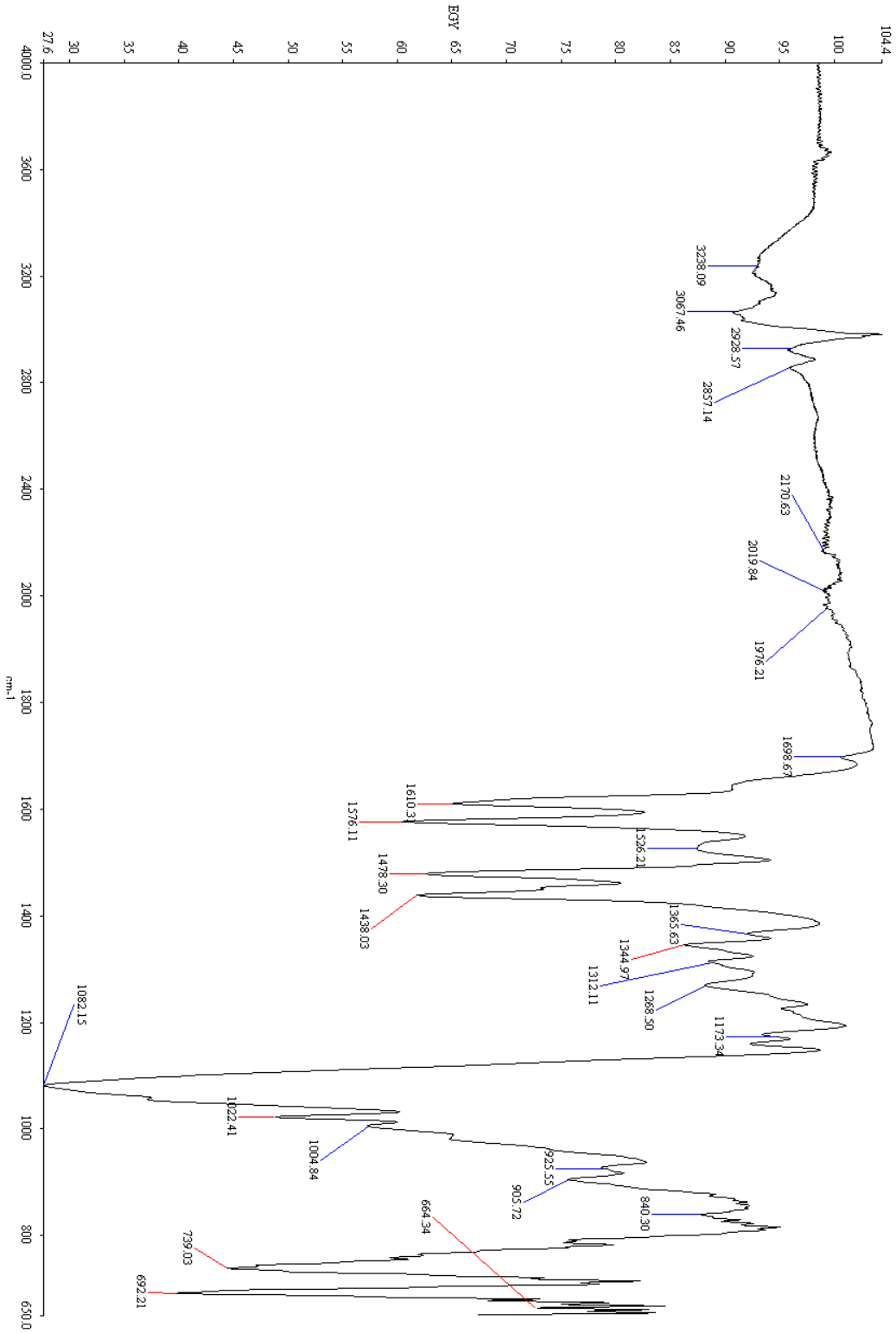

Figure B6: IR Spectrum of [(BA-TPA)Zn-SPh]$^{+}$

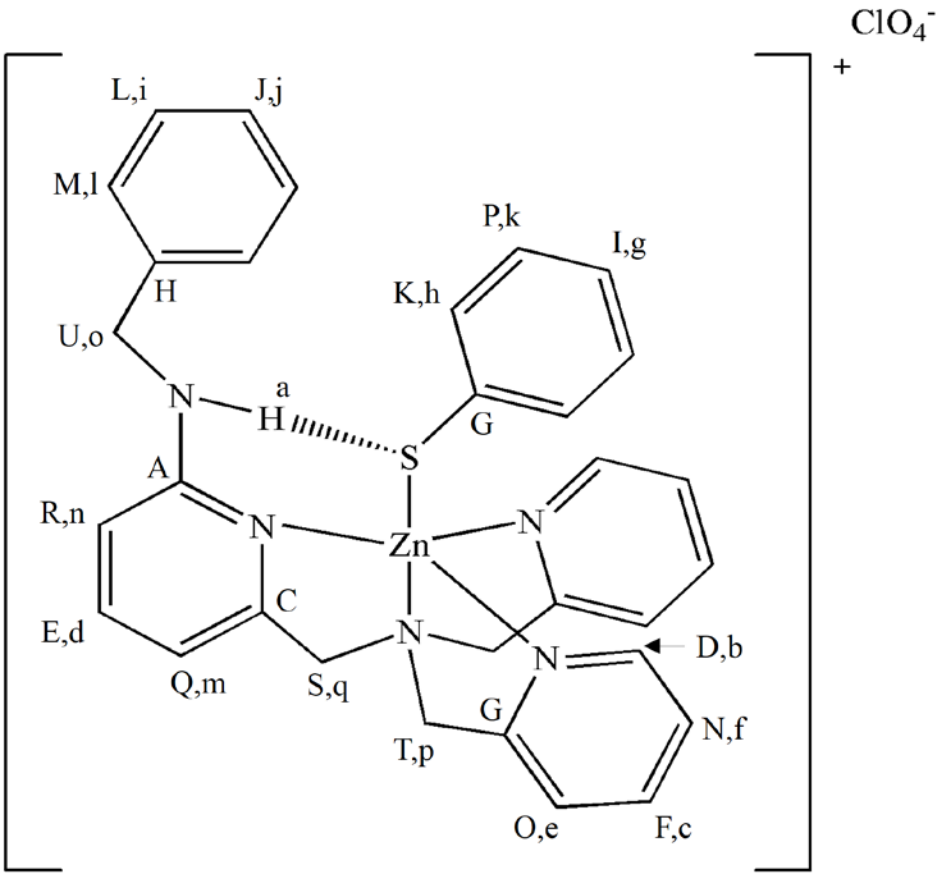

Figure B7: [(BA-TPA)Zn-SPh]ClO_4 with peak labels corresponding to which carbon peak (capital letters) and proton peak (lower-case letters) they match to in the spectra

APPNDIX C

Spectra, Characterization and Variable Temperature Results of $[(BA\text{-}TPA)Zn\text{-}SPh]^+$ at -33°C

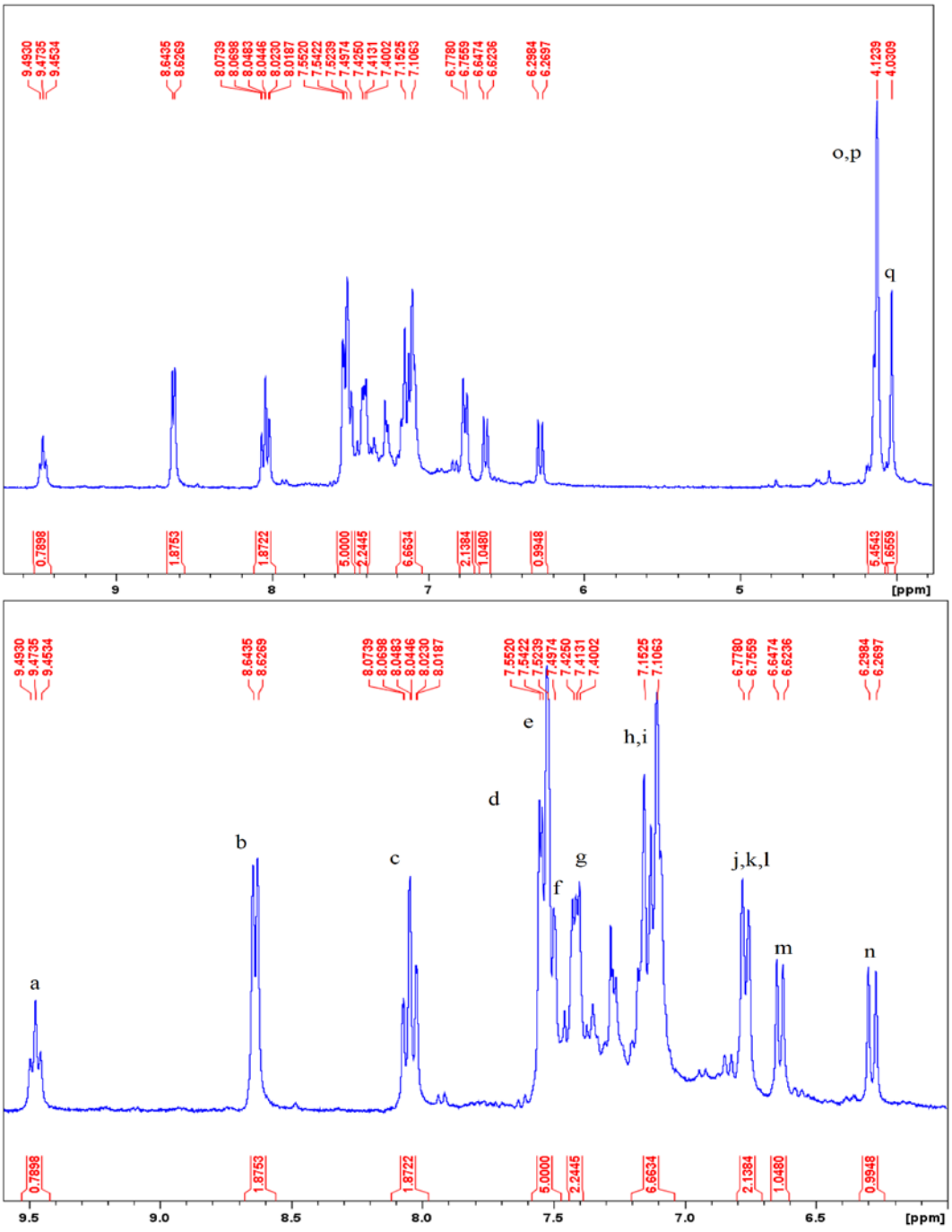

Figure C1: Full ^{1}H NMR spectrum (Top) and Zoomed region, 6.0 ppm-9.5 ppm, Bottom) of ^{1}H spectra of [(BA-TPA)Zn-SPh]$^{+}$ cooled to -33°C (Solvent: CD_3CN)

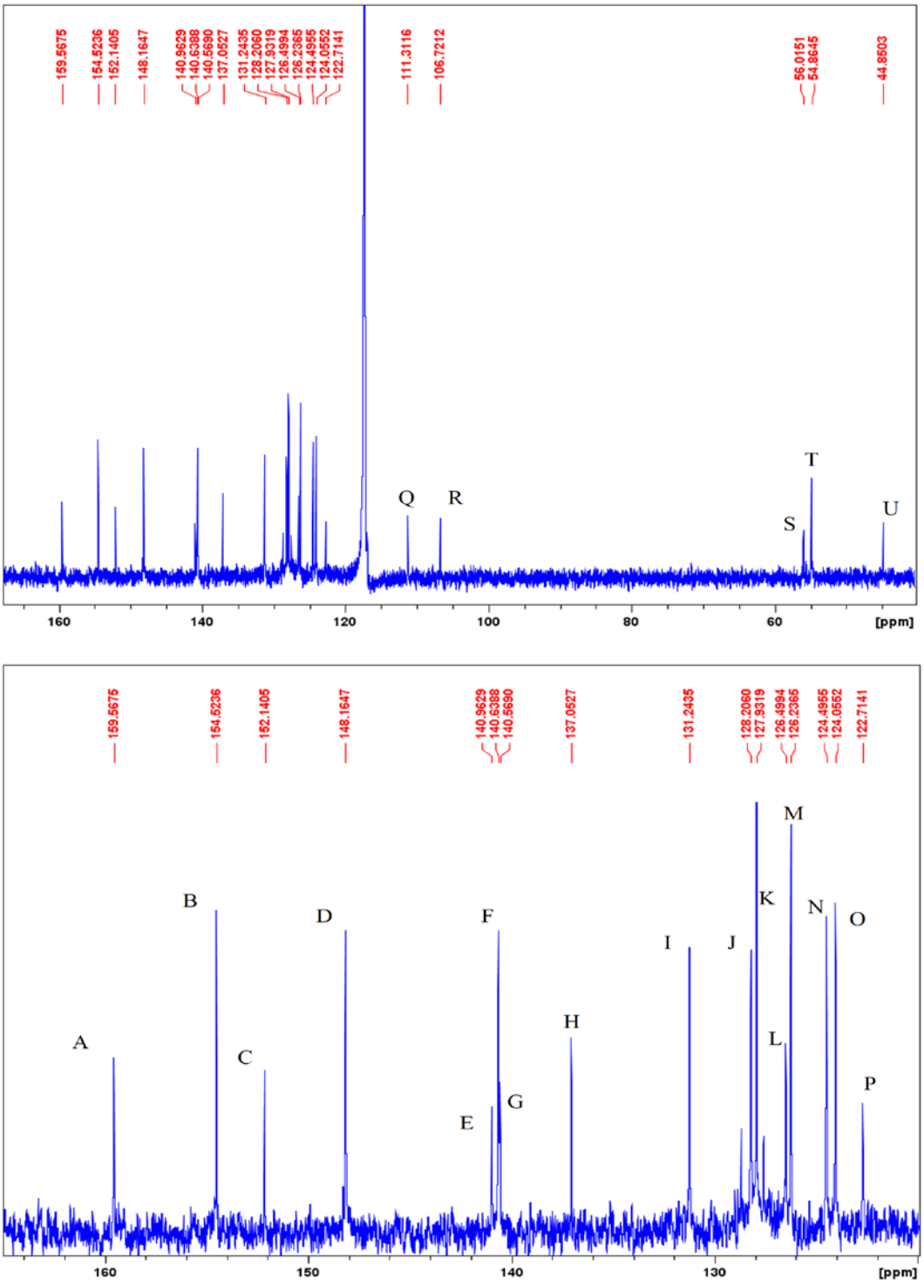

Figure C2: Full ^{13}C NMR spectrum (Top) and Zoomed region (120-165 ppm, Bottom) of ^{13}C spectra of $[(BA\text{-}TPA)Zn\text{-}SPh]^+$ cooled to -33°C (Solvent: CD_3CN)

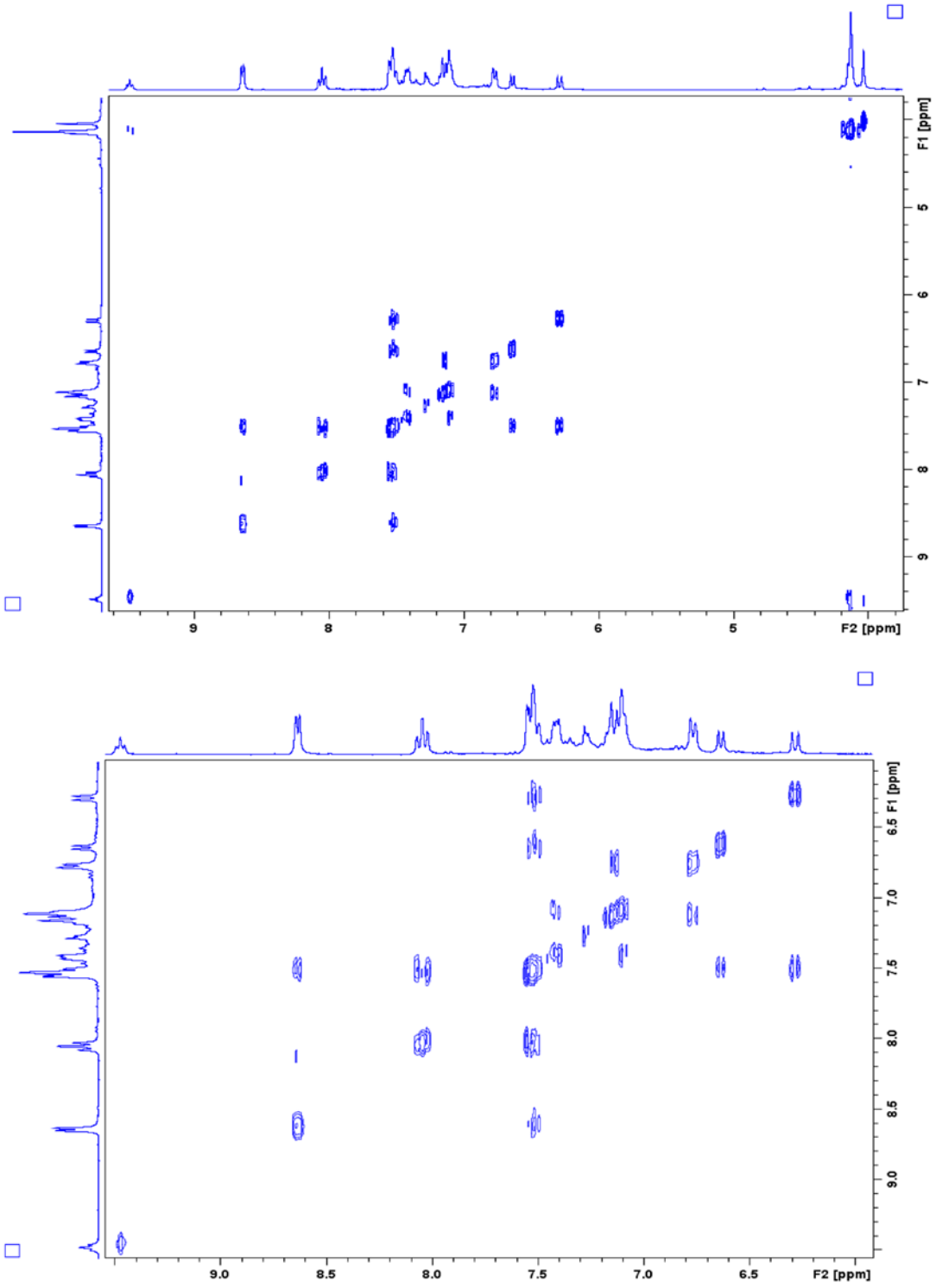

Figure C3: Full COSY spectrum (Top) and Zoomed region, (6.0-9.5 ppm, Bottom) of COSY of $[(BA\text{-}TPA)Zn\text{-}SPh]^+$ cooled to -33°C (Solvent: CD_3CN)

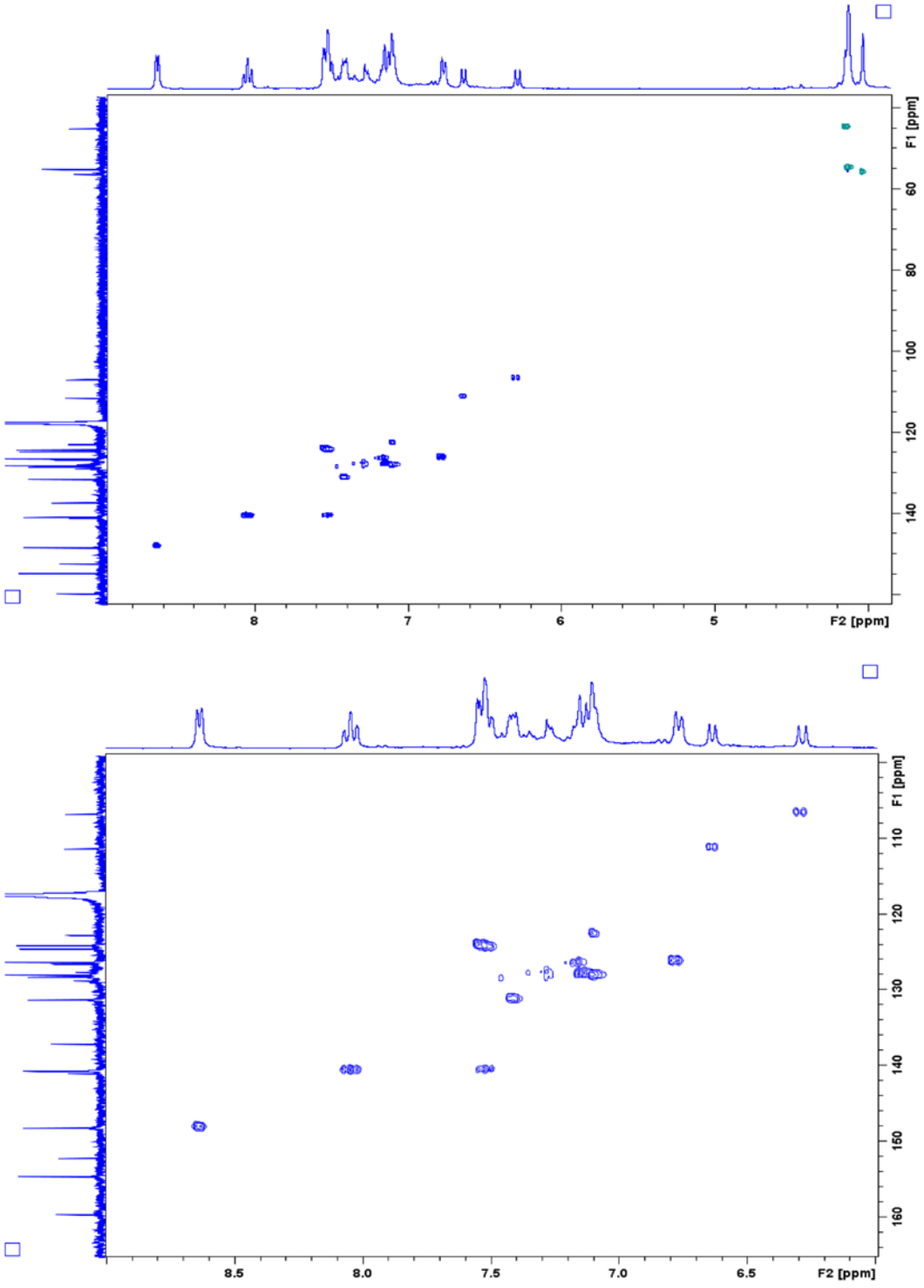

Figure C4: Full HSQC spectrum (Top) and Zoomed region (6.0-9.0 ppm, 110-160 ppm, Bottom) of HSQC of [(BA-TPA)Zn-SPh]$^+$ cooled to -33°C (Solvent: CD_3CN)

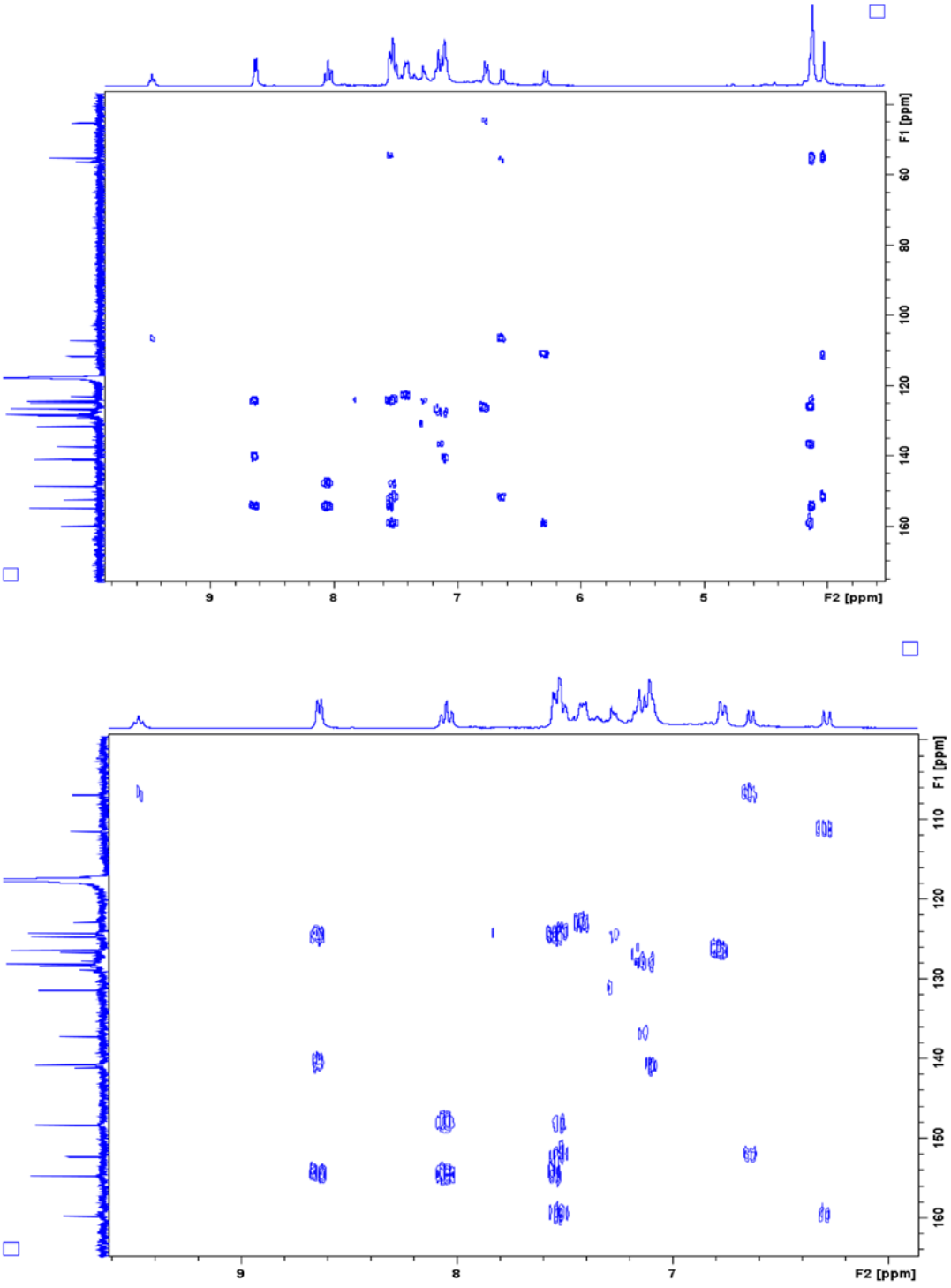

Figure C5: Full HMBC spectrum (Top) and Zoomed region (6.0-9.0 ppm, 110-160 ppm, Bottom) of HMBC of [(BA-TPA)Zn-SPh]$^{+}$ cooled to -33°C (Solvent: CD_3CN)

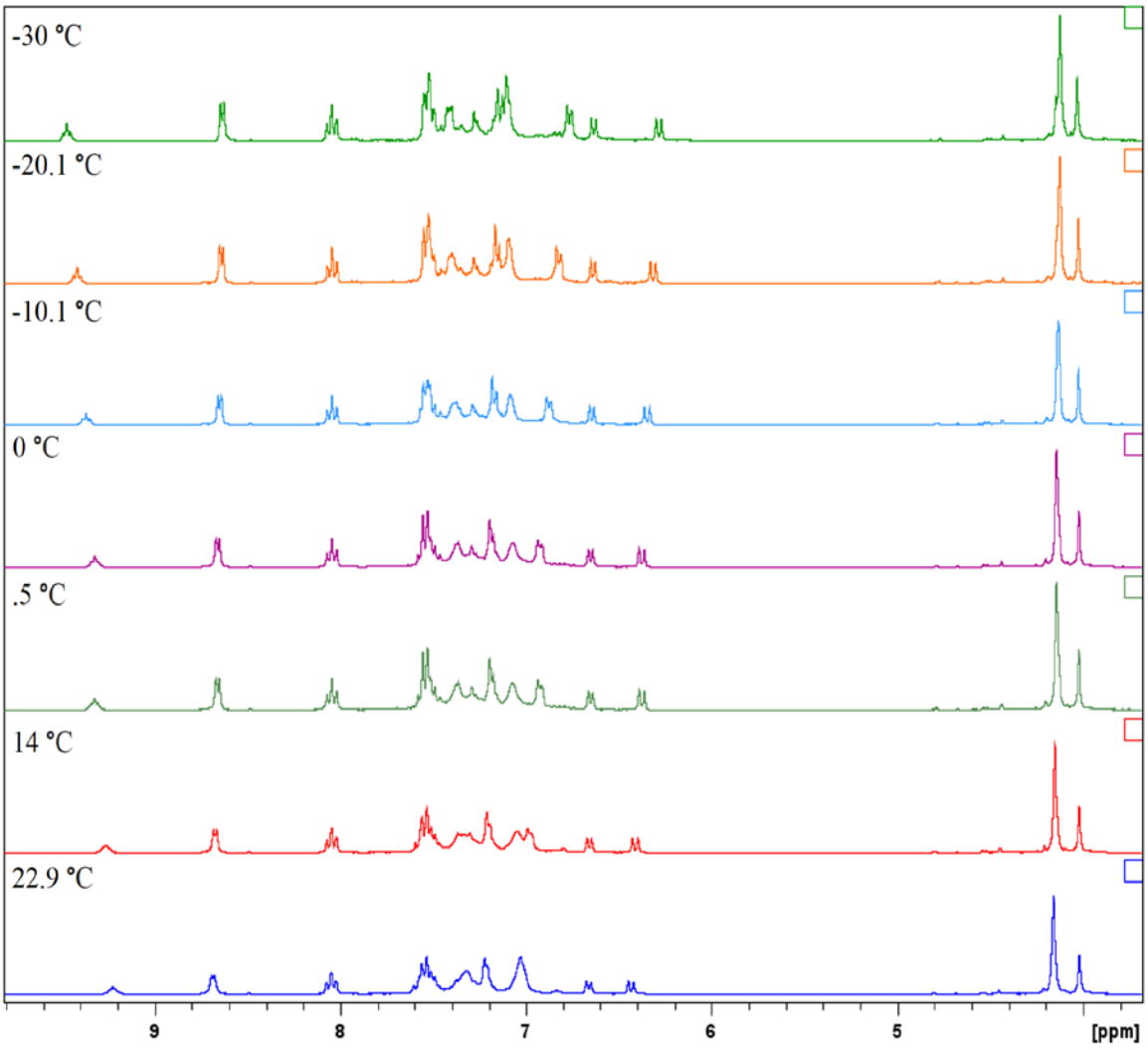

Figure C6: Results of several ^{1}H NMR spectra of [(BA-TPA)Zn-SPh]$^{+}$ during the Variable Temperature Experiment over different temperatures of [(BA-TPA)Zn-SPh]$^{+}$ (Solvent: CD_3CN)

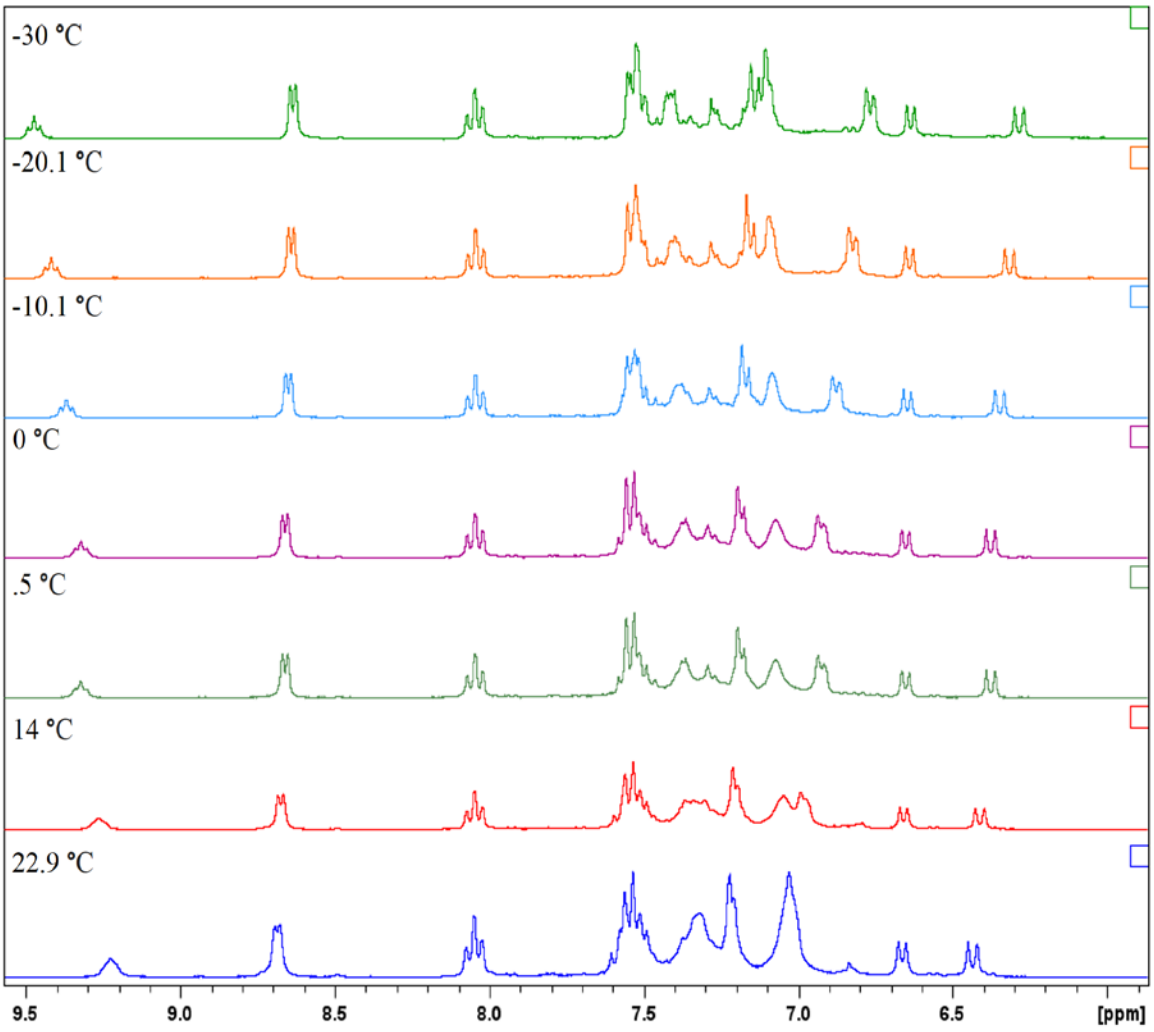

Figure C7: Results of several ^{1}H NMR spectra (6.0-9.5 ppm) of of [(BA-TPA)Zn-SPh]$^{+}$ during the Variable Temperature Experiment over different temperatures (Solvent: CD_3CN)